ELECTRORHEOLOGY AND PARTICLE DYNAMICS OF SINGLE-WALL-CARBON-NANOTUBE SUSPENSIONS UNDER SHEAR AND ELECTRIC FIELDS

BY CHEN LIN

A dissertation submitted to the

Graduate School—New Brunswick

Rutgers, The State University of New Jersey

in partial fulfillment of the requirements

for the degree of

Doctor of Philosophy

Graduate Program in Mechanical and Aerospace Engineering

Written under the direction of

Prof. Jerry W. Shan

and approved by

_____

_____

_____

_____

New Brunswick, New Jersey

October, 2010

ABSTRACT OF THE DISSERTATION

Electrorheology and particle dynamics of single-wall-carbon-nanotube suspensions under shear and electric fields

by Chen Lin

Dissertation Director: Prof. Jerry W. Shan

Electrorheological (ER) fluids are smart materials consisting of polarizable particles in an insulating liquid. Under an electric field, the dispersed particles develop an induced dipole moment and interact with each other to form chains or fibrous structures. This anisotropic microstructure enables ER fluids to have reversible changes on their macroscopic rheological properties, such as apparent viscosity and yield stress. As such, electrorheological fluids have potential application in the control of devices such as dampers, clutches, and robotics.

Single-wall-carbon-nanotubes (SWNTs), because of their nanoscale size, large aspect ratio and high polarizability, are of interest as a possible dispersed phase of novel, highly efficient ER fluids. In this work, we experimentally demonstrated for the first time the ER response of dilute SWNT suspensions, with a more-than-doubling of the apparent viscosity at moderate shear rates for a SWNT volume fraction of just $\Phi = 1.5 \times 10^{-5}$. By systematically varying the shear rate and electric field, we found that the electrorheological response can be interpreted in terms of an electrostatic-polarization model, where the governing parameter was a modified Mason number giving the ratio of viscous to dipole-dipole forces. Analysis of the electrostatic forces suggested that the

magnitude of the electrorheological response in the dilute SWNT suspension, which was much higher than conventional electrorheological fluids of comparable volume fractions, was due to the high aspect ratio of the nanotubes.

Further studies of the particle dynamics and electrorheology of SWNT suspensions were made to better understand the possible connection between the macroscopic rheology and microscopic particle dynamics. Using an optical polarization-modulation method and a modified concentric-cylinder viscometer, the first experimental measurements were made of ensemble-averaged SWNT orientation angles under combined shear flow and electric fields. The particle-orientation response was found to occur on time scales one to two orders of magnitude faster than the macroscopic electrorheological response, indicating that the particle orientation does not directly affect the apparent viscosity at these low concentrations. Consistent with the theory developed by Mason and coworkers for ellipsoidal particles, the equilibrium particle-orientation angles for various shear rates and electric fields collapsed when plotted against a parameter giving the ratio of electrostatic-to-shear-flow torques. However, the measured equilibrium orientation angles for the SWNTs showed poor quantitative agreement with the classical model. Analysis of the electrostatic interaction torques between large-aspect-ratio SWNTs showed that the interactions are significant in spite of the diluteness of the suspension, and likely account for the discrepancy between the measurement and predicted particle orientation angles.

Nomenclature

α_0 effective polarizability of a particle in vacuum

$\Delta n^{''}$ linear dichroism

$\Delta n^{'}$ linear birefringence

δ_{ij} Kronecker delta

$\dot{\gamma}$ shear rate

ϵ_f electric permittivity of continuous phase

ϵ_p electric permittivity of a particle

ϵ_{ijk} Levi-Civita symbol

ϵ_{ij} permittivity tensor

Γ'_{Ei} electrostatic torque in the x'_i direction

Γ'_{Hi} hydrodynamic torque in x'_i direction

ω frequency of an AC field

ω'_i angular velocity or spinning velocity of the particle about x'_i direction

ϕ, θ, ψ a set of Eulerian angles

ψ electrical potential

ψ^i electrical potential inside a particle

ψ^o electrical potential outside a particle

σ_f electrical conductivity of continuous phase

σ_p	electrical conductivity of a particle
τ_{mw}	characteristic relaxation time or Maxwell-Wagner relaxation time
Im	imaginary part
Re	real part
$\underline{\epsilon}_f$	complex permittivity of fluid
$\underline{\epsilon}_p$	complex permittivity of a particle
$\underline{K}$	complex form of Clausius-Mossotti function
$\vec{n}$	the unit normal vector of the interface
$\vec{D}$	displacement flux vector
$\vec{E}^-$	electric field inside a particle
$\vec{E}_0$	external electric field
$\vec{e}_i$	unit vector along i axis
$\vec{E}_{\parallel}$	electric field parallel to the a_1 axis of an ellipsoid
$\vec{E}_{\perp}$	electric field perpendicular to the a_1 axis of an ellipsoid
$\vec{F}_{dep}$	dielectrophoretic force
$\vec{T}^e$	torque applied by electric field
$\vec{u}$	unit orientation vector of the particle
$\widetilde{\alpha}$	polarizability tensor
$\widetilde{I}$	identity tensor
$\widetilde{n}$	refractive index tensor
$\widetilde{S}(0)$	scattering matrix
a	radius of the particle

a_1, a_2, a_3 semi-axes of an ellipsoid

C orbit constant

d diameter of carbon nanotube

e eccentricity of a prolate spheroid

$g(r_e)$ shape distribution function

i, j imaginary unit

J Jones matrix

K Clausius-Mossotti function

k wave number

k_0 initial phase angle

k_f dielectric constant of fluids

l length of carbon nanotube

L_{x_1} depolarization factor along x_1 axis

n_f refractive index of ambient fluids

$p\left(\theta, \phi, r_e\right)$ orientation distribution function of a suspension system with prolate spheroids

p' dipole moment in the x_i' $(i = 1, 2, 3)$ in the body set frame

$p_0\left(\theta_0, \phi_0\right)$ initial orientation distribution function

$p_\sigma\left(\theta, \phi\right)$ probability orientation distribution

P_{eff} effective polarization

p_{eff} induced effective moment

r distance from the center of the sphere to an arbitrary point

r_e aspect ratio of a spheroid

T period of particle rotation about the vorticity axis

u_i velocity component in the x_i axis

v_s volume of a spherical particle

v_{ps} volume of a prolate spheroidal particle

W interaction potential between two dipoles

x_i' $(i = 1, 2, 3)$ body set Cartesian coordinates fixed and moves with the particle

x_i $(i = 1, 2, 3)$ Cartesian coordinate with fixed directions in space and centered at the center of the particle

$\underline{p}_{eff}$ complex form of induced effective moment

Acknowledgements

I feel I am blessed to have Dr.Jerry W. Shan to be the advisor of my Ph.D study. His insightful advice and patient encouragement have always been inspiring me and guiding me through this journey. His personality and professionalism is and will be a model for me through the course of my life. I would like to thank John Petrowski for his suggestions and great help in the design of the experiments. Also I would thank my wife, my daughter and my parents for always supporting me.

Table of Contents

List of Tables

List of Figures

Chapter 1

Introduction

1.1 Carbon nanotubes (CNTs) and carbon nanotube (CNT) suspensions

Carbon nanotubes (CNTs), with their unique physical properties and their potential for commercial applications, have been of great interest to many scientists and engineers since their discovery by Iijima [1] in 1991. The ultra-high aspect ratio of their geometry, their electrical conductivity and their enormous mechanical strength (the density normalized strength is about 56 times that of steel wire [2]) make CNTs novel candidates for variety of possible applications, including conductive and high-strength composite materials [3], energy-storage devices [4,5], field-emission sensors [6,7] or drug-delivery vessels [8].

Carbon nanotubes belong to the fullerene structural family, where each member of the family composes entirely of carbon. These members include graphite, which is comprised of stacked graphene sheets of linked hexagonal rings, buckyballs (C_{60}) the smallest, soccer-ball-shaped member of the family, and carbon nanotubes (also known as buckytubes). There are two major categories of carbon nanotubes that can have high structural perfection: single wall carbon nanotubes (SWNTs) and multiwall carbon nanotubes (MWNTs). Single-wall carbon nanotubes consist of a single graphene sheet wrapped into a cylindrical tube. Multi-wall carbon nanotubes comprise an array of such cylindrical tubes that are concentrically rolled layer by layer. Unlike graphite which is always conductive or has zero band gap, a SWNT can have different macroscopic electrical properties (*i.e.*, being metallic or semi-conducting), depending on the direction in which the graphene sheet is wrapped to form the cylindrical tube. A pair of integers (n,m) is used to quantify the structural arrangement and resulting type of SWNT.

Single-wall carbon nanotubes are armchair if $(m = n \neq 0)$, zigzag type if $(n = 0$ or $m = 0)$, or chiral (any n, m combination other than the previous two). The armchair ones are all metallic, while those with $(n - m = 3k)$, where k is a non-zero integer, are semiconductors with small band gap. All other ones are semiconductors with a band gap which depends on the tube diameter [9]. Single wall carbon nanotubes have diameters of approximately 1 nm, and typical lengths on the order of microns.

The properties of carbon nanotubes have been studied for more than a decade. Scientists and engineers have shown that CNTs are promising building blocks for many applications such as polymer reinforcement [10,11] or energy conversion devices [12,13]. However, many other applications are based upon the understanding of how CNTs behave as a particulate component in aqueous or other non-aqueous liquid suspensions. Colloidal suspensions of CNTs are of interest in applications as diverse as polymer composites [14], drag reduction [15] in industrial pipe flows, and for drug-delivery vessels [16] in the human blood system.

A signifcant early challenge in the liquid-phase manipulation of CNTs was the stable dispersal of individualized (rather than bundled) CNTs in aqueous or non-aqueous solvents. Fortunately, in recent years, many inorganic and organic solvents have been found to be good solvents for CNTs with capacities of producing high yields of individual CNTs. In aqueous suspensions, surfactants and other surface modification have been used to effectly disperse CNTs. For example, high-weight-fraction (20mg/mL) dispersal of SWNTs in water has been reported with sodium dodecylbenzene sulfonate as surfactant. In these aqueous suspensions, approximately 63% of SWNTs were believed to exist in individual form [17]. Other SWNTs/organic solutions also show high stability when SWNTs at high weight fraction are dispersed [18]. The rapid advancement in the solubilization of CNTs has made possible the further study of CNTs suspensions for a variety of applications.

The stable dispersal of CNTs in liquid phase has also enabled the study of the individual and collective dynamics of nanotubes in liquids. A thorough study of the motion of an individual CNT in a quiescent or shear flow is essential to the prediction and manipulation of the trajectory of CNTs in suspension. Such studies would have

application, for instance, to the behavior of CNT-based functional nanoscaled medicine or bio-sensors for clinical usage [19]. The dynamics of CNTs in liquid suspension are also key to large-scale processing of SWNTs fibers [20] and films [21]. Other application of the controlled manipulation of CNTs in liquid suspension include the sorting of SWNTs according to their different size and electronic properties [22–24]. The study of the dynamics of nanosized, highly anisotropic CNTs in liquid suspension is of both fundamental interest and practical application.

Investigating the behavior of CNTs in liquid suspension is interesting, challenging, and inspiring. From the point of view of fluid mechanics, we are fortunate to be able to draw upon a rich history of study of low-Reynolds-number (Stoke's) flow. In this thesis, we experimentally test the applicability of some classic creeping-flow theories to the motion of nanosized, highly anisotropic CNTs under combined shear flow and electric fields. The topic not only provides a great chance to review some of the greatest work in Stoke's flow, but also the opportunity to develop some insights to applying (and adapting as necessary) classical theory to this newborn subject.

1.2 Literature review of electrorheology and particle dynamics of micro/nanoparticle suspensions

Electrorheology is a subject which studies the rheological properties, such as apparent viscosity and yield stress, of colloidal suspensions upon the applications of external electric fields. Electrorheological (ER) fluids typically consist of micro-sized dielectric particles dispersed in an insulating liquid phase. Winslow is believed to be the first to describe the ER effect. In his 1949 paper [25] he observed a several-orders-of-magnitude increase in the apparent viscosity of ER fluids consisting of dielectric particles in a low-viscosity oil. Winslow attributed this effect to the fiber-like structures spanning the whole gap between the two electrodes which formed in ER fluids under an external electric field. Over the years, much progress has been made on the properties of ER fluids and the mechanisms behind the ER response [26–32]. Excellent reviews of the phenomena and mechanisms of ER fluids are given in Refs. 30-32. The ultimate
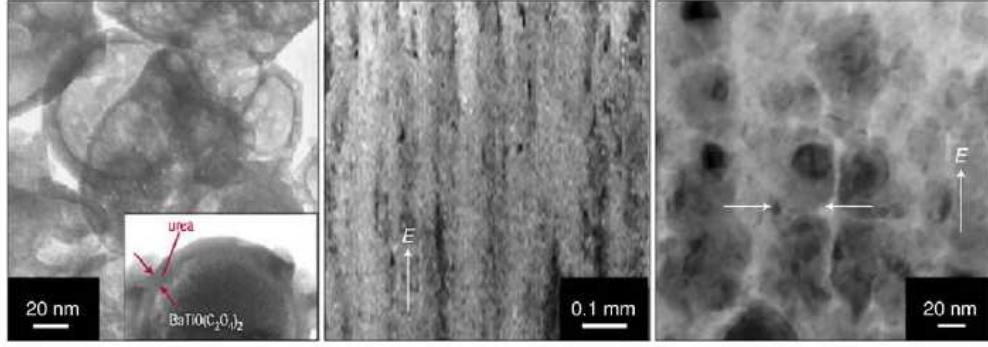
Figure 1.1: Images of nanoparticles in gigantic ER suspensions discovered by Wen's group [33].

practical motivation is to find a way to engineer highly effective and efficient ER fluids for power transfer and dissipation in real applications such as clutches, brake systems, and dampers for automobiles and other machinery.

Recent developments in the commercial-scale synthesis of nano-sized particles have led to new interest in novel ER fluids having nanoparticles as the dispersed phase. For instance, gigantic ER effects with a yield stress of 130 kPa [33] have been recently reported for urea-coated $BaTiO(C_2O_4)_2$ nanoparticles. Such a scientific discovery is rather exciting due to the fact that the maximum yield stress achieved by most of the conventional ER fluids is less than 10 kPa, well below the operational stress of about 30 kPa required for many mechanical devices. A mechanism with statistical mechanics of aligned dipole layers has also been proposed to explain this gigantic ER phenomena [34]. Their numerical results from Monte Carlo simulation agree well with the experiments.

Both positive and negtive ER behaviors were observed in the case of carbon nanofiber, CNT, and $Pb_3O_2Cl_2$ nanowire laden suspensions at the concentration of 0.0125 wt% [35]. Oscillatory shear experiments conducted to investigate the ER properties of these suspensions found that the storage modulus (the elastic component of the viscoelastic response) increased or decreased with electric field, depending on the particle type. The loss modulus varied only slightly with electric-field strength. The positive and negative ER behaviors of storage modulus were attributed to differences in the electrical conductivity of the dispersed phase resulting in different polarization behavior.
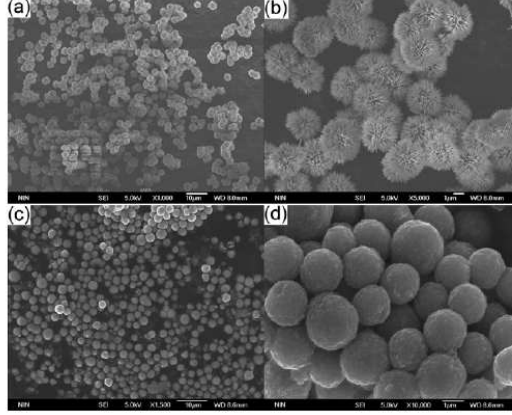
Figure 1.2: SEM images of sea-urchin-like hierarchical Cr-doped titania particles (a, b) and smooth Cr-doped titania particles (c, d). [36]. The nanostructure of (a,b) were believed to be the key factor in enhancing the ER effects.

Cr-doped titania particles with sea-urchin-like hierarchical nanostructure (Fig. 1.2 b) have recently been found to effectively enhance the efficiency of ER fluids [36]. The enhancement of ER effect of the suspension of this hierarchical Cr-doped titania is attributed to the combined effects of increased interfacial polarization and inter-particle interaction due to the presence of urchin-like nanostructures on the ER microparticles, which greatly increase the surface area of the particles.

Many researchers have investigated the effect of particle morphology on ER behavior. Titania-coated silica nanomaterials with three different shapes as in Fig. 1.3 (nanosphere, nanorod, nanotube) have been fabricated to examine the influence of particle geometry on ER fluid in nanometer-size region recently [37]. It is believed that the geometrical effect originating from high particle aspect ratio, which brings larger achievable polarizability and short relaxation times of interfacial polarization, play a dominant role in enhancing the performance of the ER fluid. The results of Hong *et al.* show that the increase in particle aspect ratio has a strong influence on ER activity and provides outstanding enhancement in the shear stress value at a given shear rate of the titania-coated silica nanotube based ER fluid.

Highly anisotropic nanowhiskers and nanotubes as possible particulate components have been used to make non-conventional ER fluids [38–40] that could operate at low voltage in micro or nano-scaled actuators or switches. The ER fluid was prepared by
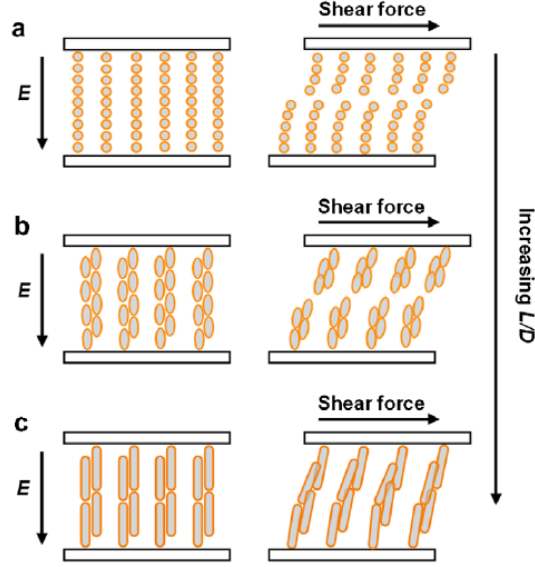
Figure 1.3: Evolution of electric field induced chain structure in titania-coated silica nanomaterials under shear force: (a) nanospheres, (b) nanorods, and (c) nanotubes [37].

dispersion of titanate nano-whiskers in silicone oil with the ultrasonic technique [39]. It was found that the stability of this nano-whisker ER fluid was very good. No signicant sedimentation was found in this nano-whisker ER fluid after several months, due to the supporting effect of the nano-whiskers with large aspect ratio. Under electric field, this nano-whisker ER fluid showed notable ER activity with dynamic yield stress of about 1.1 kPa at 3 kV/mm and 10% of particle volume fraction.

A conclusion can be drawn that there are three principal advantages of using nano-sized particles in ER fluids: (1) High particle aspect ratio, which is one of the ways to enhance ER effect [41], is more readily achieved with nano-particles, (2) Greater surface area per unit volume of nano-particles or porous material doped nano-particles [39] can also increase the efficiency of ER fluid, and (3) the size of nanoparticles can improve the stability of the ER fluids against sedimentation.

For these reasons, the high aspect ratio and electrical polarizability of single-wall carbon nanotubes (SWNTs) makes them of interest as a possible particulate component of electrorheological (ER) fluids. As we will show later in Sec. **3.1.3**, dilute SWNT suspensions have field-induced changes in apparent viscosity that are comparable to spherical-particle suspensions of 3-orders-of magnitude-higher volume fraction [42]. The
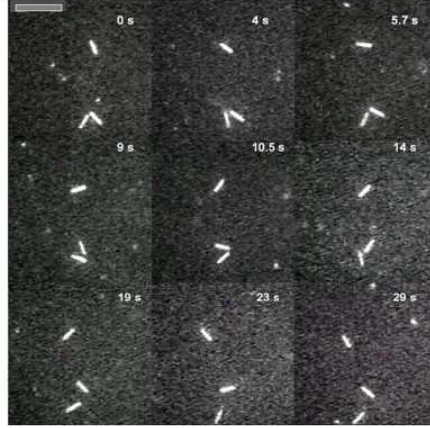
Figure 1.4: Fluorescence visualization of individual SWNTs [47].

macroscopic ER properties of such SWNT suspensions are determined by the particle dynamics and microstructure under both shear flow and electric fields.

In the absence of an electric field, there is a rich history (*cf.* reviews by Happel & Brenner [43] and Leal [44], for example) of study of the dynamics of anisotropic particles in a viscous flow, dating back to Jeffery's theoretical [45] and Taylor's experimental [46] studies of ellipsoidal particles in simple shear flow. Theories of particle motion under both shear flow and electric field can be found in Mason's early work in 1960s. These classic theories will be reviewed in a thorough manner in the following chapters. Experimentally, the particle dynamics and rheology of SWNTs in liquid suspension have been studied in recent years in flows without external electric fields by Duggal [47], Hobbie [48, 49], and Tiwari [50], among others.

The dynamics of individual SWNTs in water was visualized directly by fluorescence video microscopy as seen in Fig. 1.4, a series of snapshots of the video [47]. They measured the confined rotational diffusion coefficient and find it in reasonable agreement with predictions based on confined diffusion of dilute Brownian rods. The critical concentration at which SWNTs in water start to interact was also determined. The persistence length was calculated to range between 32 and 174 μm, in agreement with theoretical estimates. Thus, it could be concluded based upon their results that SWNTs can be treated as rigid rods in quiescent fluids.

Optical measurements of the shear response of semidilute dispersions of polymer-dispersed multiwalled carbon nanotubes were carried out by Hobbie [48]. The results showed that in a highly elastic polymer solution the nanotubes orient with the flow field at high shear rates, in the limit of large Deborah number. While in a weakly elastic polymer melt, the data suggest that the tubes orient along the direction of flow at low shear stress, with a transition to vorticity alignment above a critical shear stress. Measurements of shear-induced structure and orientation in dilute dispersions of CNT using combined polarized light scattering and optical microscopy were also conducted [51] and a semimacroscopic model for optically anisotropic nanotube suspension was derived [52].

On the other hand, nanotube dynamics and orientation under electric fields in a quiescent fluid have been studied by [22,53–55]. The hydrodynamics of SWNTs rotated in quiescent liquid suspension by an external electric field was experimentally studied with laser polarimetry by Zimmermann and Shan [55]. Their results implied that despite the fact that the size of SWNTs approaches that of the solvent molecules, classical continuum hydrodynamic theory holds approximately for external flow about carbon nanotubes.

A recent paper has reported a theoretical and computational study of the aggregation behavior of rod-like particle suspensions under combined shear and electric fields [56]. They examined from a theoretical perspective the hypothesis that a combination of AC electric and shear fields oriented at certain angles may be used to enhance the dispersion of aggregated rod solutions. The results from computer simulations display good agreement with their theoretical analysis and parametric regimes were suggested in which the use of a combination of electric and shear fields may enhance the dispersion of aggregated nanotubes. However, no experiments has been done to date on the orientational dynamics of suspended SWNTs under combined shear flow and electric fields. The current work seeks to fill some of the gaps in existing knowledge concerning CNT suspensions.

1.3   Statement of objectives

This dissertation investigates CNT suspensions from two different perspectives: First, from the perspective of the macroscopic electrorheology of dilute SWNT suspensions, and secondly, from the point of view of the microscopic particle dynamics of the system. The two investigations are closely related as the author believes that the macroscopic electrorheology is driven by the particle dynamics and microstructure formed in the suspensions. The specific scientific objectives of the work are to:

1. Demonstrate and characterize the electrorheology of dilute SWNT suspensions.

2. Clarify the mechanisms responsible for the ER behavior by examing the validity of conventional ER models for these SWNT suspensions. In particular, we study the apparent viscosity as a function of a parameter (the Mason number), giving the ratio of viscous to dipole-dipole forces acting on the particles.

3. Compare the magnitude of the ER response in dilute SWNT suspensions to that of conventional (spherical particle) suspensions of similar volume fraction.

4. Make the first experimental measurements of the ensemble-averaged nanotube orientation angle, and compare results with the classical theory of Mason and coworkers for the motion of ellipsoidal particles under combined shear flow and electric fields

5. Identify the relative contributions of particle orientation and particle chaining to the ER response of SWNT suspensions by making simultaneous measurements of nanotube orientation angle and the apparent viscosity .

 In the following chapters, we first review in more detail the classical models for the interfacial polarization of particles (Sec. **2.1.1-2.1.3**) and the motion of particles in shear and electric fields (Sec. **2.1.4**), as well as light scattering by small particles (Sec. **2.2**). Our experimental results on the macroscopic electrorheology of dilute SWNT suspensions are discussed next (Ch. **3**), followed by a description and analysis of our measurements of the equilibrium nanotube orientation angle under shear and electric

fields (Ch. **4**). The dissertation concludes with an summary of results and suggestions for future work.

Chapter 2

Background

2.1 Classical electrostatic polarization models

With the development of new ER fluids having anisotropic, nano-sized particles such as CNTs as the dispersed phase, a re-examination of classical models for the mechanisms underlying conventional ER fluids seems warranted. Many theoretical models of ER fluids have been proposed ever since the discovery of the ER effect by Winslow. The most successful and generally accepted models attribute the ER response to dipolar particle interactions caused by interfacial (Maxwell-Wagner) polarization of the particles under the electric field. A review of the theoretical models for the polarization and resulting forces/torques and motions of particles with various morphologies and different physical properties is briefly discussed in the following.

2.1.1 Polarization model for spherical particles

a. Lossless dielectric sphere in lossless dielectric medium in an uniform field

   An ideal dielectric sphere suspended in an insulating liquid phase with conductivities of both the particle and the fluid being neglected is the simplest case of an electrostatic polarization model. The dielectric particle is polarized with only bound charge under an external electric field. Assuming the particle is a perfect sphere and the field only induces dipole moments in the particle, the electrical potential can be obtained by solving Laplace's equation

$$\bigtriangledown^2 \psi = 0. \tag{2.1}$$

in the bulk phase with a uniform applied electric field, $\vec{E}_0 = E_0 \vec{e}_z$.

The boundary conditions at the interface of the particle and surrounding fluid are,

$$\psi^i = \psi^o, \tag{2.2}$$

$$\epsilon_p \bigtriangledown \psi^i \cdot \vec{n} = \epsilon_f \bigtriangledown \psi^o \cdot \vec{n}, \tag{2.3}$$

where ϵ_p and ϵ_f are electric permittivities of particle and continuous phase respectively, and $\vec{n}$ is the unit normal vector of the interface. The superscript i and o indicate the potential inside and outside the particles. The solution for the electrical potential is

$$\psi^i = -E_0 r \frac{3\epsilon_f}{\epsilon_p + 2\epsilon_f} \cos\theta, \tag{2.4}$$

$$\psi^o = -E_0 r \left[1 - K \left(\frac{a}{r} \right)^3 \right] \cos\theta, \tag{2.5}$$

where $K = \frac{\epsilon_p - \epsilon_f}{\epsilon_p + 2\epsilon_f}$, is the Clausius-Mossotti function, a is the radius of the particle, and r is the distance from the center of the spherical particle to an arbitrary point in the uniform electric field.

The induced potential outside the particle is the same as that of a dipole oriented along the z-axis whose moment is

$$p_{eff} = 4\pi\epsilon_f K a^3 E_0. \tag{2.6}$$

b. Dielectric sphere with ohmic loss in dielectric medium with ohmic loss in an AC field

The case for dielectric sphere with ohmic loss in a lossy dielectric medium is similar to lossless case except now both the sphere and the fluid medium have finite electrical conductivities, σ_p and σ_f, respectively. When an electric field is applied upon the suspension, both bound charge and free charge are induced in the particle and the medium. For an AC field of magnitude E_0 and frequency ω, we have

$$\vec{E}(t) = \mathbf{Re}[E_0 \vec{e}_z \exp(j\omega t)]. \tag{2.7}$$

Laplace's equation (2.1) and the boundary condition of continuous potential at the interface of Eq. (2.2) are the same as lossless case. The continuity of the normal component of the displacement flux vector must be replaced by the instantaneous charge conservation condition because of the time-dependent accumulation of free charge on the interface. The resulting expression for effective moment is the same as the previous lossless case in Eq. (2.6) except now the Clausius-Mossotti function is in a complex form

$$\vec{\underline{p}}_{eff} = 4\pi\epsilon_f \underline{K} a^3 \vec{E}_0, \tag{2.8}$$

where

$$\underline{K} = \frac{\underline{\epsilon}_p - \underline{\epsilon}_f}{\underline{\epsilon}_p + 2\underline{\epsilon}_f}, \tag{2.9}$$

and the complex permittivities are

$$\underline{\epsilon}_p = \epsilon_p - \frac{\sigma_p}{\omega}j$$

$$\underline{\epsilon}_f = \epsilon_f - \frac{\sigma_f}{\omega}j. \tag{2.10}$$

Equation (2.9) can be re-written to reflect the characteristic relaxation time or Maxwell-Wagner time scale τ_{mw}

$$\underline{K}(\omega) = \left(\frac{\sigma_p - \sigma_f}{\sigma_p + 2\sigma_f}\right)\left[\frac{j\omega\tau_0 + 1}{j\omega\tau_{mw} + 1}\right], \tag{2.11}$$

where

$$\tau_{mw} = \frac{\epsilon_p + 2\epsilon_f}{\sigma_p + 2\sigma_f}$$

$$\tau_0 = \frac{\epsilon_p - \epsilon_f}{\sigma_p - \sigma_f}. \tag{2.12}$$

The complex form of the Clausius-Mossotti function is very important in later calculations of interactions between particles. Two limiting cases depending on the relative magnitude of the characteristic relaxation time constant τ_{mw} and the frequency of the electric field are usually used to examine the direction of dielectrophoretic force at the low and high frequency ends:

$$\lim_{\omega\tau_{mw}\to 0} \underline{K} = \frac{\sigma_p - \sigma_f}{\sigma_p + 2\sigma_f}$$

$$\lim_{\omega\tau_{mw}\to\infty} \underline{K} = \frac{\epsilon_p - \epsilon_f}{\epsilon_p + 2\epsilon_f}. \tag{2.13}$$

Thus, in the low frequency limit, the magnitude of the effective moment depends on the difference of the electrical conductivities of the particle and the liquid while in the high frequency limit, the difference of permittivities determines the magnitude of the effective moment. A detailed derivation of Eq. (2.13) for a more general case can be found in Appendix I.

2.1.2 Polarization model for ellipsoidal particles

Now we extend our analysis to ellipsoidal particles. To be consistent with the discussion on spherical particles, we first consider lossless particles and then lossy particles.

a. Lossless dielectric ellipsoid in lossless dielectric medium

The electrical potential for a dielectric ellipsoid in a uniform field is given by Stratton [57]. The induced effective moment is

$$\vec{p}_{eff} = \frac{4\pi a_1 a_2 a_3}{3} \left(\epsilon_p - \epsilon_f \right) \vec{E}^-, \tag{2.14}$$

where $a_1 > a_2 > a_3$ are semi-axes of the ellipsoid which are aligned with the x_1, x_2, x_3 axes as depicted in Fig. 2.1. $\vec{E}^-$ is the field inside the ellipsoidal particle. The x_1 component of it is

$$E_{x1}^- = \frac{E_{0,x1}}{1 + \left(\frac{\epsilon_p - \epsilon_f}{\epsilon_f} \right) L_{x_1}}, \tag{2.15}$$

where L_{x_1} is the depolarization factor along the x_1 axis and is defined as

$$L_{x_1} = \frac{a_1 a_2 a_3}{2} \int_0^\infty \frac{ds}{\left(s + a_1^2 \right) \sqrt{\left(s + a_1^2 \right) \left(s + a_2^2 \right) \left(s + a_3^2 \right)}}. \tag{2.16}$$

The three depolarization factors are all positive and interrelated as

$$L_{x_1} + L_{x_2} + L_{x_3} = 1. \tag{2.17}$$

In a special case where the particle is a prolate spheroid ($a_1 > a_2 = a_3$), the imposed electric field has components parallel ($\parallel$) and perpendicular ($\perp$) to the a_1 axis of the particle:

$$\vec{E}_0 = \vec{E}_\parallel + \vec{E}_\perp. \tag{2.18}$$
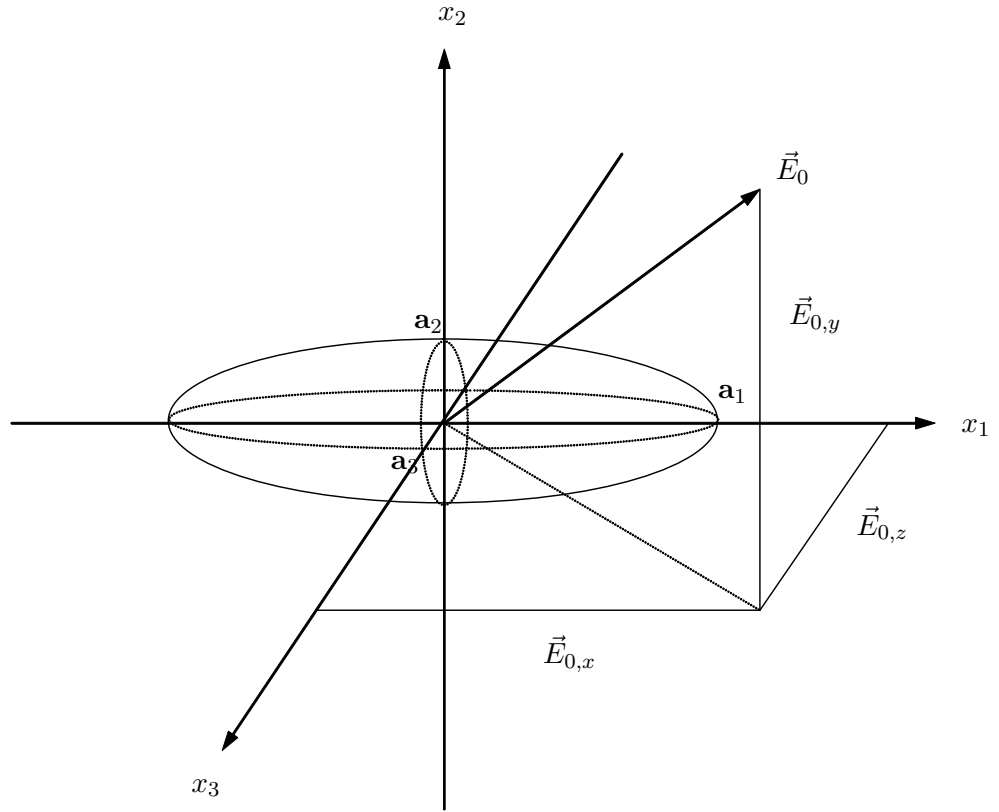
Figure 2.1: Ellipsoidal particle with semi-axes $a_1 > a_2 > a_3$ aligned with the cartesian coordinate system x_1, x_2, x_3 is subjected to an external uniform electric field $\vec{E}_0$.

The expression for the induced effective moment is the same as Eq. (2.14) with the induced field inside the particle having two components,

$$
\begin{aligned}
\vec{E}^{-} &= \vec{E}_{\parallel}^{-} + \vec{E}_{\perp}^{-} \\
&= \frac{\vec{E}_{\parallel}}{1 + \left(\frac{\epsilon_p - \epsilon_f}{\epsilon_f}\right) L_{\parallel}} + \frac{\vec{E}_{\perp}}{1 + \left(\frac{\epsilon_p - \epsilon_f}{\epsilon_f}\right) L_{\perp}}.
\end{aligned}
\tag{2.19}
$$

An analytical solution for the elliptic integral of $L_{\parallel}$ is given by Jones [58] as

$$
\begin{aligned}
L_{\parallel} &= \frac{a_1 a_2^2}{2} \int_0^{\infty} \frac{ds}{\left(s + a_1^2\right)^{3/2} \left(s + a_2^2\right)} \\
&= \frac{a_2^2}{2a_1^2 e^3} \left[ln\left(\frac{1+e}{1-e}\right) - 2e \right],
\end{aligned}
\tag{2.20}
$$

where $e \equiv \sqrt{1 - \frac{a_2^2}{a_1^2}}$ is the eccentricity of the spheroid. For high aspect ratio particles like SWNTs, the expression for $L_{\parallel}$ can be further approximated as

$$
L_{\parallel} \approx \frac{1}{r_e^2} \left[ln\left(2r_e\right) - 1 \right],
\tag{2.21}
$$

where r_e is the aspect ratio defined as $r_e = \frac{a_1}{a_2}$.

b. Dielectric ellipsoidal particle with ohmic loss in dielectric medium with ohmic loss in an AC field

Though the expressions for effective moment and characteristic relaxation time are similar to those of spherical particle case, a dielectric ellipsoidal particle has its unique orientational behavior. The components of effective moment of a dielectric ellipsoid with ohmic loss are

$$
\left(\underline{p}_{eff}\right)_i = 4\pi a_1 a_2 a_3 \epsilon_f \underline{K}_i E_{0,i},
\tag{2.22}
$$

where $i = x_1, x_2, x_3$ and the complex Clausius-Mossotti function $\underline{K}(\omega)$ now also has three components:

$$
\underline{K}_i \equiv \frac{\underline{\epsilon}_p - \underline{\epsilon}_f}{3\left[\underline{\epsilon}_f + \left(\underline{\epsilon}_p - \underline{\epsilon}_f\right) L_i\right]},
\tag{2.23}
$$

which yield three distinct Maxwell-Wagner characteristic relaxation times

$$
\left(\tau_{mw}\right)_i = \frac{\left(1 - L_i\right)\epsilon_f + L_i \epsilon_p}{\left(1 - L_i\right)\sigma_f + L_i \sigma_p}.
\tag{2.24}
$$
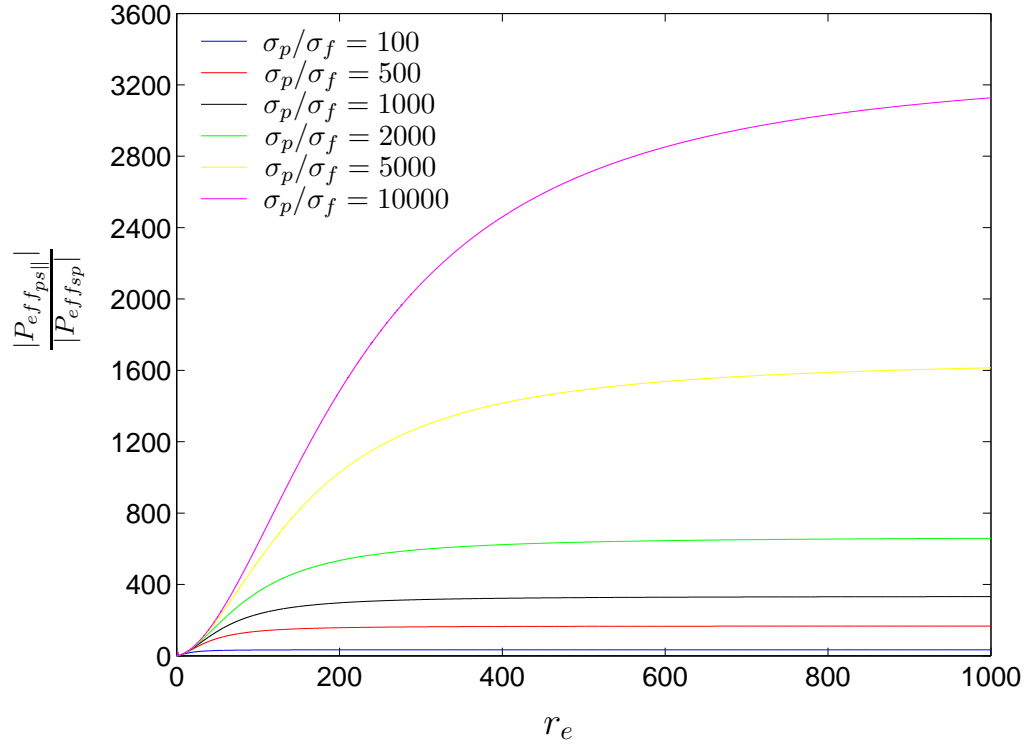
Figure 2.2: The ratio of the effective polarization of a lossy prolate spheroidal particle and that of a lossy spherical particle as a function of particle aspect ratio at various $\frac{\sigma_p}{\sigma_f}$ values.

In the case of a prolate spheroid with high aspect ratio in which $a_1 \gg a_2 = a_3$, $L_\parallel \ll 1$ and $L_\perp = (1 - L_\parallel)/2 = 1/2$, the Maxwell-Wagner relaxation times reduce to

$$\tau_{mw,\parallel} = \frac{r_e \epsilon_f + (ln\,(2r_e) - 1)\,\epsilon_p}{r_e \sigma_f + (ln\,(2r_e) - 1)\,\sigma_p}$$

$$\tau_{mw,\perp} = \frac{\epsilon_f + \epsilon_p}{\sigma_f + \sigma_p}. \tag{2.25}$$

The effective moment simplifies to

$$\vec{\underline{p}}_{eff} = 4\pi a_1 a_2^2 \epsilon_f \left(\underline{K}_\parallel \vec{E}_{0,\parallel} + \underline{K}_\perp \vec{E}_{0,\perp} \right), \tag{2.26}$$

where

$$\underline{K}_\parallel = \frac{\underline{\epsilon}_p - \underline{\epsilon}_f}{3 \left\{ \underline{\epsilon}_f + \left(\underline{\epsilon}_p - \underline{\epsilon}_f \right) \frac{1}{r_e^2} \left[ln\,(2r_e) - 1 \right] \right\}}$$

$$\underline{K}_\perp = \frac{2 \left(\underline{\epsilon}_p - \underline{\epsilon}_f \right)}{3 \left(\underline{\epsilon}_p + \underline{\epsilon}_f \right)}. \tag{2.27}$$

Similar to what we have discussed in Sec. **2.1.1.b**, two limiting cases for the expression of $\underline{K}$ exist depending on the product of Maxwell-Wagner characteristic relaxation time and the frequency of the applied electric field. Please see Appendix I for the details of mathematical derivation of $\underline{K}$ for a conducting particle suspended in a dielectric liquid medium at DC field.

It is important to note that the experiments described in the current work were all effectively in the low frequency (DC) regime in which the effective polarizabilities and dipole moments are independent of frequency, and depend only on the difference in conductivities between the particle and fluid, as well as the particle geometry. In our work, the external field was at a frequency of 4 kHz, which is much less than the crossover frequences on the order of 1-10 MHz found by Krupke *et al.* in their experiments on DEP separation of SWNTs [59]. The applicability of the low-frequency limit to our experiments is also attested by later experiments described in Sec. **3.1.3** which verified the insensitivity of the ER behavior to the frequency of the applied field within the range 100 Hz - 10 kHz.

In the DC or low-frequency regime, the ratio of the parallel component of the effective polarization of a lossy prolate spheroidal particle to the effective polarization of a

lossy spherical particle is

$$
\begin{aligned}
\frac{|P_{eff_{ps\parallel}}|}{|P_{eff_{sp}}|} &= \frac{|p_{eff_{ps\parallel}}/v_{ps}|}{|p_{eff_{sp}}/v_s|} \\
&= \frac{\frac{\sigma_p-\sigma_f}{3[\sigma_f+(\sigma_p-\sigma_f)L_\parallel]}}{\frac{\sigma_p-\sigma_f}{\sigma_p+2\sigma_f}} \\
&= \frac{1+2\frac{\sigma_f}{\sigma_p}}{3\left[\frac{\sigma_f}{\sigma_p}+\left(1-\frac{\sigma_f}{\sigma_p}\right)L_\parallel\right]}.
\end{aligned}
\tag{2.28}
$$

Substituting Eq. (2.21) into Eq. (2.28), the ratio of polarizations for prolate and spheroidal particles can be expressed as a function of the particle aspect ratio r_e and the conductivity ratio $\frac{\sigma_p}{\sigma_f}$. Fig. 2.2 shows the ratio of effective polarization in terms of r_e at different $\frac{\sigma_p}{\sigma_f}$ values. As seen in the figure, highly anisotropic particles like SWNTs $(r_e \sim 10^3)$ can have polarization much higher than that of spherical particles. This is an important difference between ER fluids containing SWNTs or other high aspect ratio nano-particles and conventional ER fluid using spherical particles. As we will see in Sec. **3.1.4** , this is also believed to be one of the reasons that lower particle concentrations are required for ER fluids based upon highly anisotropic particles to obtain the same ER effect as those containing spherical particles, assuming all other physical properties of the particles remain the same.

2.1.3   Electrostatic forces and torques applied on an ellipsoidal particle with ohmic loss in dielectric medium with ohmic loss in an AC field

When an ellipsoidal particle polarizes in an external electric field, the field will exert force and torque on the particle which tries to move and rotate the particle. In the meanwhile, neighboring polarized particles will also interact with each other. The following part reviews the methods used to evaluate the force and torque applied to the particles by the electric field as well as the particle-particle interaction force.

a. Force and torque applied by the external electric field

The expressions for instantaneous force and torque applied on a dipole by a time-dependent electric field are

$$\vec{F}_{dep}(t) = \vec{p}_{eff} \cdot \bigtriangledown \vec{E}(t) \tag{2.29}$$

$$\vec{T}^e(t) = \vec{p}_{eff} \times \vec{E}(t).$$

$\vec{F}_{dep}$ is the so-called dielectrophoretic (DEP) force which is exerted on a polarizable particle when it is subjected to a non-uniform electric field. The strength of the force depends on the surrounding medium and particle's electrical properties, on the particle's shape and size, as well as on the frequency of the electric field. $\vec{T}^e$ is the torque applied by the electric field which drives the ellipsoidal particle to rotate and align its major axis in the direction of the electric field.

For a particle with permittivity ϵ_p and conductivity σ_p in a liquid medium with permittivity ϵ_f and conductivity σ_f subject to an AC electric field, the general expression of the DEP force and the torque applied by the field based on effective moment method is given by Jones [58]

$$\vec{F}_{dep}(t) = \mathbf{Re}\left[\underline{\vec{p}}_{eff}\exp\left(j\omega t\right)\right] \cdot \bigtriangledown \mathbf{Re}\left[\underline{\vec{E}}\exp\left(j\omega t\right)\right]$$

$$\vec{T}^e(t) = \mathbf{Re}\left[\underline{\vec{p}}_{eff}\exp\left(j\omega t\right)\right] \times \mathbf{Re}\left[\underline{\vec{E}}\exp\left(j\omega t\right)\right]. \tag{2.30}$$

These equations indicate that both force and torque by the electric field have a time-dependent part and a DC part. The time averaged DC part can be further simplified as

$$< \vec{F}_{dep}(t) > = \frac{1}{2}\mathbf{Re}\left[\underline{\vec{p}}_{eff} \cdot \bigtriangledown \underline{\vec{E}}^*\right] \tag{2.31}$$

$$< \vec{T}^e(t) > = \frac{1}{2}\mathbf{Re}\left[\underline{\vec{p}}_{eff} \times \underline{\vec{E}}^*\right]. \tag{2.32}$$

The asterisk signifies complex conjugation. For an ellipsoidal particle polarized by an external electric field the effective moment can be obtained as:

$$\underline{\vec{p}}_{eff} = 4\pi a_1 a_2 a_3 \epsilon_f \underline{\widetilde{K}} \cdot \underline{\vec{E}}_0, \tag{2.33}$$

where $\underline{\widetilde{K}}$ is the complex tensor form of Clausius-Mossotti function with components in the form of Eq. (2.23)

$$\widetilde{\underline{K}} = \begin{pmatrix} \underline{K}_{x_1} & 0 & 0 \\ 0 & \underline{K}_{x_2} & 0 \\ 0 & 0 & \underline{K}_{x3} \end{pmatrix}. \tag{2.34}$$

In a linearly polarized AC field where

$$\underline{\vec{E}}_0 = \mathbf{Re}\left(\underline{\vec{E}}_0\right) = \mathbf{Re}\left(\underline{\vec{E}}_0^*\right) = \vec{E}_0, \tag{2.35}$$

the time averaged DEP force applied by the field can be obtained by replacing the complex effective moment in Eq. (2.31) with Eq. (2.33). In a Cartesian coordinate system the explicit form of DEP force is

$$< \vec{F}_{dep}(t) >= \frac{1}{2}\mathbf{Re}\left[4\pi a_1 a_2 a_3 \epsilon_f \left(\underline{K}_{x_1} E_{0,x_1} \frac{\partial}{\partial x_1} + \underline{K}_{x_2} E_{0,x_2} \frac{\partial}{\partial x_2} + \underline{K}_{x3} E_{0,x_3} \frac{\partial}{\partial x_3}\right) \vec{E}_0\right]. \tag{2.36}$$

Similarly the time averaged alignment torque applied on the ellipsoid by the field is

$$\begin{aligned} < \vec{T}^e(t) >_i &= \frac{1}{2}\left[4\pi a_1 a_2 a_3 \epsilon_f E_{0,j} E_{0,k} \mathbf{Re}\left(\underline{K}_j - \underline{K}_k\right)\right] \\ &= \frac{2}{3}\pi a_1 a_2 a_3 \epsilon_f \left(L_k - L_j\right) E_{0,j} E_{0,k} \mathbf{Re}\left[\underline{K}_j \underline{K}_k\right]. \end{aligned} \tag{2.37}$$

Note that no Einstein's summation is applied in this work unless otherwise stated. The subscripts i, j, k here are ordered according to right-hand rule, that is, $x_1 \to x_2 \to x_3 \to x_1$.

b. Force due to the induced dipole interaction of ellipsoidal particles

Consider a pair of ellipsoidal particles in an external electric field. Both particles are polarized by the field, and we assume only dipoles are induced and neglect quadrupoles and other higher order terms. To lowest order, the induced dipole moment of one particle generates a local non-uniform electric field which applies a force on the other particle. This is the source of neutrally charged particle-particle interaction. The general equation for the DEP force as in Eq. (2.29) is still valid except the electric field now is the field generated by the dipole moment of the other particle instead of the applied external field.

Fig. 2.3 shows two prolate particles in an uniform electric field with their major axes parallel to each other and in $x_2 x_3$ plane. The electric field generated at a location
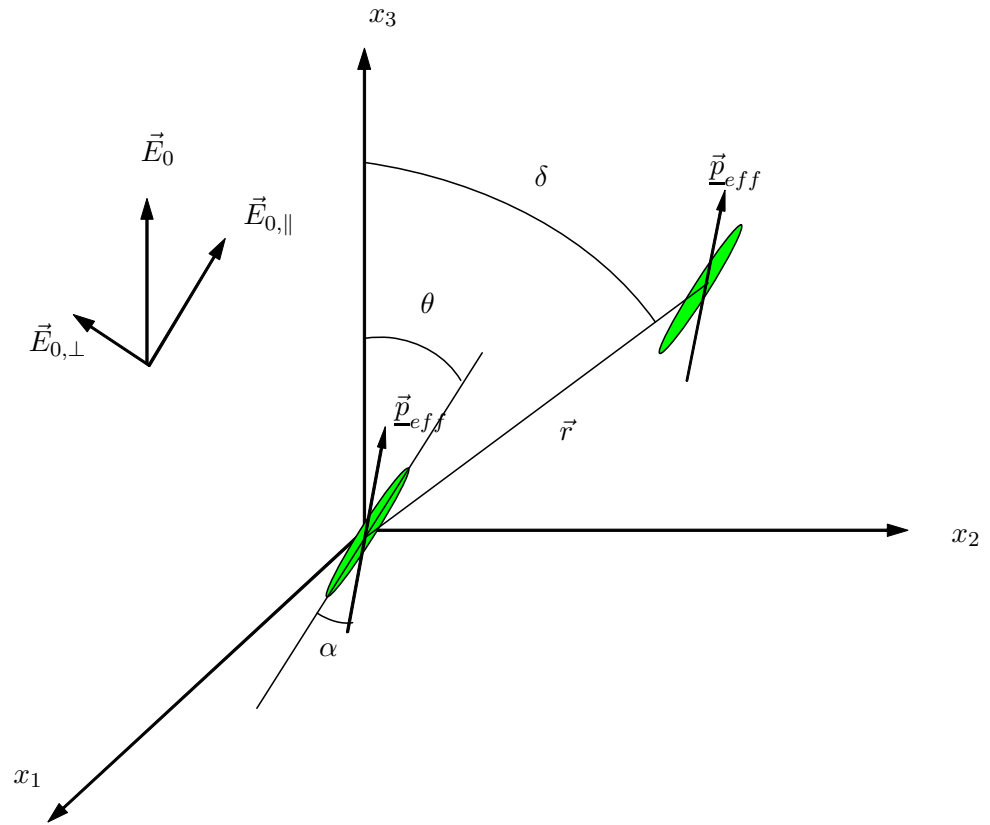
Figure 2.3: Two lossy dielectric prolates with major axes parallel to each other in an uniform electric field $\vec{E}_0$.

$\vec{r}$ by a particle of effective moment $\vec{p}_{eff}$ centered at origin is [60]

$$\vec{E}\left(\vec{r}\right) = \left(\frac{1}{4\pi\epsilon_f}\right) \frac{\left[3\left(\vec{p}_{eff}\cdot\hat{\vec{r}}\right)\hat{\vec{r}} - \vec{p}_{eff}\right]}{r^3}, \qquad (2.38)$$

where the unit vector $\hat{\vec{r}} = \vec{r}/r$ in the direction of the line connecting the centers of the two particles is

$$\hat{\vec{r}} = \cos\left(\delta - \phi\right)\hat{\vec{e}}_\| - \sin\left(\delta - \phi\right)\hat{\vec{e}}_\perp. \qquad (2.39)$$

$\hat{\vec{e}}_\|$ and $\hat{\vec{e}}_\perp$ are unit vectors parallel and perpendicular to the major axes of the particles.

The time-averaged DEP force in Eq. (2.31) can be reformed by using the relation

$$\underline{\vec{p}}_{eff}\cdot\triangledown\underline{\vec{E}}^* = \triangledown\left(\underline{\vec{p}}_{eff}\cdot\underline{\vec{E}}^*\right) - \underline{\vec{p}}_{eff}\times\left(\triangledown\times\underline{\vec{E}}^*\right). \qquad (2.40)$$

For a DC or low frequency AC field the second term on the right hand side of Eq. (2.40) equals zero. The time-averaged DEP force then becomes:

$$< \vec{F}_{dep}(t) > = \frac{1}{2}\mathbf{Re}\triangledown\left[\underline{\vec{p}}_{eff}\cdot\underline{\vec{E}}^*\right]. \qquad (2.41)$$

Inserting Eq. (2.38) into Eq. (2.41) the time-averaged DEP force on the particle at vector position $\vec{r}$ due to the field induced by the particle at origin can be expressed as

$$\begin{aligned} < \vec{F}_{dep}(t) > &= \frac{1}{2}\mathbf{Re}\triangledown\left[\underline{\vec{p}}_{eff}\cdot\underline{\vec{E}}^*\right] \\ &= \frac{1}{2}\mathbf{Re}\triangledown\left\{\underline{\vec{p}}_{eff}\cdot\left(\frac{1}{4\pi\epsilon_f}\right)\frac{1}{r^3}\left[3\left(\underline{\vec{p}}_{eff}\cdot\hat{\vec{r}}\right)\hat{\vec{r}} - \underline{\vec{p}}_{eff}\right]^*\right\} \\ &= \frac{1}{2}\mathbf{Re}\triangledown\left\{\left(\frac{1}{4\pi\epsilon_f}\right)\frac{1}{r^3}\left[3\left(\underline{\vec{p}}_{eff}\cdot\hat{\vec{r}}\right)\left(\underline{\vec{p}}_{eff}\cdot\hat{\vec{r}}\right)^* - \underline{\vec{p}}_{eff}\cdot\underline{\vec{p}}_{eff}^*\right]\right\} \\ &= \frac{1}{2}\triangledown\left\{\left(\frac{1}{4\pi\epsilon_f}\right)\frac{1}{r^3}\left(3|\underline{\vec{p}}_{eff}\cdot\hat{\vec{r}}|^2 - \|\underline{\vec{p}}_{eff}\|^2\right)\right\}, \qquad (2.42) \end{aligned}$$

where $|\underline{X}|$ is the modulus of a complex number $\underline{X}$.

In the case of a pair of prolate spheroids with high aspect ratio the expression of effective moment of Eq. (2.26) can be substituted into Eq. (2.42). Further simplification gives the dipole interaction force between two prolate spheroids in an AC field.

$$< \vec{F}_{dep}(t) >= -\frac{6\pi\epsilon_f a^2 b^4}{r^4} \left\{ \underline{K}_{\parallel}\underline{K}_{\parallel}^* E_{0,RMS,\parallel}^2 \left[3\cos^2(\delta-\theta) - 1 \right] \right.$$

$$+ \underline{K}_{\perp}\underline{K}_{\perp}^* E_{0,RMS,\perp}^2 \left[3\sin^2(\delta-\theta) - 1 \right]$$

$$+ 3E_{0,RMS,\parallel}E_{0,RMS,\perp}\sin\left[2(\delta-\theta)\right] \cdot$$

$$\left[\mathbf{Re}\left(\underline{K}_{\parallel}\right)\mathbf{Re}\left(\underline{K}_{\perp}\right) + \mathbf{Im}\left(\underline{K}_{\parallel}\right)\mathbf{Im}\left(\underline{K}_{\perp}\right) \right] \right\} \hat{\tilde{e}}_r$$

$$+ \frac{6\pi\epsilon_f a^2 b^4}{r^4} \left\{ \underline{K}_{\perp}\underline{K}_{\perp}^* E_{0,RMS,\perp}^2 \sin\left[2(\delta-\theta)\right] \right.$$

$$- \underline{K}_{\parallel}\underline{K}_{\parallel}^* E_{0,RMS,\parallel}^2 \sin\left[2(\delta-\theta)\right]$$

$$+ 2E_{0,RMS,\parallel}E_{0,RMS,\perp}\cos\left[2(\delta-\theta)\right] \cdot$$

$$\left[\mathbf{Re}\left(\underline{K}_{\parallel}\right)\mathbf{Re}\left(\underline{K}_{\perp}\right) + \mathbf{Im}\left(\underline{K}_{\parallel}\right)\mathbf{Im}\left(\underline{K}_{\perp}\right) \right] \right\} \hat{\tilde{e}}_\delta, \qquad (2.43)$$

where δ and θ are angles shown in Fig. 2.3, $E_{0,RMS,\parallel}$ and $E_{0,RMS,\perp}$ are RMS values of $E_{0,\parallel}$ and $E_{0,\perp}$ respectively.

In the special case of dielectric spheres in a fluid medium the induced effective moments are aligned with the direction of the electric field. So $E_{0,RMS,\perp} = 0$, $\underline{K}_{\perp} = 0$ and $\underline{K}_{\parallel} = \underline{K}$ in Eq. (2.43), which leads to the familiar expression of point-dipole interaction for spheres [31, 61]

$$< \vec{F}_{dep}(t) >= -\frac{6\pi\epsilon_f a^6}{r^4}\underline{K}\underline{K}^* E_{0,RMS}^2 \left\{ \left[3\cos^2(\delta) - 1\right]\hat{\tilde{e}}_r + \sin(2\delta)\hat{\tilde{e}}_\delta \right\}. \qquad (2.44)$$

Note that in both cases, the DEP force scales as $\frac{E_{0,RMS}^2}{r^4}$, although the prolate spheroid case is more complicated and depends on the orientation of the particle itself.

2.1.4   Motion of particles in shear and electric fields

Having reviewed how dielectric particles respond to a uniform electric field and their ensuing behavior, we now consider the motion of particles in a shear flow with or without external electric field.

a. Rotation of particles in Newtonian shear flow

Research on motion of particles in pure shear flow can be traced back to 1922 when Jeffery [45] first published his solution on a neutrally buoyant ellipsoidal particle

subjected to simple shear flow. In a Cartesian coordinate system fixed in the space at the center of the particle, the expression for the undisturbed simple shear flow field is

$$u_3 = \dot{\gamma} x_2; \quad u_1, \ u_2 = 0, \tag{2.45}$$

where u_i $(i = 1, 2, 3)$ are velocity components in x_i $(i = 1, 2, 3)$ axes, respectively and $\dot{\gamma}$ is the shear rate.

The angular velocity of Eulerian angles which will be defined later can be obtained from Jeffery's analysis as

$$\frac{d\phi}{dt} = \frac{\dot{\gamma}}{(r_e^2 + 1)} \left(r_e^2 \cos^2 \phi + \sin^2 \phi \right) \tag{2.46}$$

$$\frac{d\theta}{dt} = \frac{\dot{\gamma} \left(r_e{}^2 - 1 \right)}{4 \left(r_e^2 + 1 \right)} \sin 2\theta \sin 2\phi, \tag{2.47}$$

where the angles ϕ and θ are depicted in Fig. 2.4, and r_e is the aspect ratio of the spheroid. Eq. (2.46) and Eq. (2.47) can be integrated and yield

$$\tan \phi = r_e \tan \left(\frac{2\pi t}{T} + k_0 \right) \tag{2.48}$$

$$\tan \theta = \frac{C r_e}{\left(r_e^2 \cos^2 \phi + \sin^2 \phi \right)^{\frac{1}{2}}}, \tag{2.49}$$

where C is the orbit constant and k_0 is the initial phase angle. Both of them can be determined by the intial orientation of the particle. T is the period of rotation about the vorticity axis and is given by

$$T = \frac{2\pi}{\dot{\gamma}} \left(r_e + \frac{1}{r_e} \right). \tag{2.50}$$

A particle with $r_e > 1$ rotates more slowly when its major principle axis is aligned along the direction of the flow field. The orbits of the ends of the particle defined by Eq. (2.49) trace out a symmetrical pair of spherical ellipses whose eccentricity is described by the orbit constant C.

In a suspension system where many particles exist, the macroscopic properties of the suspension is determined by the distribution of particle orientations and the ensemble average of particle motions. Okagawa, Cox and Mason [62] made an argument that the orientation distribution function in terms of (ϕ, θ) can be converted to a distribution
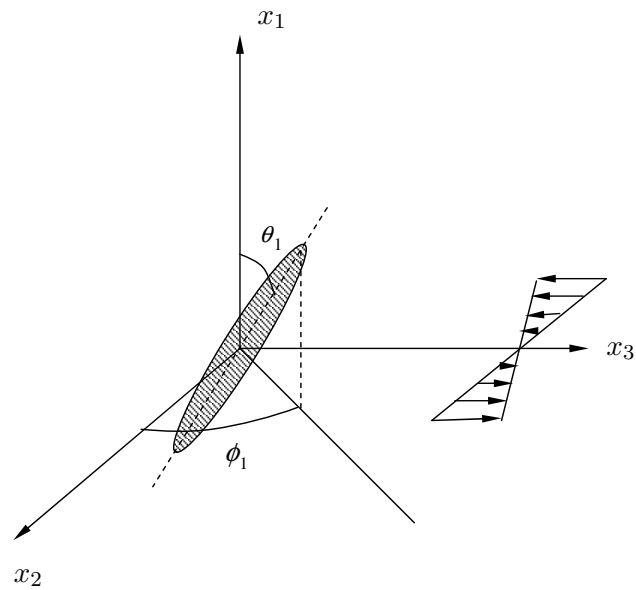
Figure 2.4: Coordinate system for a prolate spheroid in shear flow with its axis aligned at ϕ and θ. The pure shear flow is in $x_2 x_3$ plane.

function using the orbit constant C and the initial phase k_0 as two parameters. Based on this they derived the orientation distribution function as

$$p\left(\theta, \phi, r_e\right) = \frac{p_0\left(\tan^{-1}\left(\chi \tan \theta\right), \tan^{-1}\left(\frac{\tan \phi - r_e \tan \frac{2\pi t}{T}}{1 + r_e^{-1} \tan \theta \tan \frac{2\pi t}{T}}\right)\right)}{\chi\left(\cos^2 \theta + \chi^2 \sin^2 \theta\right)}, \qquad (2.51)$$

where

$$\begin{aligned}
\chi^2 &= \chi_1 \sin^2 \phi + \chi_2 \sin \phi \cos \phi + \chi_3 \cos^2 \phi, \\
\chi_1 &= \frac{1}{2}\left\{1 + r_e^{-2} + \left(1 - r_e^{-2}\right) \cos \frac{4\pi t}{T}\right\}, \\
\chi_2 &= \left(r_e^{-1} - r_e\right) \sin \frac{4\pi t}{T}, \\
\chi_3 &= \frac{1}{2}\left\{1 + r_e^2 + \left(1 - r_e^2\right) \cos \frac{4\pi t}{T}\right\}, \qquad (2.52)
\end{aligned}$$

and $p_0\left(\theta_0, \phi_0\right)$ is the initial orientation distribution. If an assumption has been made that the particles are initially randomly (isotropically) oriented, then the distribution function at time t will be

$$p\left(\theta, \phi, r_e\right) = \frac{\sin \theta}{4\pi\left(\cos^2 \theta + \chi^2 \sin^2 \theta\right)^{\frac{3}{2}}}. \qquad (2.53)$$

A real colloidal suspension is polydispersed and the co-existence of various sizes and shapes of particles is common. In this case, the probability distribution of particle aspect ratios r_e has to be taken into account when we calculate the orientation distribution function. The expression of the orientation distribution function with a given shape distribution function $g(r_e)$ is

$$p_\sigma\left(\theta, \phi\right) = \int_0^\infty p\left(\theta, \phi\right) g\left(r_e\right) dr_e, \qquad (2.54)$$

where $p_\sigma\left(\theta, \phi\right)$ is called the probability orientation distribution.

The suspension system starts to exhibit damped oscillations in time as the result of polydispersity which leads to the phase mixing of particle orbits. Therefore particles will eventually reach a time-independent steady state.

b. Rotation of particles in both shear and electric field

b.1 Hydrodynamic torque on an ellipsoid

For a rigid ellipsoid suspended in a viscous Newtonian fluid at creeping flow region, the force per unit area applied on the surface of the particle can be determined and hence

the hydrodynamic torque referring to the moving Cartesian coordinates x'_i $(i = 1, 2, 3)$ is

$$\Gamma'_{Hi} = \frac{16\pi\eta_c \left(a_j^2 + a_k^2\right)}{3 \left(a_j^2\alpha_j + a_k^2\alpha_k\right)} \times \left(\frac{a_j^2 - a_k^2}{a_j^2 + a_k^2} s_{jk'} + \zeta'_i - \omega'_i\right), \tag{2.55}$$

which is equivalent to equation (36) in [45]. Each a_i $(i = 1, 2, 3)$ is the semi-axis of the ellipsoid along the ith principle axis, while $s_{jk'}$ are components of distortion of fluid and ζ'_i are components of rotation of fluid. The ω'_i are the components of particle's angular velocity, and α_i is defined as

$$\alpha_i = \int_o^\infty \frac{d\lambda}{\left(a_i^2 + \lambda\right) \left[\left(a_1^2 + \lambda\right) \left(a_2^2 + \lambda\right) \left(a_3^2 + \lambda\right)\right]^{\frac{1}{2}}}. \tag{2.56}$$

b.2 Electrostatic torque on an ellipsoid

As discussed in previous sections, a dipole moment will be induced if a dielectric particle is put in a uniform electric field. We assume that the ellipsoidal particle does not have a permanent dipole and the electric permittivity tensor of the particle only has three diagonal components so that

$$\epsilon_{ij} = \delta_{ij}\epsilon_{ij}, \tag{2.57}$$

where δ_{ij} is the Kronecker delta.

In this case, an electrostatic torque $\mathbf{\Gamma'_E}$ will be applied on the particle by the field

$$\mathbf{\Gamma'_E} = \mathbf{p'} \times \mathbf{E'_0}, \tag{2.58}$$

where $\mathbf{p'}$ is the induced dipole moment and the $'$ means relative to the x'_i coordinates. Okagawa and Mason [63] derived an explicit expression of the total electric torque acting on the ellipsoid:

$$\Gamma'_{Ei} = \frac{4\pi}{3}a_1 a_2 a_3 \epsilon_f \left(\frac{\epsilon_p}{\epsilon_f} - 1\right) \times \epsilon_{ijk} \frac{E'_{0j}E'_{0k}}{1 + \frac{1}{2}a_1 a_2 a_3 \left(\frac{\epsilon_p}{\epsilon_f} - 1\right)\alpha_j}, \tag{2.59}$$

where ϵ_{ijk} is the Levi-Civita symbol. This equation is equivalent to Eq. (2.37), where the particle has ohmic loss and the torque there is time-averaged. To keep consistant with the discussion in Okagawa and Mason's paper [63], in the following we use the torque form of Eq. (2.59).

b.3 Angular velocity and rotation under both shear and electric field

When an ellipsoid is in both viscous shear flow and an electric field, the total torque $\mathbf{\Gamma'}$ can be determined by the principle of superposition:

$$\mathbf{\Gamma'} = \mathbf{\Gamma'_H} + \mathbf{\Gamma'_E}. \tag{2.60}$$

At equilibrium the hydrodynamic torque and the electrostatic torque balance each other. Substituting $\mathbf{\Gamma'_H}$ and $\mathbf{\Gamma'_E}$ with the expressions in Eq. (2.55) and Eq. (2.59) yields the angular velocity ω'_i of the ellipsoid relative to x'_i coordinates

$$\omega'_1 = \frac{a_2^2 - a_3^2}{a_2^2 + a_3^2} s'_{23} + \zeta'_1 + \frac{a_1 a_2 a_3 \left(a_2^2 \alpha_2 + a_3^2 \alpha_3\right)}{16 \pi \eta_c \left(a_2^2 + a_3^2\right)} \epsilon_f \left(\frac{(q'_{22} - 1)}{1 + \frac{1}{2} a_1 a_2 a_3 (q'_{22} - 1) \alpha_2} \right.$$
$$\left. - \frac{(q'_{33} - 1)}{1 + \frac{1}{2} a_1 a_2 a_3 (q'_{33} - 1) \alpha_3} \right) E'_{02} E'_{03} \tag{2.61}$$

$$\omega'_2 = \frac{a_3^2 - a_1^2}{a_3^2 + a_1^2} s'_{31} + \zeta'_2 + \frac{a_1 a_2 a_3 \left(a_3^2 \alpha_3 + a_1^2 \alpha_1\right)}{16 \pi \eta_c \left(a_3^2 + a_1^2\right)} \epsilon_f \left(\frac{(q'_{33} - 1)}{1 + \frac{1}{2} a_1 a_2 a_3 (q'_{33} - 1) \alpha_3} \right.$$
$$\left. - \frac{(q'_{11} - 1)}{1 + \frac{1}{2} a_1 a_2 a_3 (q'_{11} - 1) \alpha_1} \right) E'_{03} E'_{01} \tag{2.62}$$

$$\omega'_3 = \frac{a_1^2 - a_2^2}{a_1^2 + a_2^2} s'_{12} + \zeta'_3 + \frac{a_1 a_2 a_3 \left(a_1^2 \alpha_1 + a_2^2 \alpha_2\right)}{16 \pi \eta_c \left(a_1^2 + a_2^2\right)} \epsilon_f \left(\frac{(q'_{11} - 1)}{1 + \frac{1}{2} a_1 a_2 a_3 (q'_{11} - 1) \alpha_1} \right.$$
$$\left. - \frac{(q'_{22} - 1)}{1 + \frac{1}{2} a_1 a_2 a_3 (q'_{22} - 1) \alpha_2} \right) E'_{01} E'_{02}. \tag{2.63}$$

As illustrated in Fig. 2.5 we define the coordinate system x_i $(i = 1, 2, 3)$ as fixed coordinate system in space with the origin at the center of the ellipsoid and x'_i $(i = 1, 2, 3)$ as body coordinates which adhere to the particle. Then the orientation of the particle can be described by the three Eulerian angles θ, ϕ, ψ, with θ being the angle between the axes of x_1 and x'_1, ϕ being the angle between x_2 axis and *the line of the nodes* which is defined as the intersection of plane $x_2 x_3$ and plane $x'_2 x'_3$, ψ being the angle between *the line of the nodes* and x'_2 axis.
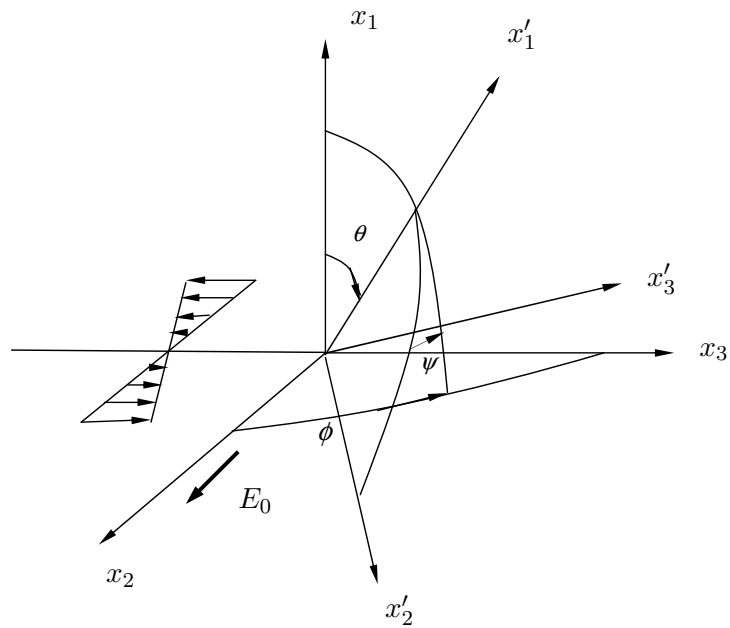
Figure 2.5: Configuration of space fixed coordinate system x_i $(i = 1, 2, 3)$, body fixed coordinate system x'_i $(i = 1, 2, 3)$ and Eulerian angles θ, ϕ, ψ.

The rates of the change of these angles are related to the angular velocity [64] as

$$\frac{d\theta}{dt} = \omega_2' \sin\psi + \omega_3' \cos\psi \tag{2.64}$$

$$\frac{d\phi}{dt} = \left(\omega_3' \sin\psi - \omega_2' \cos\psi\right) \csc\theta \tag{2.65}$$

$$\frac{d\psi}{dt} = \omega_1' - \left(\omega_3' \sin\psi - \omega_2' \cos\psi\right) \cot\theta. \tag{2.66}$$

In a special case where the electric field is applied parallel to the x_2 axis and the particle is electrically conductive and axisymmetric, further simplification of equations (2.64~2.66) can be performed once the angular velocity has been substituted by Eq. (2.61~2.63) for a prolate spheroid:

$$\frac{d\theta}{dt} = \frac{\dot\gamma\left(r_e^2 - 1\right)}{4\left(r_e^2 + 1\right)} \sin 2\phi \sin 2\theta - \frac{\epsilon_f P\left(r_e\right)}{\eta_c} E_0^2 \cos^2\phi \sin 2\theta \tag{2.67}$$

$$\frac{d\phi}{dt} = \frac{\dot\gamma}{r_e^2 + 1}\left(r_e^2 \cos^2\phi + \sin^2\phi\right) + \frac{\epsilon_f P\left(r_e\right)}{\eta_c} E_0^2 \sin 2\phi, \tag{2.68}$$

where

$$P(r_e) = \frac{(3A - 2)\,Q(r_e)}{8\pi A\,(A - 1)}$$

$$Q(r_e) = \frac{2r_2^2 + \left(1 - 2r_e^2\right)A}{4\left(r_e^2 + 1\right)}, \tag{2.69}$$

and

$$A = \frac{r_e^2}{r_e^2 - 1} - \frac{r_e \cosh^{-1}(r_e)}{\left(r_e^2 - 1\right)^{\frac{3}{2}}} \qquad r_e > 1,$$

$$A = \frac{r_e \cos^{-1}(r_e)}{\left(1 - r_e^2\right)^{\frac{3}{2}}} - \frac{r_e^2}{1 - r_e^2} \qquad r_e < 1,$$

$$A = \frac{2}{3} \qquad r_e = 1. \tag{2.70}$$

Integration of Eq. (2.67) and Eq. (2.68) yields

$$\tan\theta = \frac{C r_e}{\left(r_e^2 \cos^2\phi + \sin^2\phi - f r_e \sin 2\phi\right)^{\frac{1}{2}}} \times \exp\left(\frac{-\epsilon_f P\left(r_e\right)}{\eta_c} E_0^2 t\right) \tag{2.71}$$

$$\tan\phi = r_e\left(1 - f^2\right)^{\frac{1}{2}} \times \tan\left(\frac{2\pi t}{T} + k_0\right) + f r_e, \tag{2.72}$$

where C and k_0 are integration constants. T is the period of the rotation about the vorticity axis which is given by

$$T = \frac{2\pi}{\dot\gamma\left(1 - f^2\right)^{\frac{1}{2}}}\left(r_e + r_e^{-1}\right), \tag{2.73}$$

and f is a dimensionless quantity which is defined by

$$f = \frac{-\epsilon_f P\left(r_e\right) E_0^2 \left(r_e^2 + 1\right)}{\dot{\gamma}\eta_c r_e}. \tag{2.74}$$

It can be seen from Eq. (2.73) that the rotation period becomes infinite and imaginary when f^2 equals to 1 and greater than 1 respectively. This means the particle can no longer complete one full rotation and a critical field strength corresponding to $f^2 = 1$ exists and is given by

$$E_{crit}^2 = \left| \frac{-r_e \eta_c \dot{\gamma}}{\epsilon_f P(r_e)(r_e + 1)} \right|. \tag{2.75}$$

In cases where external electric fields are greater than the above critical field the particle will eventually reach a steady state at which both Eq. (2.67) and Eq. (2.68) equal zero. The orientation angles of a prolate particle at steady state are

$$\theta_{1\infty} = \frac{\pi}{2} \tag{2.76}$$

$$\phi_{1\infty} = \tan^{-1}\{r_e[f - (f^2 - 1)^{\frac{1}{2}}]\}, \tag{2.77}$$

which means the particle eventually will lie on the $x_2 x_3$ plane and that the particle equilibrium angle $\phi_{1\infty}$ will depend on the dimensionless parameter f which is a function of field strength, aspect ratio of the particle, shear rate and the viscosity and permittivity of the base fluid. Figure 2.6 shows the variation of $\phi_{1\infty}$ with $E_0^2/\dot{\gamma}$ for particles having different aspect ratios. As can be seen in the figure, at low electric field strength and high shear rates, the particles are aligned with the flow direction with $\phi_{1\infty} = 90°$ while at high electric field and low shear rates, the particles are oriented in the direction of the electric field. As will be discussed in more detail later in Sec. **4.5**, calculations of E_{crit} for a typical case of our experiment lead to a value of 27.35 V/mm. As the external electric fields applied in these cases are normally above 100 V/mm, thus all the following discussion will be based on the case when $f^2 > 1$ and $E_0 > E_{crit}$, *i.e.*, the particle is no longer rotating but is in equilibrium.

Another key point that Fig. 2.6 illustrates is the fact that the model predictions of the equilibrium particle orientation angle are seen to be essentially independent of the

aspect ratio in the high-aspect-ratio range (for aspect-ratio higher than 10). Thus, the polydispersity (*i.e.*, the broad distribution of nanotube lengths) in actual samples is irrelevant to the orientation angles predicted by the model. However, the dimensionless parameter f itself under a typical lab condition relies much on the particle aspect-ratio as depicted in Fig. 2.7.
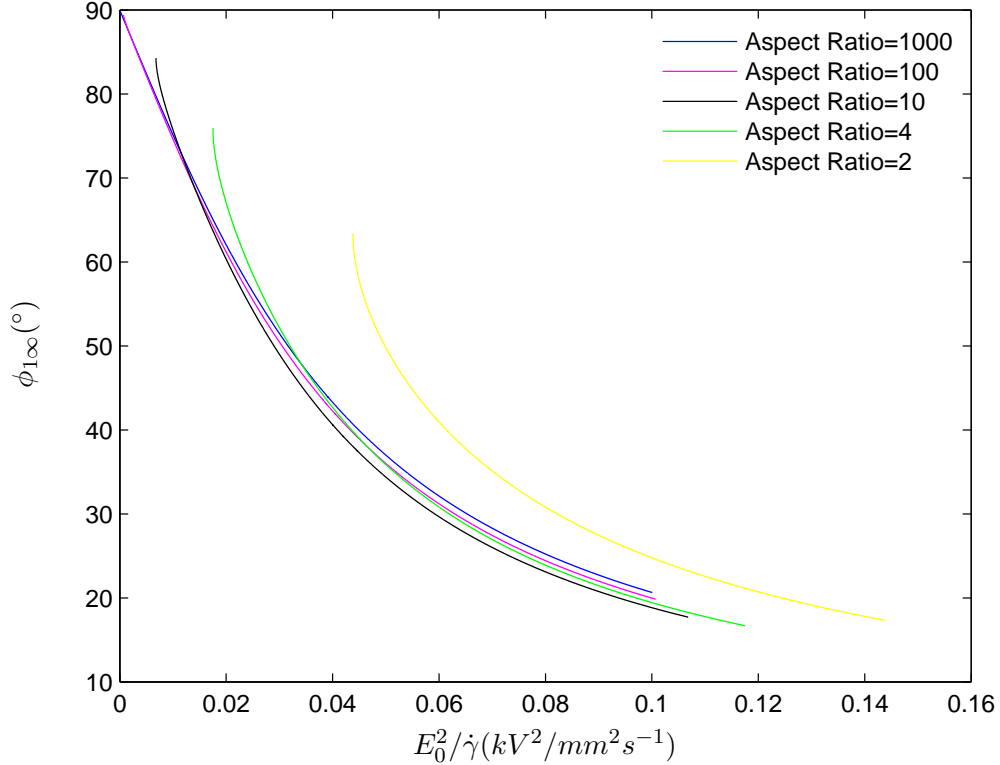
Figure 2.6: Equilibrium orientation angle $\phi_{1\infty}$ varies with $E_0^2/\dot{\gamma}$ for particles having different aspect ratios.

Similar to the case where particles are undergoing only shear flow, the orientation distribution function for dilute suspension at both shear and electric field can be obtained. For a random initial orientation condition, Mason and coworkers [63] derived the mathematical form of the distribution function

$$p_t(\theta, \phi) = \frac{\sin\theta}{4\pi\left(\cos^2\theta + \chi^2\sin^2\theta\right)^{\frac{3}{2}}}\exp\left(\frac{2\epsilon_f P(r_e)}{\eta_c}E_0^2 t\right), \qquad (2.78)$$

where

$$\chi^2 = \left(\chi_1\sin^2\phi + \chi_2\sin\phi\cos\phi + \chi_3\cos^2\phi\right)\exp\left(\frac{2\epsilon_f P(r_e)}{\eta_c}E_0^2 t\right). \qquad (2.79)$$
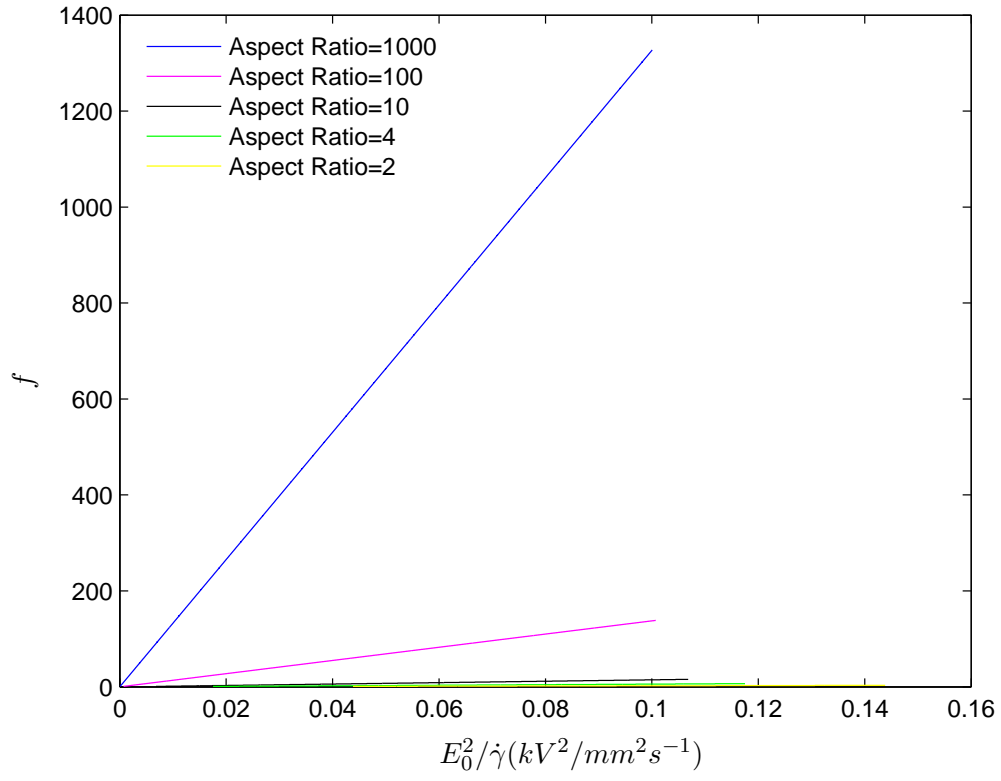
Figure 2.7: Dimensionless parameter f varies with $E_0^2/\dot{\gamma}$ for particles having different aspect ratios.

Equations of χ_1, χ_2 and χ_3 in three different cases according to the strength of applied electric field E_0 are tabulated by Mason [63].
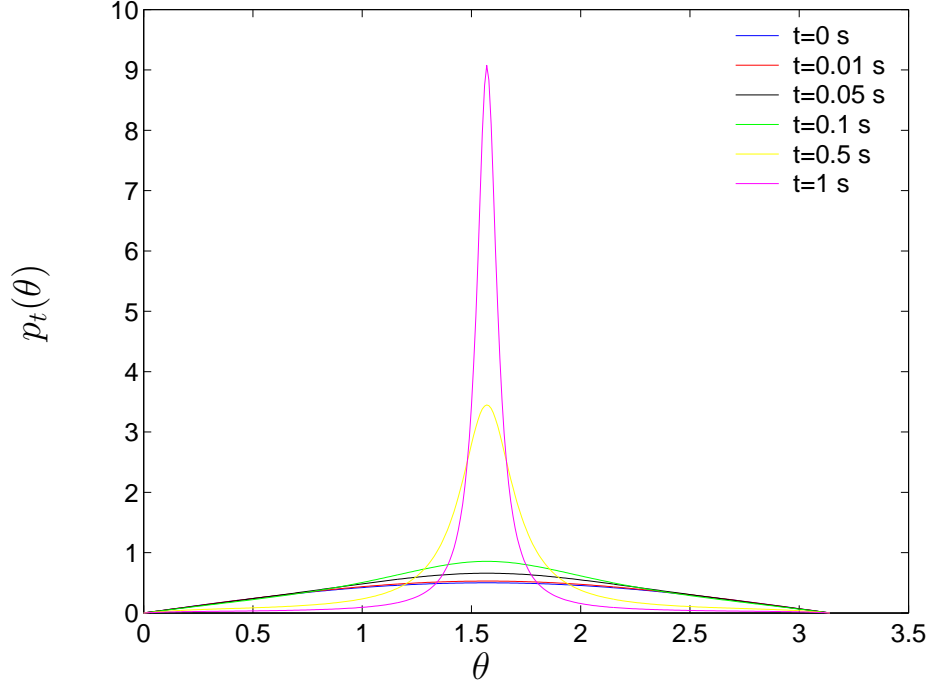
Figure 2.8: Separate probability distribution in terms of θ at different time intervals. Typical values chosen to calculate f are: $\epsilon_f = 2.8\epsilon_0, P = -0.02157, \dot{\gamma} = 10s^{-1}, E_0 = 200V/mm, r_e = 1000, \eta_c = 40cP$.

The individual probability distribution of θ and ϕ can be obtained by the integration of Eq. (2.78) as

$$\begin{aligned} p_t(\theta) &= \int_0^{2\pi} p_t(\theta, \phi) d\phi \\ &= \frac{\sin\theta}{\pi m_1^{\frac{1}{2}} m_2} E(k_m) \exp\left(\frac{2\epsilon_f P r_e}{\eta_c} E_0^2 t\right) \end{aligned} \tag{2.80}$$

and

$$\begin{aligned} p_t(\phi) &= \int_0^{\pi} p_t(\theta, \phi) d\theta \\ &= \frac{1}{2\pi \left(\chi_1 \sin^2\phi + \chi_2 \sin\phi \cos\phi + \chi_3 \cos^2\phi\right)}, \end{aligned} \tag{2.81}$$

where $E(k_m)$ is the complete elliptic integral of the second kind with modulus $k_m =$

$1 - \frac{m_1}{m_2}$ and

$$m_1 = \cos^2\theta + \frac{1}{2}\{\chi_1 + \chi_3 + [(\chi_3 - \chi_1)^2 + \chi_2^2]^{\frac{1}{2}}\}\sin^2\theta\exp\left(\frac{2\epsilon_f P_{r_e}}{\eta_c}E_0^2 t\right) \qquad (2.82)$$

$$m_2 = \cos^2\theta + \frac{1}{2}\{\chi_1 + \chi_3 - [(\chi_3 - \chi_1)^2 + \chi_2^2]^{\frac{1}{2}}\}\sin^2\theta\exp\left(\frac{2\epsilon_f P_{r_e}}{\eta_c}E_0^2 t\right). \qquad (2.83)$$

Figures 2.8 and Fig. 2.9 show the separate probability distribution of θ and ϕ respectively at different time intervals. All particles are approaching to an equilibrium state with the steady orientation angles defined by Eq. (2.76) and Eq. (2.77). Notice that the time scales for both probability distribution of θ and ϕ to reach to their equilibrium state are within about one or two seconds. Experimentally, it is difficult for us to capture the dynamics of this orienting process at these rapid time scales. In the following chapters, we will focus on the equilibrium orientation angles predicted by Eq. 2.77.
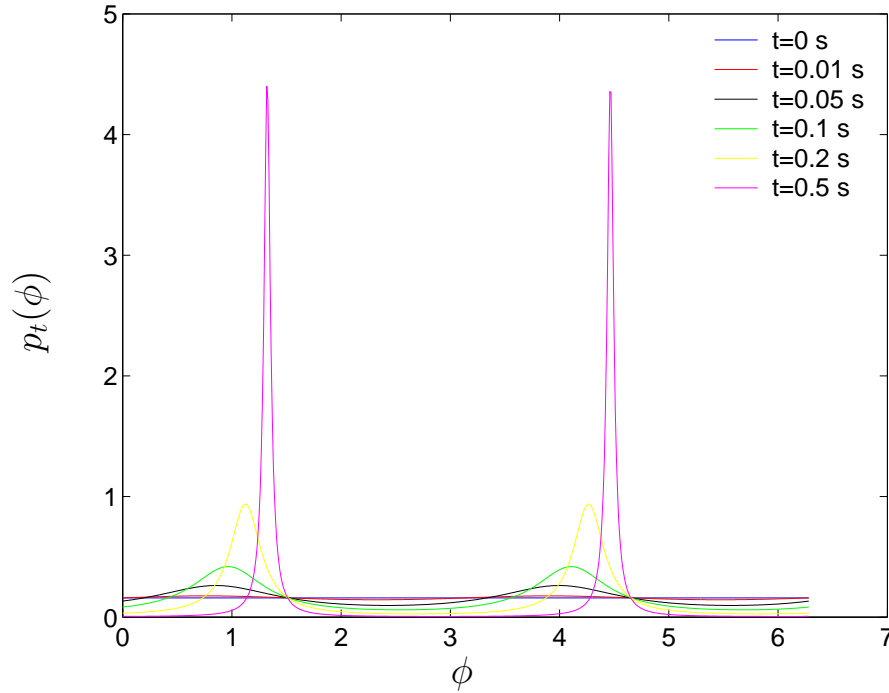
Figure 2.9: Separate probability distribution in terms of ϕ at different time intervals.

2.2 Light scattering by small particles

From the previous discussion a colloidal suspension of ellipsoidal/cylindrical particles exhibits a preferential orientation upon the application of external fields, which can

be a hydrodynamic flow field, an electric field or a magnetic field. This orientational anisotropy usually induces changes of optical properties of the colloidal system. These changes of optical properties would allow us to probe the microstructure of colloidal suspensions subjected to external fields. Many applications have been carried out based on polarimetry or the analysis of the interaction of polarized light with sample suspensions. The most common material properties which are involved in these analysis are linear dichroism and linear birefringence. Both of them are related to the refractive index of the sample suspension, which can be represented as a complex tensor

$$\widetilde{n} = \left\{ \begin{array}{ccc} n_{11} & n_{12} & n_{13} \\ n_{21} & n_{22} & n_{23} \\ n_{31} & n_{32} & n_{33} \end{array} \right\}, \tag{2.84}$$

where

$$\widetilde{n} = \widetilde{n}' - i\widetilde{n}''. \tag{2.85}$$

The linear birefringence $\Delta n'$ and linear dichroism $\Delta n''$ are defined as the difference of the principle eigenvalues of the tensor $\widetilde{n}'$ and $\widetilde{n}''$ respectively.

According to Van de Hulst's treatise on light scattering by small particles, the interaction of a plane incident wave with a scattering particle can be described by four amplitude functions, S_1, S_2, S_3, S_4, which are all functions of θ_1 and ϕ_1 as illustrated in Fig. 2.10. These amplitude functions form a matrix called the scattering matrix, which relates the electric vector of the incident light to that of outgoing scattered light. In our discussion only forward scattering is considered, so the angle θ_1 becomes 0. Using the notation of Van de Hulst in a Cartesian coordinate system, the relation can be described as

$$\left(\begin{array}{c} E_x \\ E_y \end{array} \right) = \left(\begin{array}{cc} S_2(0) & S_3(0) \\ S_4(0) & S_1(0) \end{array} \right) \cdot \frac{e^{-ikr+i\omega t}}{ikr} \left(\begin{array}{c} E_{x0} \\ E_{y0} \end{array} \right), \tag{2.86}$$

where $\left(\begin{array}{c} E_{x0} \\ E_{y0} \end{array} \right)$ is the field vector of the incident light at the location of the particle (the origin), r is the distance between the origin and an arbitrary point in space where the field vector of the scattered light is calculated, and $k = \frac{2\pi}{\lambda}$ is the wave number with λ being the wavelength of the light.
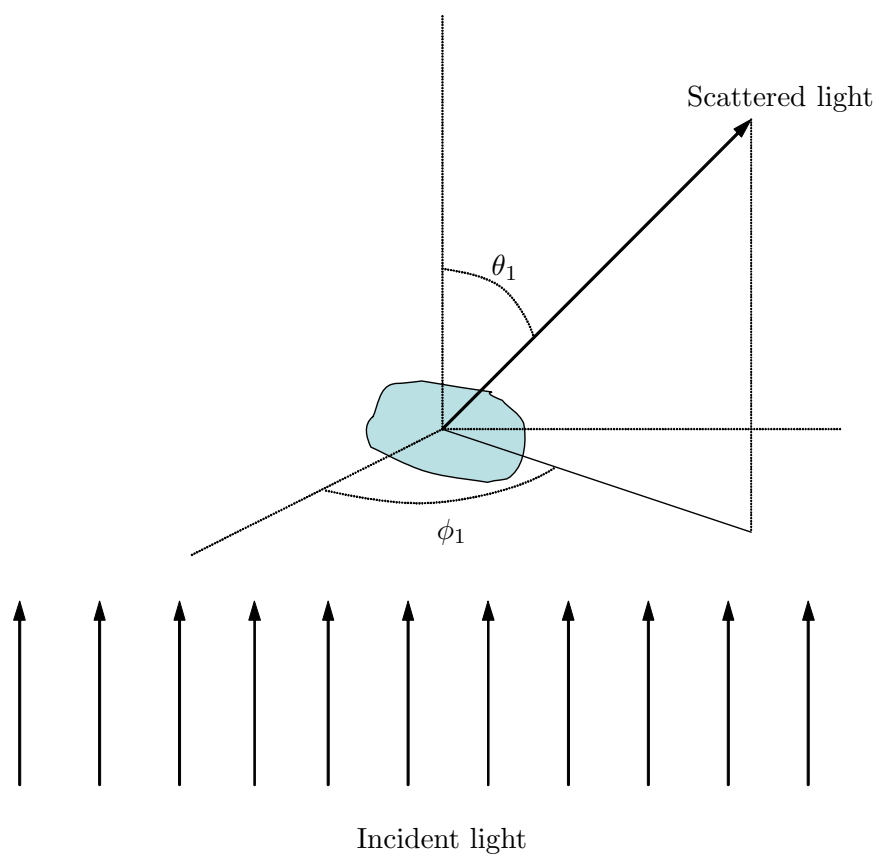
Figure 2.10: Definition of scattering angle.

Van de Hulst shows that the phase lag of the wave which is represented by the linear birefringence $\widetilde{n}'$ and the intensity decrease of the wave by the linear dichroism $\widetilde{n}''$ are related to the tensor form of scattering matrix by

$$\widetilde{n}' = \widetilde{I} + \frac{2\pi n_f N}{k^3}\mathbf{Im}\{\widetilde{S}(0)\} \tag{2.87}$$

$$\widetilde{n}'' = \frac{2\pi n_f N}{k^3}\mathbf{Re}\{\widetilde{S}(0)\}, \tag{2.88}$$

where n_f is the refractive index of the fluid and $\widetilde{I}$ is the identity tensor.

When only particles small in size compared to the wavelength of light are considered, the tensor form of the scattering matrix can be expanded in the power series of the wavenumber [65, 66]. Approximations can be made by only maintaining the first real and imaginary terms of the expansion which also agrees with the expression Van de Hulst obtained from the expansion of higher order terms for spherical particles.

$$\widetilde{S}(0) = ik^3\widetilde{\alpha} + \frac{2}{3}k^6\widetilde{\alpha}^2, \tag{2.89}$$

where $\widetilde{\alpha}$ is the polarizability tensor with 3 indices. Since $\widetilde{S}(0)$ is normally a tensor with 2 indices, care has to be taken when different light propagation directions are considered. With the shear flow defined as

$$u_3 = \dot{\gamma}y$$

$$u_1 = 0$$

$$u_2 = 0,$$

only light propagating in the x_1 direction need be considered in this thesis. For a prolate spheroidal particle with uniaxial polarizability, $\widetilde{\alpha}$ may be written as

$$\widetilde{\alpha} = \begin{pmatrix} \alpha_a & 0 & 0 \\ 0 & \alpha_b & 0 \\ 0 & 0 & \alpha_b \end{pmatrix}. \tag{2.90}$$

in a Cartesian coordinate system of body frame fixed to the particle. Conversions from the body frame to the general lab frame can be obtained by multiplying by the rotation matrix. If the a_1 axis of particle has polar and azimuthal angles respectively as θ and

ϕ, $\widetilde{\alpha}$ in general lab frame system has the expression as

$$\widetilde{\alpha} = \alpha_b \widetilde{I} + (\alpha_a - \alpha_b)(\vec{u}\vec{u}). \tag{2.91}$$

or

$$\widetilde{\alpha} = \begin{pmatrix} \alpha_b + \sin^2\theta \cos^2\phi\,(\alpha_a - \alpha_b) & \sin^2\theta \sin\phi \cos\phi\,(\alpha_a - \alpha_b) & \sin\theta \cos\theta \cos\phi\,(\alpha_a - \alpha_b) \\ \sin^2\theta \sin\phi \cos\phi\,(\alpha_a - \alpha_b) & \alpha_b + \sin^2\theta \sin^2\phi\,(\alpha_a - \alpha_b) & \sin\theta \cos\theta \sin\phi\,(\alpha_a - \alpha_b) \\ \sin\theta \cos\theta \cos\phi\,(\alpha_a - \alpha_b) & \sin\theta \cos\theta \sin\phi\,(\alpha_a - \alpha_b) & \alpha_b + \cos^2\theta\,(\alpha_a - \alpha_b) \end{pmatrix}, \tag{2.92}$$

where $\vec{u}$ is the unit orientation vector of the particle, which is

$$\vec{u} = \begin{pmatrix} \sin\theta\cos\phi \\ \sin\theta\sin\phi \\ \cos\theta \end{pmatrix}. \tag{2.93}$$

Substituting the polarizability tensor in equation (2.89) with equation (2.91), the real and imaginary parts of $\widetilde{S}(0)$ can be expressed as

$$\mathbf{Re}\{\widetilde{S}(0)\} = \frac{2k^6}{3}\left[\alpha_b^2 \widetilde{I} + (\alpha_a^2 - \alpha_b^2)(\vec{u}\vec{u})\right] \tag{2.94}$$

$$\mathbf{Im}\{\widetilde{S}(0)\} = k^3\left[\alpha_b \widetilde{I} + (\alpha_a - \alpha_b)(\vec{u}\vec{u})\right]. \tag{2.95}$$

For a flow in the $x - y$ plane and the light propagating along z direction, only the upper left subset of the polarizability matrix in equation (2.92) matters in the calculation of $\widetilde{S}(0)$. The linear birefringence $\Delta n'$ and linear dichroism $\Delta n''$ as defined above can be further calculated as ensemble averages over the orientation distribution function and the shape distribution function for prolates

$$\Delta n' = 2\pi n_f N\,(\alpha_a - \alpha_b)\left[< \sin^2\theta \cos(2\phi) >^2 + < \sin^2\theta \sin(2\phi) >^2\right]^{\frac{1}{2}} \tag{2.96}$$

$$\Delta n'' = \frac{2}{3}\pi n_f N k^3\,(\alpha_a^2 - \alpha_b^2)\left[< \sin^2\theta \cos(2\phi) >^2 + < \sin^2\theta \sin(2\phi) >^2\right]^{\frac{1}{2}}, \tag{2.97}$$

where $<>$ is the averaging symbol. Since in most cases the principal polarizabilities are coincident with the principal axes of the particle itself, the average orientation angles of birefringence and dichroism are the same and equal to the net orientation of the particles. And it is the angle of rotation that diagonalizes the upper subset of the

polarization matrix $\widetilde{\alpha}$ and can be expressed as [67]

$$\tan\left(2\chi\right) = \frac{<\sin^2\theta\sin\left(2\phi\right)>}{<\sin^2\theta\cos\left(2\phi\right)>}, \qquad (2.98)$$

where χ is the orientation angle.

The optical method used in our experiments to detect the ensemble-averaged particle orientation in SWNT suspensions is a polarization modulation technique [67,68], which is based on the theory of light scattering by small particles discussed above. A detailed mathematical description of our experimental setup will be provided in Ch. **4**. Starting from the next chapter, we will discuss the details of our two major experiments: the rheology measurement and the ensemble-averaged particle orientation measurement of SWNT suspensions under both shear and electric fields.

Chapter 3

Rheology measurement of SWNTs/α-terpineol suspension under both shear and electric fields

Apparent viscosity measurements of SWNTs/α-terpineol suspension under both shear and electric fields are carried out by two individually modified rheological instruments: a Brookfield DVII+ Pro viscometer and a Bohlin VOR rheometer. The Brookfield DVII+ Pro viscometer, which can be easily modified due to the simplicity of its mechanical setup of the measurement cell, is used to perform both rheological and later optical measurements under various shear rates and electric field strengths. The ER apparent viscosity of SWNTs/α-terpineol suspensions is explored over a range of experimental conditions and the results suggest that Maxwell-Wagner polarization model is applicable in this particular ER fluid, the SWNTs/α-terpineol suspension. To further study the equilibrium time scale and trend of apparent viscosity over a larger range of the combination of shear rates and electric field strength or equivalently the parameter $\dot{\gamma}/E^2$, the Bohlin VOR rheometer was used to conduct systematic rheometry measurements. In the following, we will discuss our experimental results with both the Brookfield viscometer and with the Bohlin VOR rheometer.

3.1 Rheology measurement using Brookfield DVII+ Pro viscometer

3.1.1 Experimental setup

Apparent viscosity measurements of SWNTs/α-terpineol suspensions under external electric field were first performed on the Brookfield DVII+ Pro viscometer with a modified concentric-cylinder geometry cell. The modification makes two additions to the
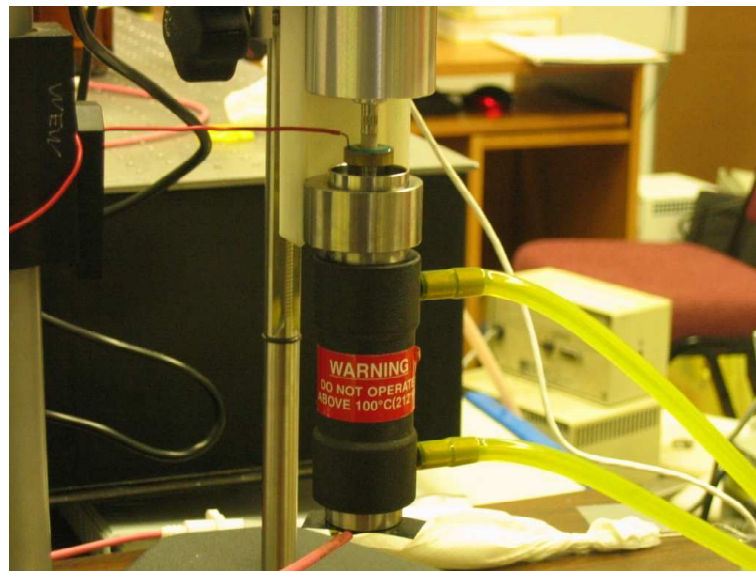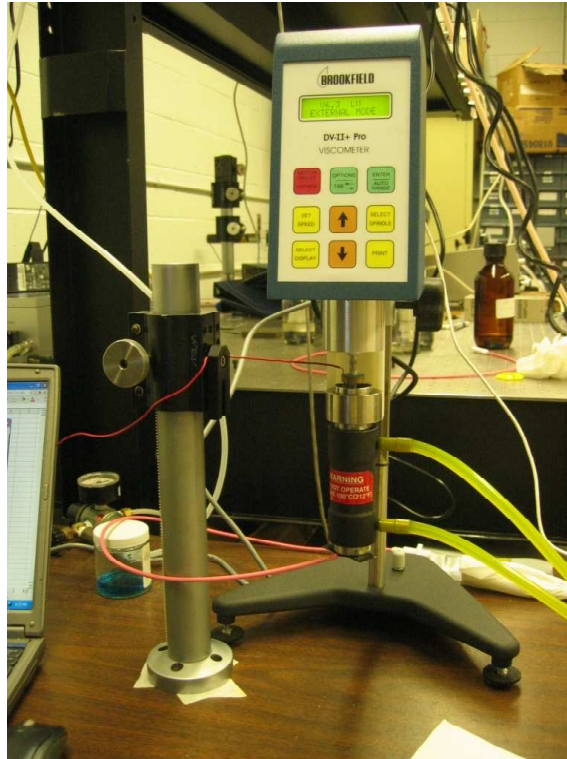
Figure 3.1: Pictures of the experimental setup of electrorheology measurements.

original concentric-cylinder cell. The first addition is a plastic insulator which is inserted between the top measuring unit and the metal coupling nut connecting to the inner cylinder to provide high voltage shock protection to the main electronic unit of the device. The second additional part is a small brass disc with a 0.2" wide and 0.1" deep groove on it which will be used to facilitate a good grounding of the inner cylinder. A conducting wire is dipped into the groove with copper nitrate solutions in it to make an electrical connection from the inner cylinder to the ground. It has to be assured that the wire has no direct contact with the bottom of the groove on the copper disc so that no significant extra torque is applied on the rotating shaft where the rheology measurement data is collected. A radially oriented electric field is developed between the inner cylinder and the outer cylinder by charging the outer cylinder with a high-voltage amplifier (Trek 609E-6) while keeping the rotating inner cylinder grounded. In this arrangement, the electric field applied on the SWNT suspensions tend to orient the nanotubes radially, perpendicular to the flow direction. At the same time the voltage applied on the sample suspension and the current through the sample circuit were monitored by a LabView data acquisition system. A schematic of the experimental setup of rheology measurement with an applied electric field is shown in Fig 3.2. An AC electric field is chosen in order to minimize possible electrochemical effects at the electrodes as well as electrophoretic motion of the nanotubes. Since this model of Brookfield viscometer is strain-controlled instrument, only apparent viscosity rather than yield stress measurement of our ER fluids can be performed. But the simple configuration of this machine does make modifications more practical and easier to be carried out. Modifications for optical measurements on this viscometer will be described in another section.

3.1.2 Sample preparation

Dilute or semi-dilute SWNT suspensions were prepared by dispersing HiPCO SWNTs (Carbon Nanotechnologies, Inc.) in α-terpineol at a volume fraction of $\Phi = 1.5 \times 10^{-5}$. The length distribution of the SWNTs was estimated to range from 150 nm to 3000 nm, with a mean around 1 μm as originally obtained from CNI. Acid-treatment was applied
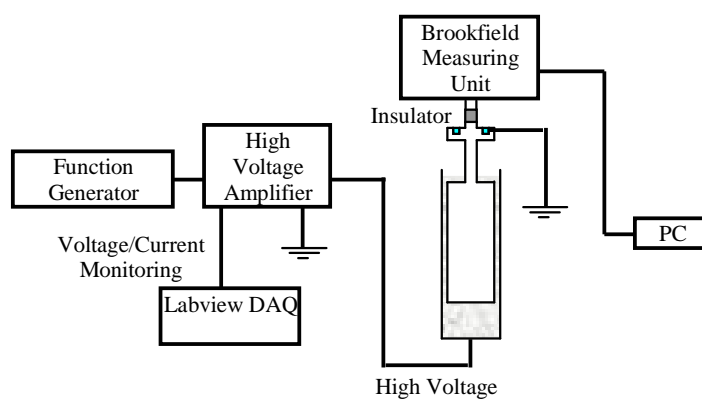
Figure 3.2: Schematic of the modified concentric-cylinder viscometer which measured the apparent viscosity while simultaneously monitoring the applied voltage and current.

by CNI to remove amorphous carbon and left over catalyst particles after the synthesis of these SWNTs. The solvent, α-terpineol, has low electric conductivity and a viscosity about 36.0 cPs at room temperature and was reported to be a good solvent for carbon nanotubes [69]. Samples were prepared at room temperature with the assistance of bath sonication. Bath sonication was chosen rather than tip sonication because it has been shown to effectively disperse nanotubes with significantly less nanotube breakage [17,70]. The suspension was sonicated and rested alternately for a period of 12 hours each for several times. This alternating sonication/rest procedure was used to make certain the particles were sufficiently wetted by the surrounding fluids and minimized the chance of bubble creation. At the prepared volume fraction of $\Phi = 1.5 \times 10^{-5}$, the suspensions were dilute in the sense that the average distance between nanotubes was such that they were unlikely to interact through random rotations. The specific criteria to distinguish dilute from semi-dilute suspensions will be discussed in more detail in the next chapter. The suspensions primarily contained a mixture of individual nanotubes and small bundles of SWNTs, as will also be discussed in more detail in the next chapter. Particle sizing with a disk-centrifuge instrument showed that the bundles were small, with an equivalent hydrodynamic diameter peak below 160 nm.

3.1.3 Experimental results of apparent viscosity of SWNTs/α-terpineol suspension

The experimental setup of the rheometry measurement under external electric field was described in Sec. **3.1.1**. The Brookfield DVII viscometer with modified concentric cylindrical cell developed a shear flow in the circumferential direction while the high AC voltage applied between two cylinders generated a radially oriented electric field as illustrated in Fig. 3.3.

The dependency, if any, of the ER response on the frequency of applied AC fields were first tested to verify that all the experiments conducted were at low-frequency/DC region of Maxwell-Wagner model as described by the equations (2.8 to 2.13), where the conductivities of the particle and liquid phase determine the interfacial polarizability. In an initial set of experiments, it was shown that the apparent viscosities were little

Flow field

a

Electric field

b

Both flow and electric field

c

d
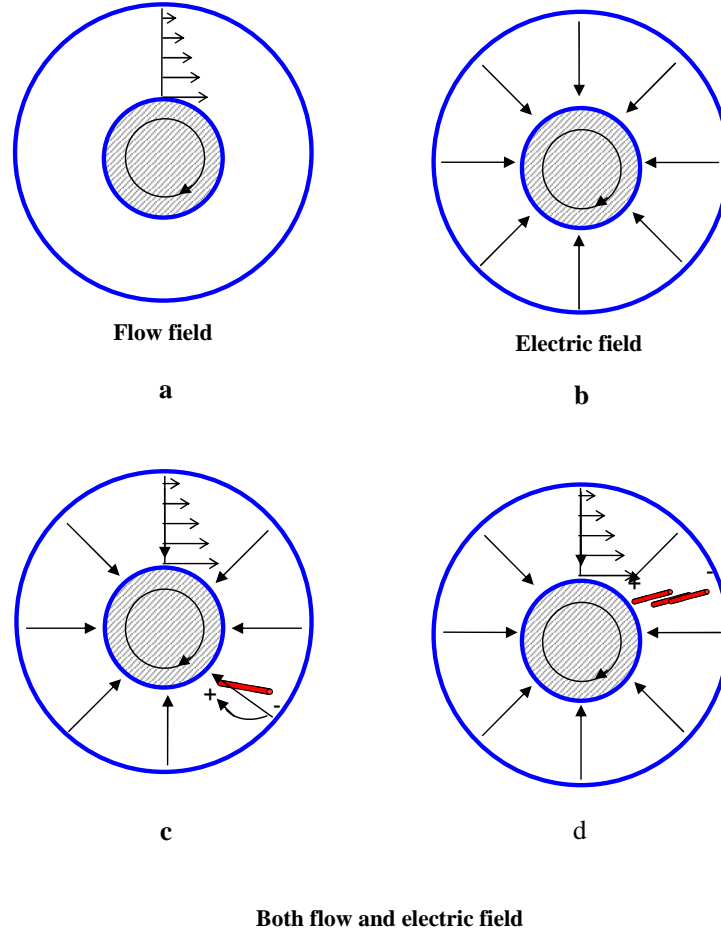
Figure 3.3: **a.** Top view of the shear flow field with streamline along the circumferencial direction. **b.** Top view of the applied electric field in radial direction. **c.** A particle in both flow and electric field: competing hydrodynamic and electrostatic torque (including torque applied by the field and the torque due to dipole-dipole interaction) trying to rotate the particle. **d.** Particles reach equilibrium under both fields and start chaining due to dipole-dipole interaction.

affected by the frequency of the applied field over a tested range of 100 Hz to 10 kHz, as was expected. For all subsequent measurements, a fixed 4 kHz field is applied based on this insensitivity to field frequency under 10 kHz.

Reproducibility of these rheology measurements was tested by measuring selected samples for several times and measuring different sample loadings in different days. Fig. 3.4 shows results of reproducibility tests in several typical cases. These results further confirmed the necessity of alternately sonicating and resting the samples for many times. Assurance of at least one hour of re-sonication before any rheology measurements were also critical to good reproducibility of our experiments.

Representative time-traces of the measured apparent viscosity, η, normalized by the liquid continuous-phase viscosity, η_c, are shown in Fig. 3.5 for a constant shear rate of $\dot{\gamma} = 6.12 \, \text{s}^{-1}$. At these extremely low volume fractions, the continuous phase viscosity η_c is equivalent to the suspension viscosity in the absence of an electric field. Electric fields of the indicated root-mean-square (RMS) strengths were turned on at $t = 160 \, \text{s}$. A clear ER response is seen, with the apparent viscosity more than doubling at $E_{\text{rms}} = 213$ V/mm. In contrast to conventional ER fluids, which typically have response times ranging from a few milliseconds to several seconds [32, 72], these SWNT/α-terpineol suspensions required hundreds of seconds to reach equilibrium. This is likely due to the low concentrations, which are $4 - 5$ orders of magnitude lower than typical ER fluids. Another unusual characteristic of the dilute SWNT suspensions is the saturation that is seen in the steady-state apparent viscosity at higher electric fields. Beyond a certain field strength of around 160 V/mm (but below another critical threshold), increasing the electric field only serves to decrease the response time of the ER suspension. Thus, at the fields strengths of $E_{\text{rms}} = 160$ and 213 V/mm, the final values of η are nearly identical. At very high electric fields where percolation happens, the apparent viscosity can spike suddenly due to the growth of SWNT chains that span the entire gap between inner and outer cylinders of the viscometer. The simultaneous current monitoring result shown in Fig. 3.6 gave significant evidence that percolation happened in the sample suspension. One or more SWNT chains bridged the whole gap between the cylinders, which initiated a large electrical current flow through the sample. At that moment, the
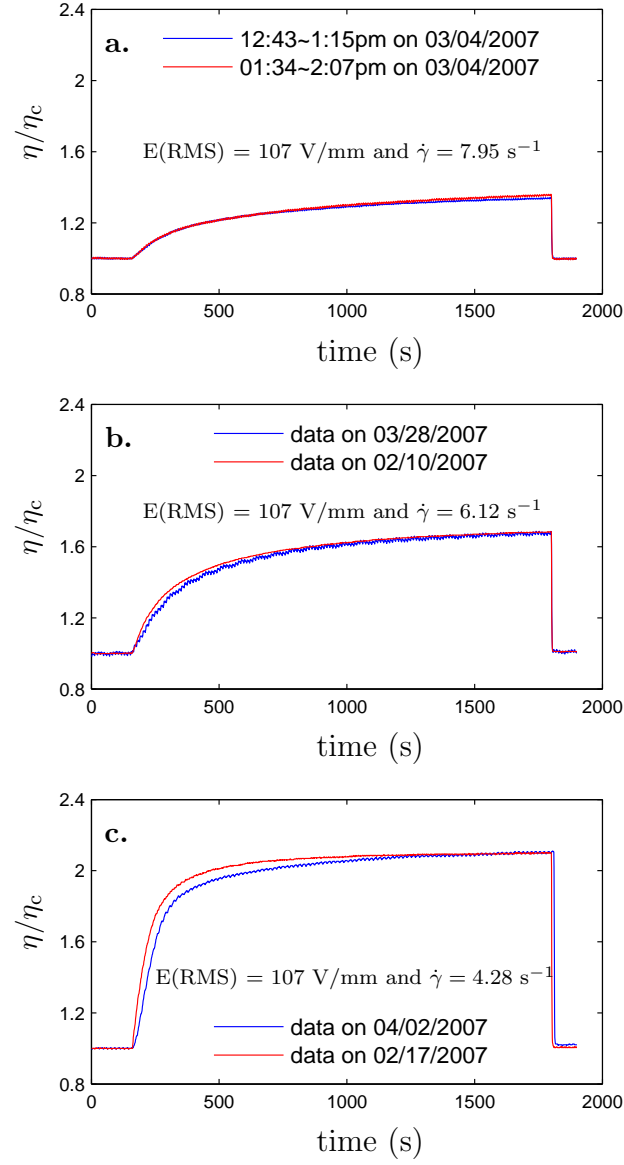
Figure 3.4: **a.** Two measurement data sets taken for the same sample. **b.** and **c.** Data sets taken from measurements of different sample loading made in different dates.

measurement system had to be shut down in order to protect the AC amplifier which could only handle maximum peak to peak current value of 20 mA.

Measured steady-state apparent viscosities for non-percolating suspensions are shown in Fig. 3.7 and 3.8 for varying field strengths and shear rates. The steady state viscosities, *i.e*, those after long equilibration times after the field is applied, are estimated by fitting the time-trace data to an exponential of the form $\eta = \eta_0 + a_0 \exp(-(t - t_0)/\tau)$. The steady-state η_0 are also plotted against the ratio of shear rate and electric field squared, $\dot{\gamma}/E^2$, and an equivalent dimensionless parameter, the Mason number. Two regimes can be easily noticed in Fig. 3.9: (1) the data for varying shear rates and electric fields collapse well for large values of $\dot{\gamma}/E^2$ (2) At lower values of $\dot{\gamma}/E^2$, the apparent viscosity saturates with increasing electric field, and the data for different shear rates begin to deviate from one another after saturations are reached.

3.1.4 Analysis and discussion

To interpret these results, we consider the electrostatic particle-particle interaction forces acting on the nanotubes in suspension. We already discussed the particle-particle interaction forces in Sec. **2.1.3** and here we are going to do the calculation a little differently starting from the interaction potential of two particles in an electric field. In the simplest point-dipole approximation, the interaction potential between two particles suspended in a liquid of dielectric constant k_f is:

$$W = \frac{4\pi\epsilon_0 k_f \alpha_0^2 E^2}{r^3} \left(3\cos^2\theta - 1\right), \tag{3.1}$$

where α_0 is the effective polarizability of the particle in vacuum, r is the distance between the two particles, and θ is the angle between the field and a line connecting the particles. The force between the two particles is $F_{\mathrm{dipole}} = -\partial W/\partial r$, which, for $\theta = 0$, has a maximum value of

$$F_{\mathrm{dipole,max}} = \frac{24\pi\epsilon_0 k_f \alpha_0^2 E^2}{r^4}. \tag{3.2}$$

This is consistent with Eq. (2.44). The effective polarizability α_0 can be calculated from the Maxwell-Wagner interfacial polarization model (Eqns 2.8 to 2.13) as previously
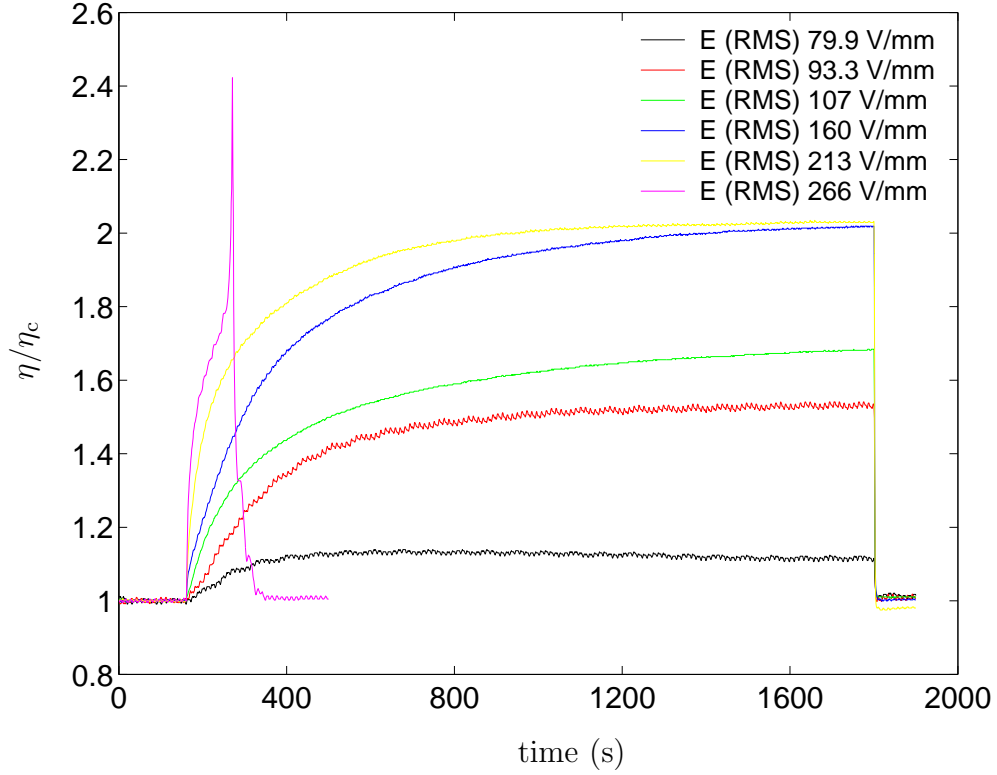
Figure 3.5: Time traces of the normalized apparent viscosity of the suspension. For the data shown, the shear rate was maintained constant at $\dot{\gamma} = 6.12 \text{ s}^{-1}$, while the applied electric-field strength was varied. For the $E_{\text{rms}} = 266$ V/mm case, the field is turned off at $t = 300$ s, when field-induced percolation occurs.
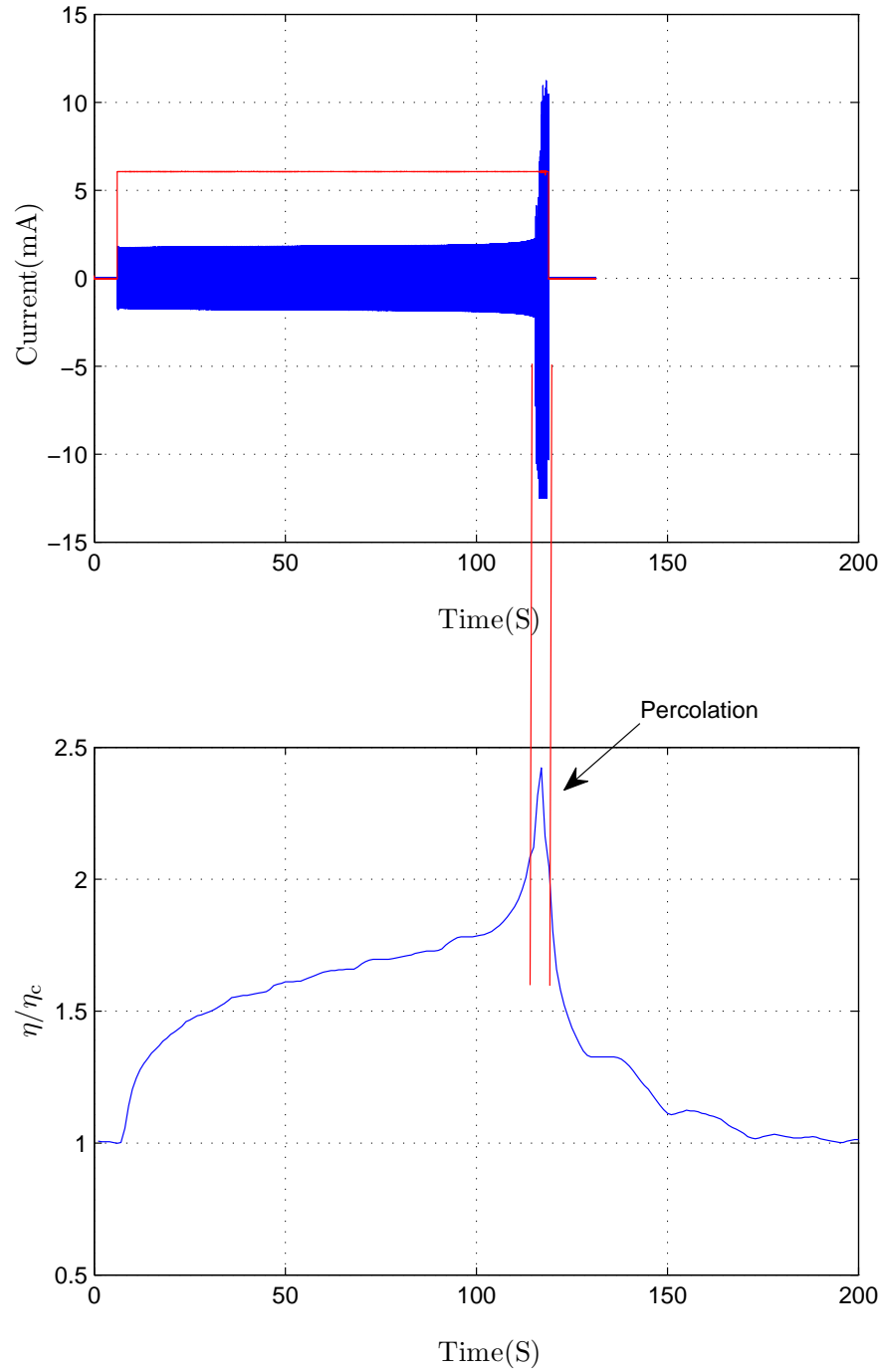
Figure 3.6: Current monitoring as in the $E_{\mathrm{rms}} = 266$ V/mm case in Fig. 3.5. When field-induced percolation occurs, both the apparent viscosity and the current through the sample spike concurrently, which indicates that there is one or more SWNT chains span the enrire gap (sample becomes conductive at that moment) between the two cylinders.
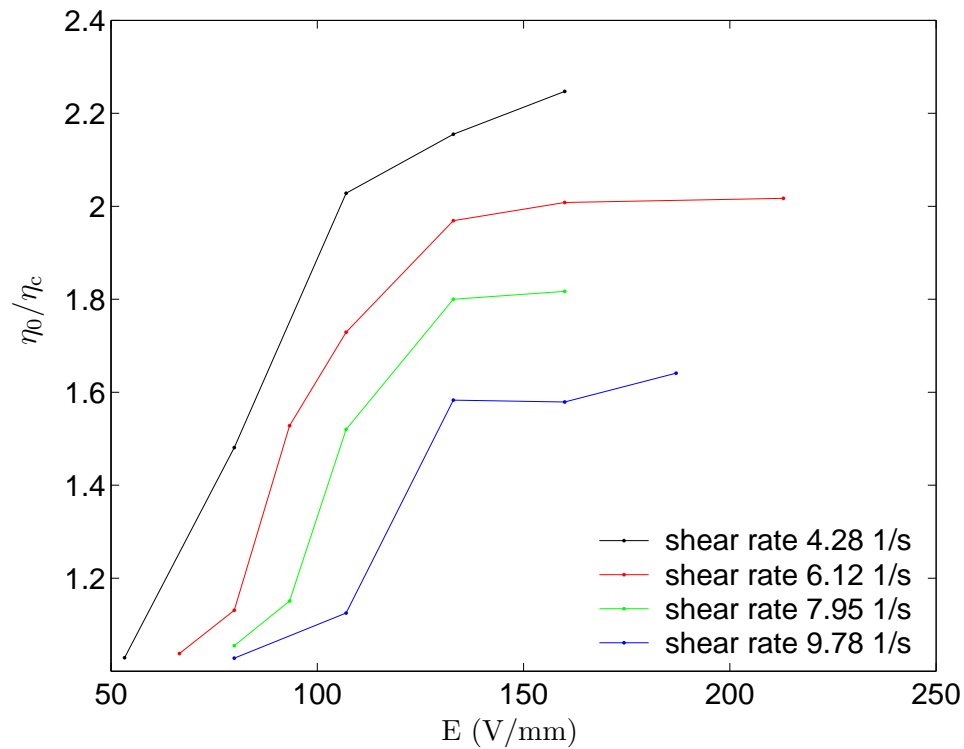
Figure 3.7: Steady-state apparent viscosity varies with electric field strength.
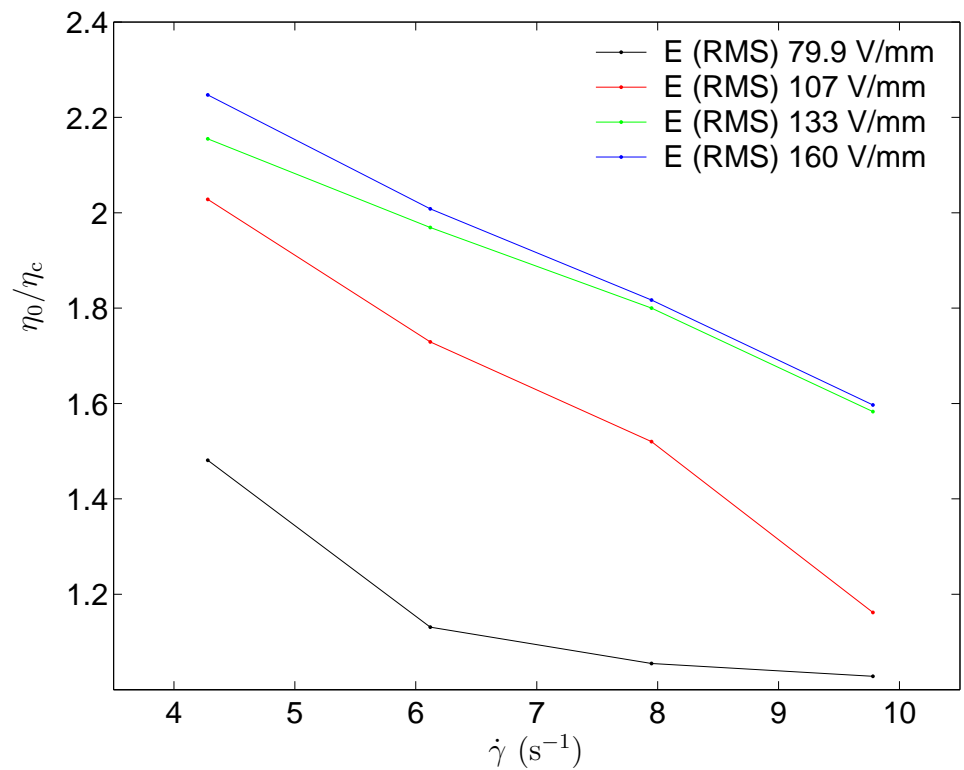
Figure 3.8: Steady-state apparent viscosity varies with shear rate.
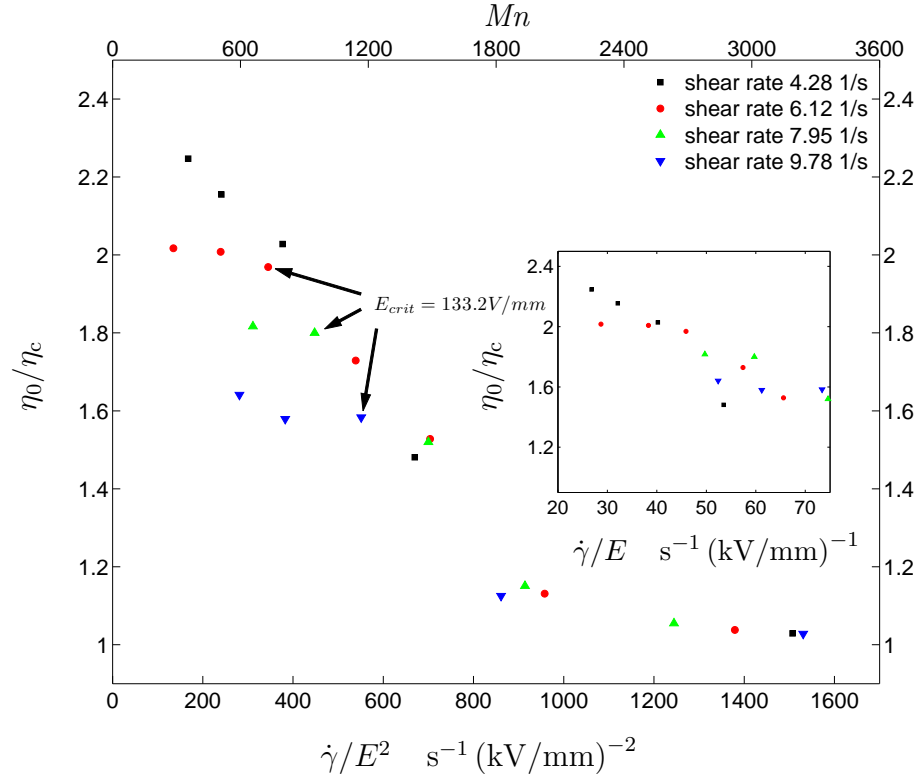
Figure 3.9: Steady-state apparent viscosity of the SWNT/α-terpineol suspension as a function of $\dot{\gamma}/E^2$ or, in dimensionless form, Mn. The inset shows the low-Mn, number data replotted against $\dot{\gamma}/E$.

Table 3.1: Typical values of the dimensionless ratios of competing forces/energies in the SWNT/α-terpineol suspension at room temperature under electric fields of magnitude $100 - 300$ V/mm. The viscosity and dielectric constant of α-terpineol is 37.6 cP and 2.8 respectively. The shear rate is taken to be $\dot{\gamma} = 5$ s^{-1} and the nanotube length is estimated to be $l = 1.0$ μm. The dipole-interaction strength is estimated based on a separation distance of $r = 1.0$ μm and a polarizability of $\alpha_0 = 0.011$ μm^3 derived from our previous experiments on SWNT alignment under electric fields.

Dimensionless parameter	Interpretation	Typical value
$Mn \equiv \frac{\eta_c \dot{\gamma} l^6}{8\epsilon_0 k_f \alpha_0^2 E^2}$	$\frac{\text{Viscous}}{\text{Dipole}-\text{dipole}}$	$80 - 800$
$\lambda \equiv \frac{4\pi\epsilon_0 k_f \alpha_0^2 E^2}{l^3 k_B T}$	$\frac{\text{Dipole}-\text{dipole}}{\text{Thermal}}$	$0.1 - 0.8$
$Pe \equiv \frac{3\pi\eta_c l^3 \dot{\gamma}}{k_B T}$	$\frac{\text{Viscous}}{\text{Thermal}}$	400

[58, 61] mentioned if the complex dielectric constants of the particle and liquid are known. The polarizability of a SWNT along the main tube axis can be estimated by

$$\alpha_\parallel = \underline{K}_\parallel \pi \frac{d^2}{4} l. \tag{3.3}$$

where d is diameter and l is the length of a nanotube. $\underline{K}_\parallel$ is defined in Eq. (2.27). The conductivities dominate the polarizability in the low-frequency limit, while the (real) dielectric constants are most important to the polarizability in the high-frequency limit. However, in practive, rather than estimate the polarizability based on the conductivities of the nanotubes and fluid, it is more convenient to use α_0 from earlier experiments measuring the alignment of identical SWNTs in suspension under electric fields [54]. Based on this measured α_0, the particle-interaction force can be estimated for nanotubes near contact by assuming $r = l$, where the length of the nanotube is taken to be $l = 1.0$ μm. We note that the assumption of point dipoles makes this an underestimate of the actual electrostatic force between nanotubes in close proximity.

Typical values of the dimensionless ratios of the viscous shear, thermal, and dipole-dipole interaction forces for our experiment are summarized in Table 3.1. (Van der Waals forces are neglected because they are much shorter range than the electrostatic dipole-dipole force [73].) The Mason number, Mn, is the ratio of viscous forces to dipole-dipole forces, while the Peclet number, Pe, gives the ratio of viscous energy

to thermal energy, and the interaction parameter, λ, parameterizes the ratio of dipole-dipole interaction energy to thermal energy. The Pe, value indicates that this SWNT/α-terpineol suspension is non-Brownian. The dipole-dipole interaction energies/forces seen in the table are within one or two orders of magnitude of the thermal energy and viscous force, respectively. As noted before, however, the point-dipole assumption underestimates the dipole-dipole interaction when particles are close to each other. Moreover, unlike the conventional Mn, for spherical particles, which does not depend on the size of the particles, the Mn, in our case depends on the sixth power of the length scale, l, which is chosen for the SWNTs. Thus, the actual values of the Mn, and λ in our experiments are likely to be lower and higher, respectively, than estimated. Since our experiments were conducted at a fixed temperature, we expect that Mn, $i.e$, the ratio of viscous to electrostatic particle-particle interaction force, suffices to characterize the ER behavior of the SWNT suspension. This is supported by Fig. 3.9, which shows that the data for apparent viscosity collapses for varying shear rate and electric field when plotted against Mn, or $\dot{\gamma}/E^2$, at least for large Mn. At high electric fields, however, the fluid conductivity can increase with field strength, thus causing the electric field between two closely spaced particles to be lower than it would be if the fluid conductivity had not increased. The dipole-dipole interaction force in this case has been found to depend linearly [74] rather than quadratically on E. Thus, the collapse of the apparent viscosity in Fig. 3.9 when plotted against $\dot{\gamma}/E$, rather than against $\dot{\gamma}/E^2$, at low Mn may be a consequence of such a field-enhanced conductivity effect. We further determined a critical electric field strength, E_{crit}, where the linear dependence of dipole-dipole interaction on E started to take place. As illustrated in Fig. 3.9, we obtained $E_{crit} = 133.2\mathrm{V_{rms}}/\mathrm{mm}$ from where the data points at different shear rates began to plateau. We suggest, therefore, that the ER behavior of the SWNT/α-terpineol suspension can be interpreted in terms of a electrostatic polarization model, where the governing parameter is the ratio of viscous to dipole-dipole forces. Only the dependence of the dipole-dipole forces on E appears to change in the high- and low-field limits.

The magnitude of the ER response for the SWNT suspension is surprisingly large

in comparison to conventional ER suspensions of the same volume fraction. To illustrate this, we compare the SWNT suspensions to suspensions of spherical glassy carbon particles (diameter of 0.4 μm) in the same solvent, α-terpineol. As Fig. 3.10 shows, no discernible electrorheological response is seen for a particle volume fraction identical to that of the SWNT suspension, despite the fact that the glassy-carbon particles are conducting and polarizable at low frequencies like the nanotubes. In fact, the glassy-carbon suspension require a volume fraction three-orders-of-magnitude higher than that of the SWNT suspension to achieve similar increases in apparent viscosity, under the same conditions ($E_{\mathrm{rms}} = 160$ V/mm, shear rate of 6.12 s^{-1}). This is consistent with the reports of enhanced ER response for $r_e = 30$ whiskers (as compared to spherical particles) of aluminum-borate at volume fractions of 3.4×10^{-3} to 0.125 [75, 76]. However, the enhancement is much more pronounced for these dilute suspensions of SWNTs.

To explain the remarkably large ER response of the dilute SWNT suspension, we compare the electrostatic and viscous forces acting on SWNTs to those of spherical particles. Since the SWNTs have an aspect ratio of order 10^3, they have simultaneously higher polarizabilities and viscous drag forces as compared to spherical particles of the same volume. The polarizability of a conducting prolate spheroid of length l and aspect ratio r_e immersed in a fluid of dielectric constant k_f is, in the limit of $r_e \gg 1$, [77]

$$\alpha = \frac{k_f l^3}{24 \left[\log \left(2 r_e\right) - 1\right]}, \tag{3.4}$$

while the polarizability of a conducting sphere is $\alpha = k_f a^3$, where a is the radius of the sphere. Assuming typical dimensions of $l = 1.0$ μm and $r_e = 1000$, the nanotube has a polarizability comparable to a spherical particle of radius $a = 0.18$ μm. Such a spherical particle would have a volume 3×10^4 times larger than that of the SWNT. Similarly, the viscous drag force for a nanotube moving at relative speed v perpendicular to its long axis in a fluid of viscosity η_{c} is [78]

$$F_{\mathrm{D}} = \frac{4\pi \eta_{\mathrm{c}} l}{\log r_e} v, \tag{3.5}$$

while that of a sphere is $F = 6\pi \eta_{\mathrm{c}} a v$. (The drag force only differs by a factor of one-half if the nanotube moves parallel to its long axis.) Thus, for flow at the same speeds, the
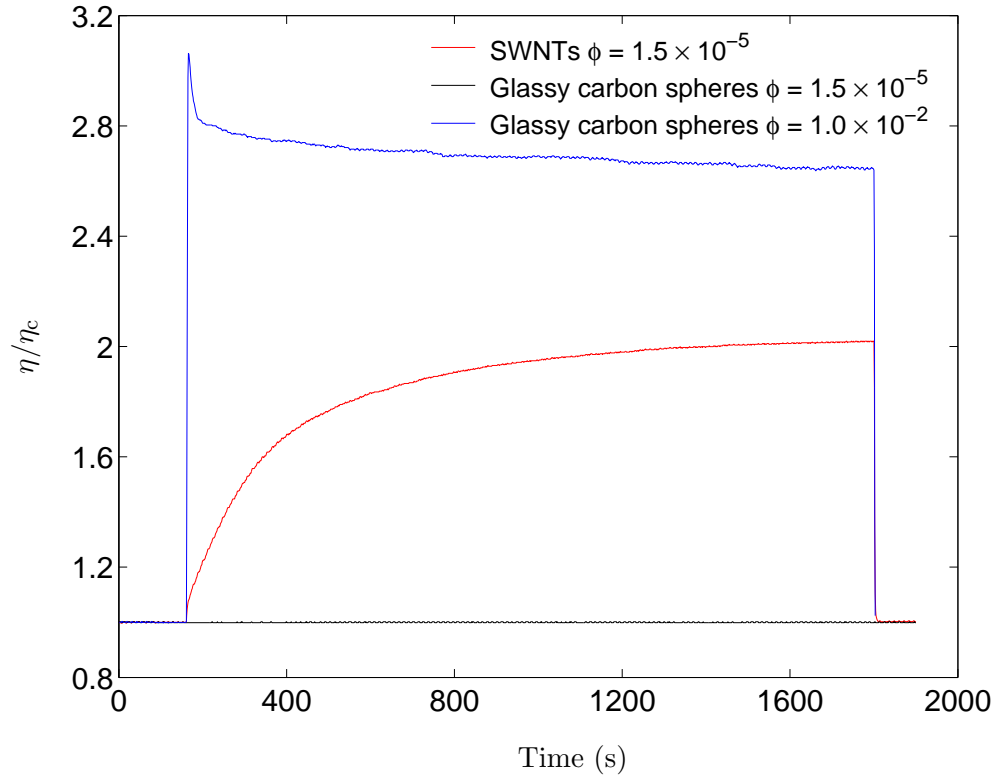
Figure 3.10: Comparison of the electrorheological response between a SWNT suspension and suspensions of spherical conductors (glassy carbon spheres). The SWNT suspension shows an electrorheological response that is comparable to a glassy-carbon suspension having three-orders-of-magnitude-higher volume fraction. No measurable response is seen for the glassy-carbon suspension of the same volume fraction.

viscous force on the SWNT is equivalent to that a sphere of radius $a = 0.10$ μm, or volume 4×10^3 times larger than that of the SWNT. This larger viscous force can lead to a greater energy dissipation in the flow, and possiblly a higher apparent viscosity. But based on another experimental observation (the orders of difference in time scales of particle orientation and the ER response) that will be discussed later in Sec. **4.5**, the higher viscous drag is likely not the cause of the enormous ER effect. In summary, the large aspect ratio of the nanotubes, which results in higher polarizabilities and thus particle chaining, is thus believed to be responsible for the unusually large ER response of the SWNT suspension at low volume fractions.

3.2   Rheology measurement using Bohlin VOR rheometer

3.2.1   Experimental setup

The adaptation of the Bohlin VOR rheometer to conduct rheology measurements of SWNT suspensions under electric field was similar to that of the Brookfield viscometer we used earlier. To insulate the cylinder cell from the torque measurement unit to avoid possible high voltage shock to the main electronic system, a non-conducting polycarbonate piece was inserted in between. Unlike the Brookfield viscometer the inner cylinder of this VOR rheometer does not rotate when the measurements are performed. The copper disc with a groove in the Brookfield case were replaced by two semispherical pieces of brass with a small indentation to accommodate conducting electrolyte solutions. An acrylic coat for the outer cylinder was necessary to isolate the outer cylinder from the rotating shaft and the temperature control chamber so that the high AC voltage could be applied upon it. The high voltage was applied through a connection between a wired carbon brush and the groove surface of the rotating outer cylinder. The effects on the rotation rate of the outer cylinder due to the friction between the tip of the carbon brush and the groove surface could be safely neglected here. This Bohlin VOR rheometer is a strain-controlled machine, and it is a more dedicated rheology measurement instrument with higher torque measurement range compared to the Brookfield viscometer. Systematic measurements with large range of

shear rates and electric field strength on the electrorheology of SWNT suspensions were made possible by this modified Bohlin VOR rheometer.

3.2.2 Experimental results of apparent viscosity measurements of SWNTs/α-terpineol suspension

The measured steady-state apparent viscosities of SWNT/α-terpineol suspensions using Bohlin VOR rheometer against the electric field strength at various shear rates are plotted in Fig. 3.11, together with the data measured previously by our Brookfield viscometer.

Higher electric field strength were applied when the Bohlin VOR rheometer was used to measure the apparent viscosity. The data follows the same trend as those obtained previously but with lower apparent viscosity. This can be seen more clearly when we plot these data against the parameter $\dot{\gamma}/E^2$ in Fig. 3.12. Similar phenomena happened as in Fig. 3.9: at high value of $\dot{\gamma}/E^2$, all data collapse pretty well, but at low value of $\dot{\gamma}/E^2$ the apparent viscosity saturates and level out at different saturation values. With these data from Bohlin VOR rheometer, we further verify that our results are consistent on these two independent rheometry setups. Testings of wider range of electric field strength and shear rates were also achieved this time through the adapted Bohlin rheometer.

3.2.3 Summary

In summary of this chapter, we have found, for the first time, evidence for an electrorheological effect in a dilute suspension of carbon nanotubes. The ER behavior of the SWNT/α-terpineol suspension can be interpreted in terms of an electrostatic polarization model, where the governing parameter is the ratio of viscous to dipole-dipole forces. At low field strengths, the conventional Mn, characterizes the viscosity, while, at high field strengths, a modified Mn, which accounts for the nonlinear conductivity of the solvent, best collapses the data. At the highest field strengths, one or more percolating chains of SWNTs can eventually span the electrodes of the viscometer, and cause a further increase in the apparent viscosity. Most notably, the ER response is
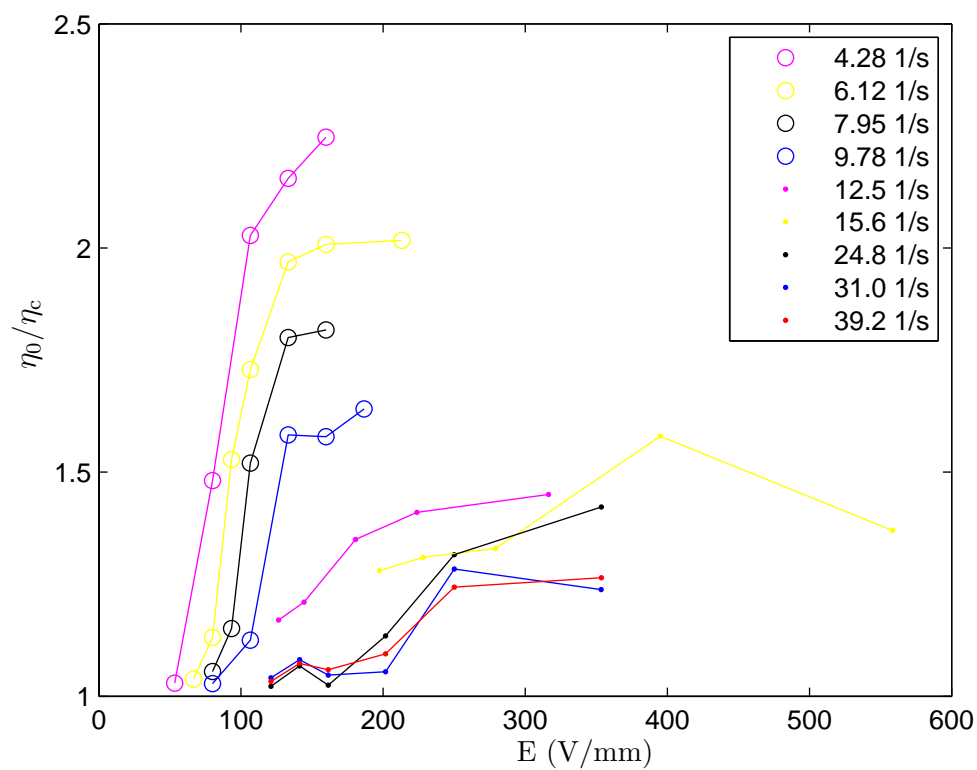
Figure 3.11: Steady-state apparent viscosity varies with electric field strength. Solid dots are data from Bohlin VOR rheometer; Circles are data from Brookfield viscometer.
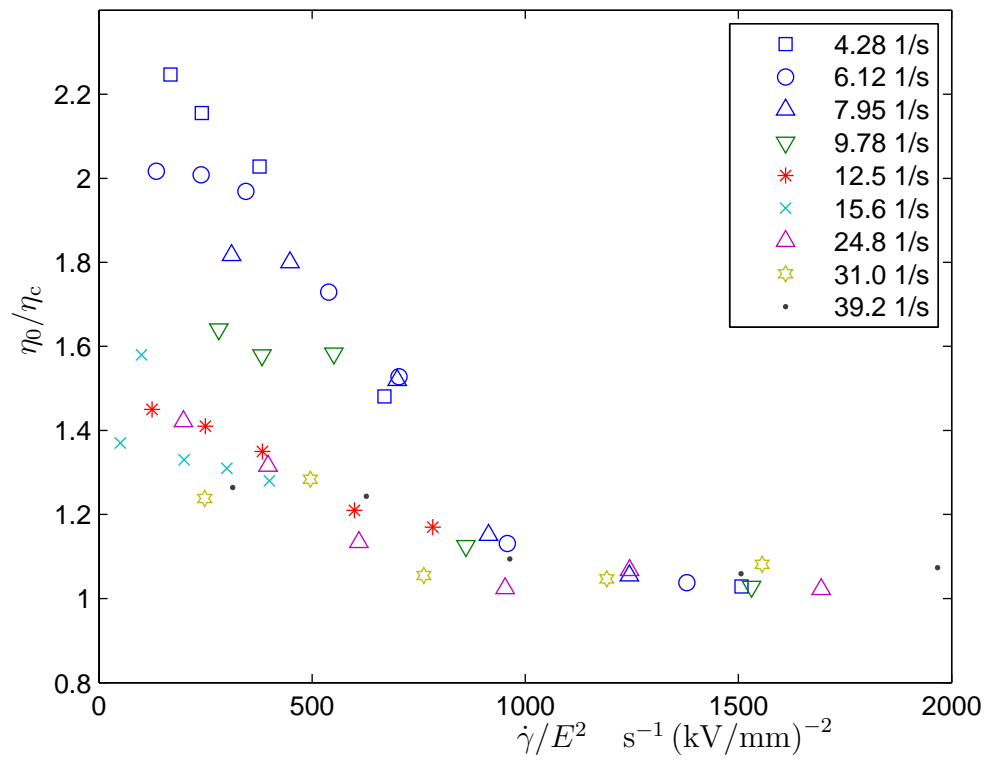
Figure 3.12: Steady-state apparent viscosity of the SWNT/α-terpineol suspension as a function of $\dot{\gamma}/E^2$.

"strong" in the sense that the dilute SWNT suspension displays changes in the apparent viscosity that are comparable to a more conventional (spherical particle) suspension having a 3-orders-of-magnitude-higher volume fraction. The magnitude of the response is believed to be due to the large aspect ratio of the nanotubes, which enhances the electrostatic forces. There are still many questions left to be answered. For instance, since we attribute the unconventionally strong ER response (apparent viscosity) to the highly anisotropic properties (geometry, polarizability) of SWNTs, how would the preferential orientations of SWNTs and small SWNT bundles affect the overall apparent viscosity? We will try to answer this question in the following chapter on the particle dynamics and ensemble-averaged particle orientation of SWNT suspensions under both shear and electric fields.

Chapter 4

Particle dynamics of SWNTs suspensions

4.1 Visualization of structure forming under electric field

To experimentally investigate the microstructure that forms under both shear and electric field, visualizations of the SWNT suspensions were first done in a quiescent fluid under an external electric field.

The chaining of SWNT bundles and the thickening of these chains under an electric field were visualized by Nikon 35 mm camera with a macro lens, as well as a digital image acquisition system which consisted of a one million pixel CCD Redlake camera, an EPIX image acquisition board and software. Two SWNT suspensions were used in the visualization: a volume fraction of 0.001% of SWNTs in pure ethanol and a 0.0015% of SWNTs in α-terpineol. Suspension samples were housed in a glass cuvette (L: 10mm $\times$ W: 10mm $\times$ H: 43mm) with external electrodes attached to its two outside surface normal to the direction of the camera view. A regular desk lamp was used as a background illumination source. Sample images of structure forming process in quiescent flows of ethanol and α-terpineol are shown in Fig. 4.1 and 4.2 respectively. The process of chaining, thickening of chains of SWNT bundles with the electric field on and the snapping of chains after the field being turned off looked similar in both ethanol and α-terpineol cases. But the time scale for these chains to form and getting thicker were quite different. It took about $5-6$ minutes for the camera to start capturing traces of SWNTs chains in SWNTs/α-terpineol suspension and only took $1-2$ minutes in SWNTs/ethanol case. The slight difference in particle volume fraction between the SWNTs/α-terpineol and SWNTs/ethanol suspensions is not likely to cause this difference in the time scale of the chaining process. Instead, it is believed that the SWNT chains formation, thickening, and breaking process were faster
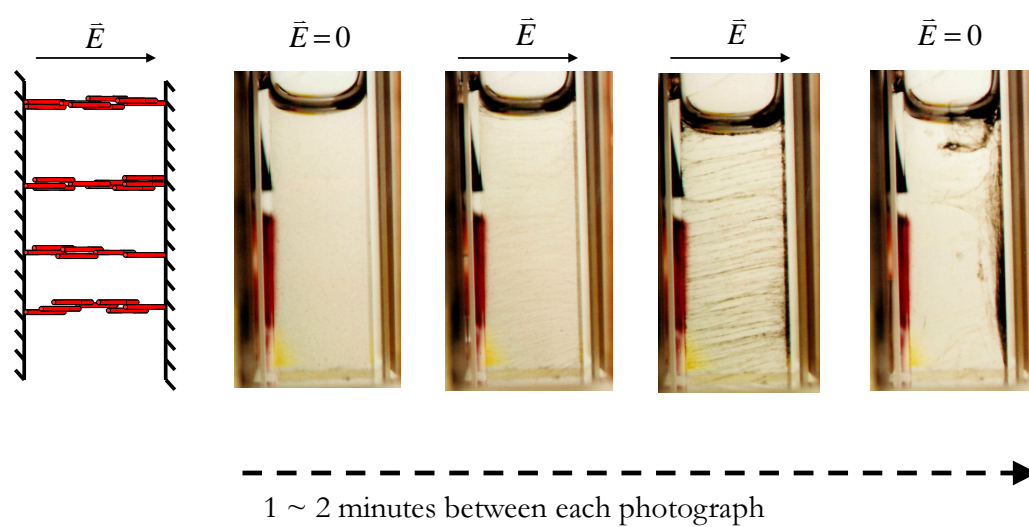
Figure 4.1: Visualization of the SWNTs chain formation under an electric field in a quiescent SWNTs/ethanol suspension.
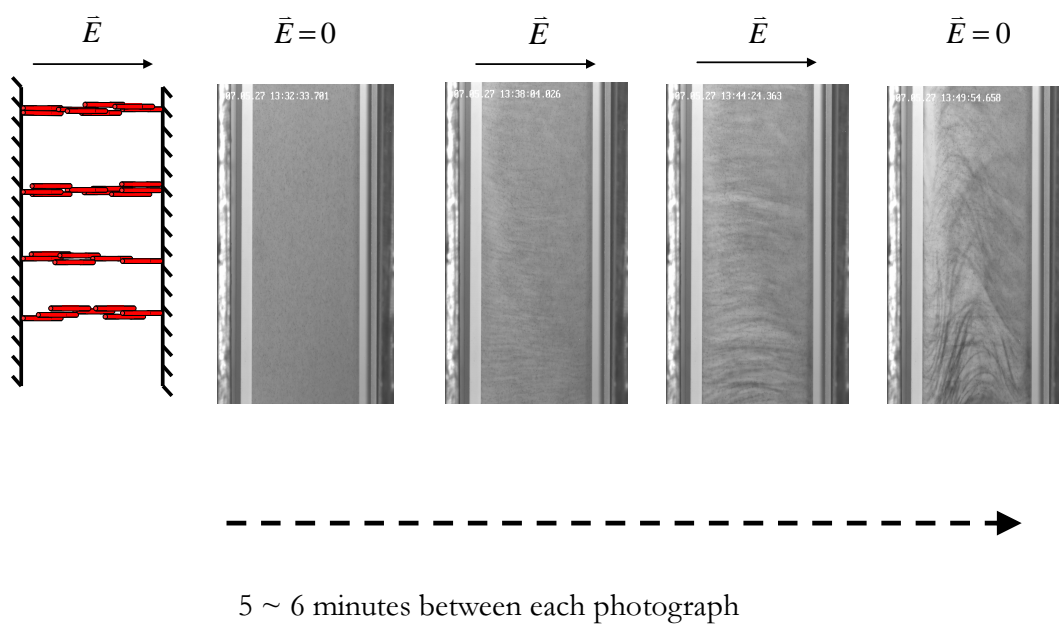
Figure 4.2: Visualization of the SWNTs chain formation under an electric field in a quiescent SWNTs/α-terpineol suspension.
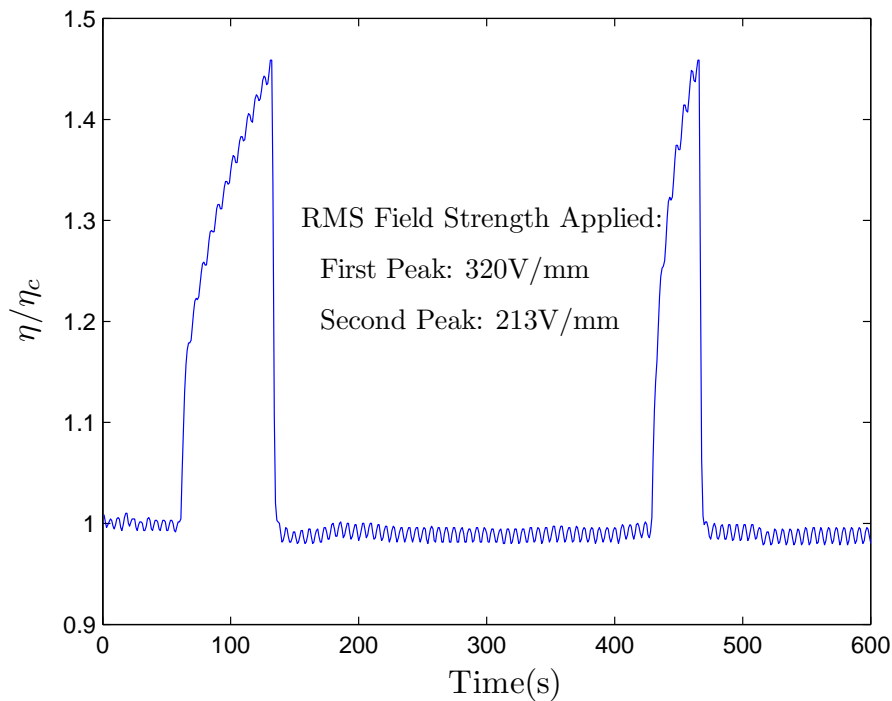
Figure 4.3: Time trace of viscosity ratio at the shear rate of 12.23 1/s. Sample prepared at 20mg/L of SWNT in α-terpineol. External electric field was turned on, off, on and off during the experiment. Time response for the second viscosity jump shortened because of the residual of the chains after the first turn-on and off of the electric field.

in SWNTs/ethanol suspension than that in the SWNTs/α-terpineol case because of the difference in viscosities of the solvents, with ethanol having a viscosity almost 30 times less than that of α-terpineol.

Besides the visualization experiments where the chaining process can be seen directly, we also have other evidence showing the chains forming in the SWNT suspensions. As depicted in Fig. 4.3, during a typical apperant viscosity measurement the external electric field was turned on and off two times to see what was the effect of the chains forming at the first time on the second chaining process. Even though the electric field applied for the second viscosity jump was smaller than that of the first jump, the time response from the second was faster than the first spike which indicated that the chains formed during the first process did not break completely which facilitated the faster chaining in the second process. As will be seen in later sections, chaining and the micro-structure forming in the suspension are the dominant mechanisms for the

dramatic apparent viscosity changes at dilute SWNT suspensions while the aligment of SWNTs in the suspension may only have indirect impact on the viscosity.

4.2   A few notes on particle motion under shear and electric fields

It has been shown in Ch. **2** that a particle under both shear and electric fields will rotate and reach an equilibrium state when the applied electric field strength is greater than a critical value [63]. The particle orientation angles at the equilibrium state have the form of Eqn. (2.76) and (2.77) which are recapped here as

$$\theta_{1\infty} = \frac{\pi}{2} \tag{4.1}$$

$$\phi_{1\infty} = \tan^{-1}\{r_e[f - (f^2 - 1)^{\frac{1}{2}}]\}, \tag{4.2}$$

The complete form of the dimensionless parameter f is

$$f = \frac{-\epsilon_f P\left(\underline{\epsilon}_p/\underline{\epsilon}_f, r_e\right) E_0^2 \left(r_e^2 + 1\right)}{\dot{\gamma}\eta_c r_e}. \tag{4.3}$$

where $P\left(\underline{\epsilon}_p/\underline{\epsilon}_f, r_e\right)$ reflects the induced polarization of the particle and is a function of the particle aspect ratio r_e and the complex permittivity ratio of the particle and the ambient fluid. For conducting particles immersed in a dielectric fluid at low frequency regime (conductivity dominates), as in the case of SWNTs in $\alpha-$terpineol of our experiments, a limiting case of $\sigma_p/\sigma_f \to \infty$ has been taken in the expression for P given in Eq. (2.69).

The parameter f, which is proportional to $E^2/\dot{\gamma}$ under a certain physical conditions in which the physical properties of the particle and its ambient fluid are fixed, is a dimensionless measure of the relative electrostatic-to-hydrodynamic torques acting on the isolated particle in a fixed orientation. This can also be conveniently re-exammed by calculating the ratio of the first component of the electrostatic and hydrodynamic torque applied on the particle by the shear and electric field respectively.

In an x_1', x_2', x_3' coordinate system fixed on an ellipsoidal particle with each axis aligned with the principal axes of the ellipsoid as shown in Fig. 4.4, the x_1'-component of the hydrodynamic torque applied by a flow on an ellipsoidal particle of semi-axes a_1,
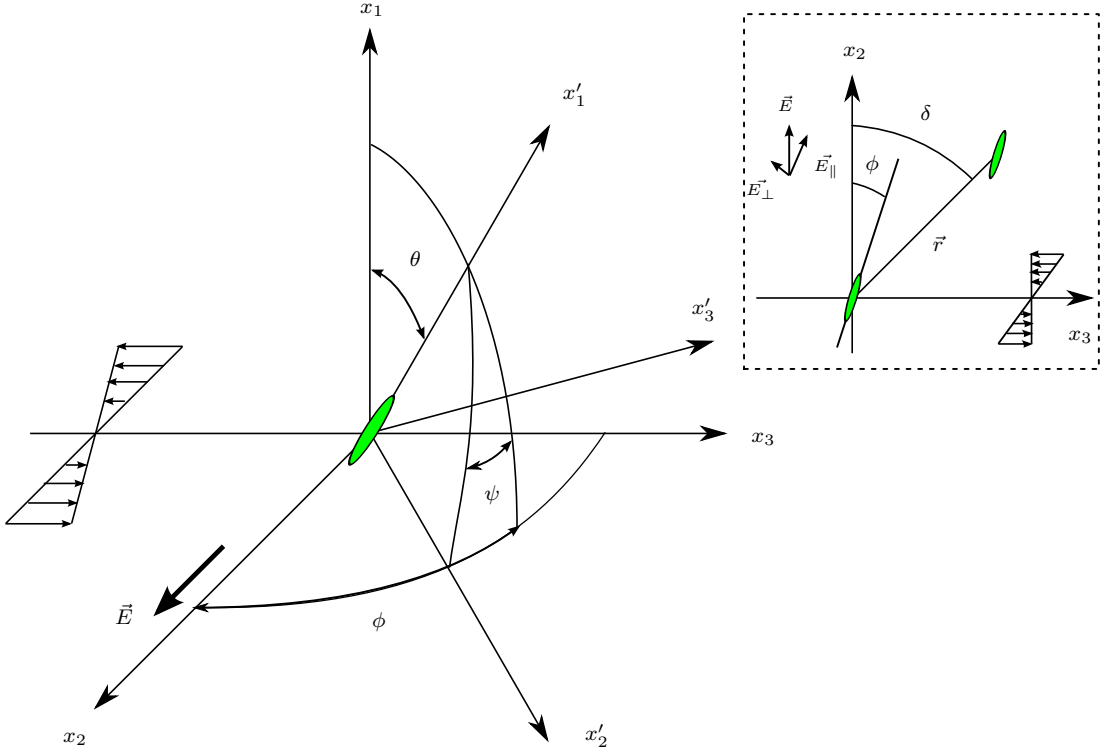
Figure 4.4: Coordinate system used in the calculation of the torque due to the shear flow and electric fields. The inset shows the particle pair configuration of the simplest case considered in this work.

a_2, a_3, is [45]

$$T_{x_1'}^h = \frac{16\pi\eta_c}{3\left(a_2^2\beta_0 + a_3^2\gamma_0\right)}\{\left(a_2^2 - a_3^2\right)h + \left(a_2^2 + a_3^2\right)(\xi - \omega_1)\}, \tag{4.4}$$

where

$$\beta_0 = \int_0^\infty \frac{ds}{\left(a_2^2 + s\right)R_s},$$

$$\gamma_0 = \int_0^\infty \frac{ds}{\left(a_3^2 + s\right)R_s},$$

$$R_s = \sqrt{\left(a_1^2 + s\right)\left(a_2^2 + s\right)\left(a_3^2 + s\right)},$$

$$h = \frac{1}{2}\left(\frac{\partial w}{\partial x_2'} + \frac{\partial v}{\partial x_3'}\right),$$

$$\xi = \frac{1}{2}\left(\frac{\partial w}{\partial x_2'} - \frac{\partial v}{\partial x_3'}\right),$$

η_c is the dynamic viscosity of the fluid, ω_1 is the angular velocity of the particle about the x_1' axis, and u, v, w are the three fluid-velocity components in the x_1', x_2', x_3'

directions. If the particle does not rotate (as would be the case in an equilibrium state when the hydrodynamic and electrostatic torques balance each other), Eq. (4.4) can be simplified as

$$T_{x_1'}^h = \frac{16\pi\eta_c\dot{\gamma}\left(a_2^2 m_2 n_3 - a_3^2 m_3 n_2\right)}{3\left(a_2^2\beta_0 + a_3^2\gamma_0\right)}, \tag{4.5}$$

where $\dot{\gamma}$ is the shear rate and the direction cosines of the x_1', x_2', x_3' axes referred to x_1, x_2, x_3, the coordinate system fixed in space, are (l_1, m_1, n_1), (l_2, m_2, n_2) and (l_3, m_3, n_3).

The torque applied by an electric field on the ellipsoidal particle can be obtained using the effective moment method [58]. The general form of the effective moment induced by the external field on an ellipsoidal particle of semi-axes a, b, c, can be expressed as

$$\vec{p}_{eff} = 4\pi a_1 a_2 a_3 \epsilon_f \underline{\widetilde{K}} \cdot \vec{E}, \tag{4.6}$$

where $\underline{\widetilde{K}}$ is the tensor form of complex Clausius-Mossotti factor,

$$\underline{\widetilde{K}} = \begin{pmatrix} \underline{K}_{x_1'} & 0 & 0 \\ 0 & \underline{K}_{x_2'} & 0 \\ 0 & 0 & \underline{K}_{x_3'} \end{pmatrix},$$

and $\underline{K}_{x_{1,2,3}'}$ are defined as

$$\underline{K}_{x_1'} = \frac{\underline{\epsilon}_p - \underline{\epsilon}_f}{3\left[\underline{\epsilon}_f + \frac{a_1 a_2 a_3}{2}\left(\underline{\epsilon}_p - \underline{\epsilon}_f\right)\alpha_0\right]},$$

$$\underline{K}_{x_2'} = \frac{\underline{\epsilon}_p - \underline{\epsilon}_f}{3\left[\underline{\epsilon}_f + \frac{a_1 a_2 a_3}{2}\left(\underline{\epsilon}_p - \underline{\epsilon}_f\right)\beta_0\right]},$$

$$\underline{K}_{x_3'} = \frac{\underline{\epsilon}_p - \underline{\epsilon}_f}{3\left[\underline{\epsilon}_f + \frac{a_1 a_2 a_3}{2}\left(\underline{\epsilon}_p - \underline{\epsilon}_f\right)\gamma_0\right]}, \tag{4.7}$$

and $\underline{\epsilon}_f$, $\underline{\epsilon}_p$ are the complex permittivities of the fluid and particle, respectively, and α_0 is defined as

$$\alpha_0 = \int_0^\infty \frac{ds}{\left(s + a_1^2\right) R_s}. \tag{4.8}$$

The x_1'-component of the torque due to the electric field is

$$T_{x_1'}^e = \frac{2}{3}\pi a_1^2 a_2^2 a_3^2 \epsilon_f \left(\gamma_0 - \beta_0\right) E_{x_2'} E_{x_3'} \mathbf{Re}\left[\underline{K}_{x_2'}\underline{K}_{x_3'}\right], \tag{4.9}$$

where $\epsilon_f = \mathbf{Re}\left(\underline{\epsilon}_f\right)$ and $E_{x_2'}, E_{x_3'}$ are electric-field components in x_2', x_3' directions, which depend on the orientation of the particle. The ratio of the x_1'-components of the

torques applied by the electric field and shear flow on the particle can be expressed using Eq. (4.9) and Eq. (4.5) as

$$\frac{T^e_{x'_1}}{T^h_{x'_1}} = \frac{a_1^2 a_2^2 a_3^2 \epsilon_f \left(a_2^2 \beta_0 + a_3^2 \gamma_0\right)\left(\gamma_0 - \beta_0\right) E_{x'_2} E_{x'_3} \mathbf{Re}\left[\underline{K}_{x'_2}\underline{K}_{x'_3}\right]}{8\eta_c \dot{\gamma}\left(a_2^2 m_2 n_3 - a_3^2 m_3 n_2\right)}. \tag{4.10}$$

For fixed fluid-and-particle properties, the electrostatic-to-hydrodynamic torque ratio is a function of $E^2/\dot{\gamma}$ and the particle orientation only, *i.e.*,

$$\frac{T^e}{T^h} = g\left(\theta, \phi, \psi\right) E^2/\dot{\gamma}, \tag{4.11}$$

where θ, ϕ, ψ are Eulerian angles as illustrated in Fig. 4.4. Below a critical electric-field strength, particles are expected to rotate in a modified Jeffery orbit, while, for sufficiently large field strengths, the electrostatic and hydrodynamic torques on each particle balance and the particles should reach an equilibrium orientation angle. This equilibrium angle is expected to be only a function of the parameter $E^2/\dot{\gamma}$, or equivalently, f, for all shear rates and field strengths.

In the following, we describe our experiments on SWNT suspensions under simultaneous shear flow and electric fields. The particle Reynolds numbers $Re = \dot{\gamma}l^2/\nu$ range from 10^{-10} to 10^{-7}, for the range of shear-rates, $\dot{\gamma}$, and particle lengths, l, of the current study. The measured SWNT orientation angles are quantitatively compared with the predictions of Mason-and-coworkers' classical theory for the orientational dynamics of an isolated ellipsoidal particle in a flowing Newtonian fluid subject to an external electric field. The apparent shear viscosity of the suspension is also simultaneously measured, in order to clarify what role, if any, particle orientation plays in determining the apparent viscosity of SWNT suspensions under electric fields.

4.3 Sample specification and characterization

The same purified HiPCO SWNTs used in the previous chapter were purchased in dry-powder form from CNI, Inc. and used as-received. The SWNTs are long, straight rods, having diameters of 1 nm and lengths of order $10^2 - 10^3$ nm, as seen from AFM imaging (Fig. 4.5) [79] and also reported by the manufacturer. Individual SWNTs are rigid rods
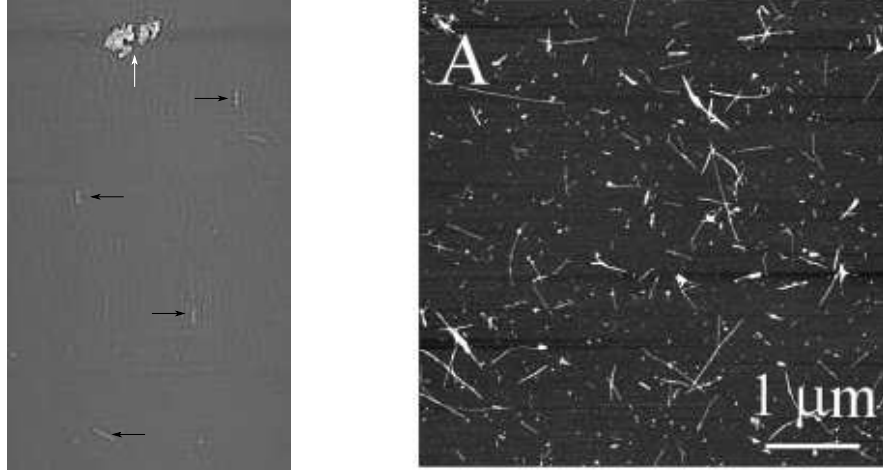
Figure 4.5: AFM images of HiPCO SWNTs deposited from suspension on a freshly cleaved mica substrate. Left: Our AFM visualization, with black arrows indicating straight, individualized nanotubes, and a white arrow showing a nanotube bundle. Right: Similar HiPCO SWNTs also visualized by AFM by Fagan et. al [79] 2006.

with persistence lengths $L_P = K/k_B T \sim 40$ microns [78,80] much greater than typical nanotube lengths. Even accounting for bending due to shear flow in our suspensions, the equivalent persistence length for individual SWNTs, calculated as $L_P/Pe_r \sim 2$ microns (where Pe_r is the rotational Peclet number that will be discussed in more detail later), is greater than the nanotube length. For a nanotube bundle, calculation of the persistence length requires detailed information of the lateral coherence between the N constituent tubes. However, if these N identical rods are aligned and can slip freely along each other, the total additive stiffness would be N times greater than L_P [80]. Thus, the SWNTs/bundles in our suspensions are treated as long, rigid rods.

The SWNTs were dispersed in a solvent, α-terpineol, which has low electrical conductivity and has been reported to be a good solvent for carbon nanotubes [69]. Samples at four different volume fractions of SWNTs, $\Phi = 1.5 \times 10^{-6}$, 3.7×10^{-6}, 1.5×10^{-5} and 2.2×10^{-5}, were prepared at room temperature with the assistance of bath sonication. As before, bath sonication was chosen rather than tip sonication because it has been shown to effectively disperse nanotubes with significantly less nanotube breakage [17]. For suspensions of high-aspect-ratio particles such as SWNTs, the transition

from "dilute" to "semi-dilute" regimes occurs at a cross-over volume fraction

$$\Phi_c = c_0 \pi / 4 r_e^2, \tag{4.12}$$

where $c_0 = 1$ in the strict Doi-Edwards formulation, while $c_0 \simeq 30$ based on experiments with poly(γ-benzyl-**L**-glutamate) [81]. If the empirical value of $c_0 \simeq 30$ is used, the dilute-to-semidilute-cross-over volume fraction is calculated to be $2.4 \times 10^{-5} - 2.4 \times 10^{-3}$ for aspect ratios ranging from 10^2 to 10^3, and all of our samples would be considered dilute. If the Doi-Edwards criterion [78] is used, our samples would still be likely to be dilute at the lowest concentrations tested. Moreover, considering that a portion of the nanotubes in solution are likely to be bundled rather than suspended as individual tubes, the suspensions tested are even more likely to be dilute, as the effective aspect ratio of the bundled nanotubes would be lower than the nominal value for individual nanotubes.
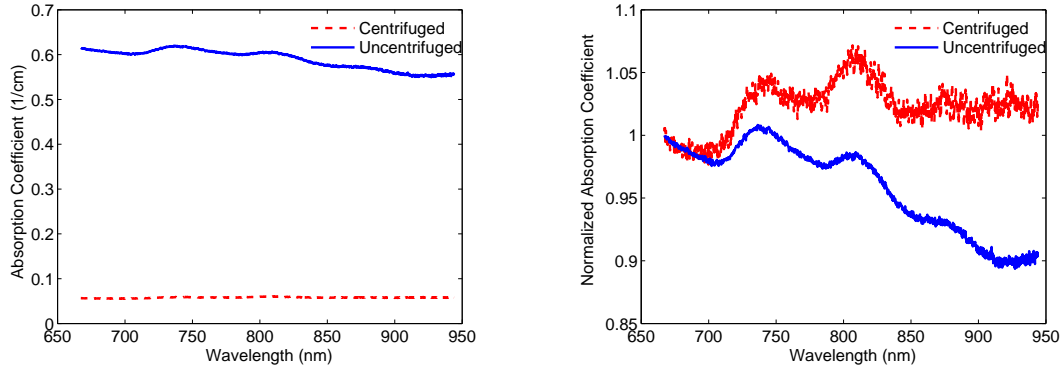
Figure 4.6: VIS-NIR absorption spectra of SWNTs/α-terpineol suspensions with and without centrifugation. Left: Absolute absorption. Right: Absorption spectra of centrifuged and uncentrifuged suspensions, normalized to have the same low wavelength absorption.

Analysis with a Brookhaven disc-centrifuge particle sizer showed that the particles in suspension were small, with 90% of particles/bundles present in the suspension having equivalent hydrodynamic diameters below 160nm. VIS-NIR absorbance measurements confirmed the presence of individual SWNTs in the suspension. As seen in Fig. 4.6, the absorption spectra of the SWNTs/α-terpineol suspension display characteristic peaks in the absorption spectra which correspond to the first inter-band M1

transition of individualized metallic SWNTs in suspension [21]. Such peaks would be suppressed by bundling of SWNTs in the suspension, as shown by [71]. Thus, the presence of such peaks indicates the presence of individual SWNTs in the suspensions. Suspensions with an enriched fraction of individual nanotubes were also prepared by centrifuging the original suspensions at 50,000g for 2.5 hours to remove larger particle bundles. As seen in Fig. 4.6, the overall absorption dropped after centrifugation due to the reduced concentration of nanotubes in the suspension. However, the relative height of the absorption peaks (normalized by the absorption at the low wavelengths) doubled after centrifugation, indicating an enrichment of the fraction of individualized SWNTs after centrifugation, as expected (Fig. 4.6: Right). Assuming that the relative peak height of the absorption features in the absorption spectrum serves as a rough measure of the degree of nanotube individualization, we may quantify the degree of dispersion by comparing our spectra with those of well-individualized suspensions using various surfactants, e.g. single-stranded DNA [79]. For example, the relative peak height (with respect to the background) of the peak near 750 nm for our centrifuged SWNTs/α-terpineol suspension is 0.05, while for DNA-wrapped SWNTs it is 0.15 and 0.14 (depending on the suspensions pH). Thus, our centrifuged suspensions contain perhaps 1/3 of the fraction of individualized SWNTs that the DNA-wrapped SWNT suspensions do. Nonetheless, the α-terpineol-SWNT suspensions studied here contained a mixture of bundled and individualized SWNTs, with a trend toward a greater percentage of individualized SWNTs after centrifugation. Measurement of the ensemble-averaged particle orientation angles under simultaneous shear flow and electric field were made with both the uncentrifuged and centrifuged suspensions, although measurements with the latter were limited due to the small sample volumes available.

It is also very important to note that the optical-polarization-modulation technique that is used to measure the ensemble-averaged particle orientation angles is sensitive to linear dichroism of the sample. The dichroism in this case is due to absorption anisotropy of aligned nanotubes [54, 82]. When the particles become much larger than the wavelength of light (632.8 nm for our HeNe laser), the absorption and scattering would no longer be anisotropic and linear dichroism is no longer be present, as discussed

by Fuller [83], who pioneered the measurement technique. As a result, the dichroism-based technique to measure the ensemble-averaged particle orientation is sensitive only to individual SWNTs and their small bundles; larger bundles do not contribute to the signal. We further confirmed that we are able to measure the orientation angles of samples that had been centrifuged at 50,000g for two and a half hours to remove large bundles. Thus, the measurement technique that is used in the present work ensures that the measured orientation angles are those of individual SWNTs and small bundles.

4.4   Experimental method
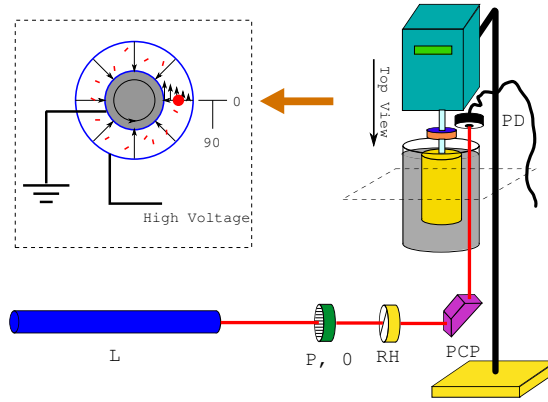
Figure 4.7: Schematic of the modified concentric-cylinder viscometer and the laser-polarimetry system used to simultaneously measure apparent viscosities and ensemble-averaged particle-orientation angles. **L**: HeNe laser, **P,0**: Polarizer at 0 °, **RH**: Rotating half-wave plate, **PCP**: Polarization-conserving prism, **PD**: Photodetector.

The electrorheological (ER) measurement was carried out in a modified concentric-cylinder cell (Fig. 4.7) of a Brookfield DVII+ viscometer at a fixed temperature of 25°C. The concentric-cylinder cell was redesigned in two aspects. First the gap between the inner and outer cylinder was increased to 3.2mm to accommodate a laser beam of diameter of 1.2mm. Secondly, the bottom of the outer cylinder was removed and replaced with an optical window and a sealing cap. A shear-flow field in the circumferential direction was generated by the strain-rate-controlled viscometer unit while an external electric field was formed in the radial direction by applying a potential difference between the inner and outer cylinders.

A laser-polarimetry system, based on the optical-rheometry schemes developed by Fuller [68], was used to measure the ensemble-averaged orientation of the individually suspended and small bundles of SWNTs. As seen in Fig. 4.7, the optical train consisted of a linearly polarized laser at a wavelength of 632nm, a Glan-Taylor polarizer having $1:10^6$ extinction ratio, a rotary half-wave plate, a polarization-conserving, 90°-beam-deflecting prism [84], and a photodetector. The rotary half-wave plate, which served as a polarization modulator, was driven by a pulley-motor system with adjustable RPM up to 5200. Post-sample light was received by a photodetector and demodulated and further processed by a lock-in amplifier using the signal from the motor encoder as a reference signal. To test the optical system, a calibration was performed using another Glan-Taylor calcite polarizer oriented at known angles. Fig. 4.8 shows the calibration results. The calibration showed that the orientation-angle measurement was accurate within 0.1°, which was also the resolution of the rotation stage used in this calibration process.

Repeatability of the results for both apparent-viscosity and ensemble-averaged orientation angle measurements was examined by measuring selected samples several times, as well as measuring different sample loadings on different days. The largest source of error in the optical measurements came from the initial positioning of the sample cell relative to the laser beam. This systematic error, which could be corrected in post processing, was within 5° difference from trial to trial. The random error for the apparent-viscosity measurement was within 1% of the viscosity measurement range. A pure α-terpineol sample was tested to ensure that the viscosity and dichroism of the solvent itself did not change upon the application of the external electric field.

For the range of shear rates of the current study, the suspensions are non-Brownian. The rotational Peclet number , $Pe_\mathrm{r} \equiv \dot{\gamma}/D_\mathrm{r}$, defined as the ratio of the shear rate, $\dot{\gamma}$, to the rotary diffusion coefficient, D_r, is a measure of relative viscous and thermal effects. For rigid, rod-like particles, the rotary diffusion coefficient is [78, 85]

$$D_\mathrm{r} = \frac{3k_BT\left[ln\left(l/d\right) - 0.8\right]}{\pi\eta_cL^3},\tag{4.13}$$

where l and d are the length and diameter of the particle. For our experiment, the
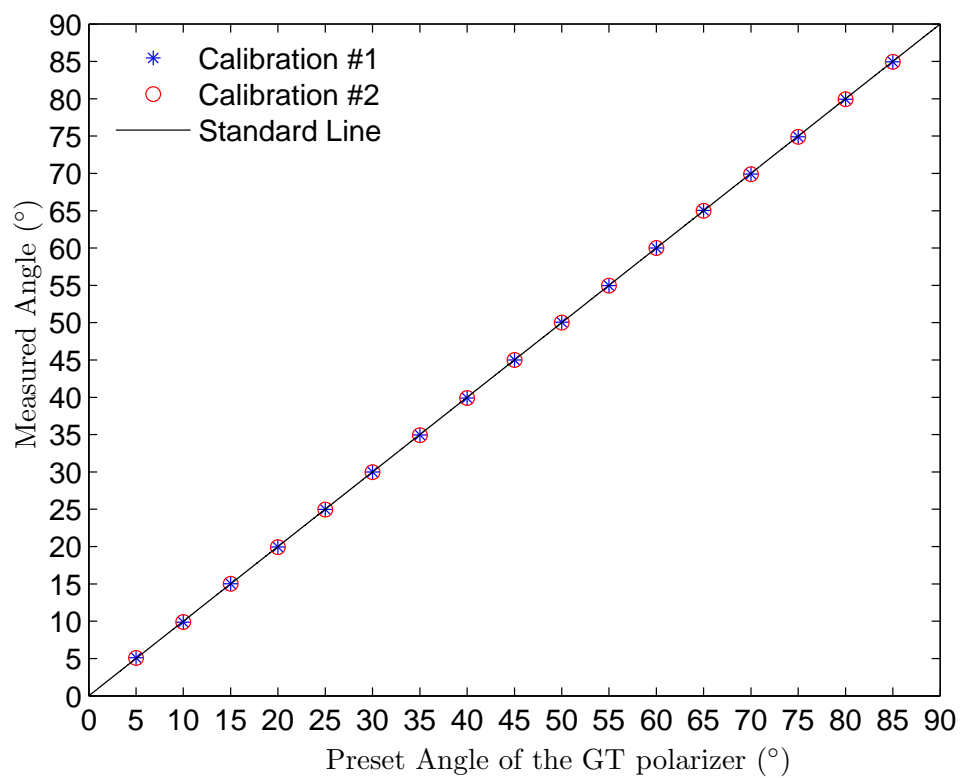
Figure 4.8: The calibration of our optical system using a Glan-Taylor polarizer oriented at known angles.

calculated values of Pe_r are in the range of $2 \sim 18$ for the shear rates used, assuming individual nanotubes of length $l \simeq 1$ μm in the suspensions. Even for shorter tubes, considering that for nearly all of the conditions studied, $f \gg 1$, $i.e.$, the electric field is very strong, Brownian motion is not expected to have a significant effect on the results.

4.4.1 Mathematical analysis of optical polarimetry setup

We have laid the basis for light scattering by small particle in our background chapter. Before we get into the experimental results of particle orientation measurements, it is necessary to have a detailed description about the methodology we used in designing and interpreting our experiments.

Two mathematical descriptions of polarized light are often utilized to analyze optical polarimetry measurements: Jones and Mueller calculus. The Jones calculus uses a Jones vector which is the same as the electric field vector itself to represent the polarized light, while in the Mueller calculus the representation of the polarized light is carried out by four quantities known as the Stokes parameters which are functions only of observables of the electromagnetic wave. Since the analysis of the same polarimetry experiment can be accomplished by either one of these two mathematical methods, Jones and Mueller calculus are equivalent [86]. When the polarized light interacts with materials or passes through any optical elements, the incident beam and the emerging light wave are linearly related by a transformation matrix. In the case of Jones calculus, the mathematical expression is

$$\vec{E}_t = J\vec{E}_i, \tag{4.14}$$

where $\vec{E}_i$ and $\vec{E}_t$ are Jones vectors of a polarized incident and transmitted wave respectively and J is the Jones matrix for a particular sample material or an optical component. Similarly in Mueller calculus, Mueller matrix is the transformation matrix which relates the Stokes vectors of the incident to the transmitted wave.

$$\vec{S}_1 = M\vec{S}_0, \tag{4.15}$$

where $\vec{S}_0$ and $\vec{S}_1$ are Stokes vectors of a polarized incident and transmitted wave respectively and M is the Mueller matrix. Notice that Jones vector has two components

while Stokes vector has four components, therefore Jones matrix J is a 2×2 matrix and Mueller matrix M is a 4×4 matrix. Since Jones and Mueller calculus are interchangeable [86] and the latter has the direct observable, the intensity of the polarized light, as the first component of Stokes vector, the mathematical analysis of our optical polarimetry experiments will be described in the form of Mueller calculus. For a sequence of optical elements encountered in an optical train the resulting Stokes vector of the light is the product of the incident light and each of the corresponding Mueller matrix of the optical elements

$$\vec{S}_N = M_N \cdot M_{N-1} \cdots M_2 \cdot M_1 \cdot M_0 \cdot \vec{S}_0. \tag{4.16}$$

The Mueller matrix of each of the optical elements depicted in Fig. 4.7 can be found in Appendix II, assuming our sample suspensions are coaxial birefringent/dichroic medium. Since the linearly polarized light source can be treated as a result of an unpolarized light passing through a polarizer, a Stokes vector, $\vec{S}_0 = \begin{pmatrix} I_0 \\ 0 \\ 0 \\ 0 \end{pmatrix}$, of an unpolarized light with a polarizer as the first optical element will be used as our starting point of the mathematical analysis.

$$
\begin{aligned}
\vec{S}_1 &= M_0 \cdot \vec{S}_0 \\
&= \frac{1}{2} \begin{pmatrix} 1 & 1 & 0 & 0 \\ 1 & 1 & 0 & 0 \\ 0 & 0 & 0 & 0 \\ 0 & 0 & 0 & 0 \end{pmatrix} \begin{pmatrix} I_0 \\ 0 \\ 0 \\ 0 \end{pmatrix} \\
&= \frac{1}{2} \begin{pmatrix} I_0 \\ I_0 \\ 0 \\ 0 \end{pmatrix},
\end{aligned} \tag{4.17}
$$

The polarized beam is then transmitted through a rotating half-wave plate driven

by a pulley-motor system

$$
\begin{aligned}
\vec{S}_2 &= M_1 \cdot \vec{S}_1 \\
&= \frac{1}{2}
\begin{pmatrix}
1 & 0 & 0 & 0 \\
0 & \cos 4\left(\omega t + \beta_0\right) & \sin 4\left(\omega t + \beta_0\right) & 0 \\
0 & \sin 4\left(\omega t + \beta_0\right) & -\cos 4\left(\omega t + \beta_0\right) & 0 \\
0 & 0 & 0 & -1
\end{pmatrix}
\begin{pmatrix}
I_0 \\
I_0 \\
0 \\
0
\end{pmatrix} \\
&= \frac{1}{2}
\begin{pmatrix}
I_0 \\
I_0 \cos 4\left(\omega t + \beta_0\right) \\
I_0 \sin 4\left(\omega t + \beta_0\right) \\
0
\end{pmatrix},
\end{aligned}
\tag{4.18}
$$

Finally, the rotating linearly polarized light is passed through a sample SWNT suspension under both shear flow and electric field in the modified concentric cylindrical cell of the Brookfield viscometer. The sample suspensions are assumed to have coaxial dichroism and birefringence with the extinction and retardation defined as

$$
\delta'' = 2\pi \Delta n'' d/\lambda
\tag{4.19}
$$

$$
\delta' = 2\pi \Delta n' d/\lambda,
\tag{4.20}
$$

where d is the optical path length of the sample. The Mueller matrix for sample materials with both dichroism and birefringence can be found in Fuller's paper [68].

The Stokes vector of the resulting light after the sample suspension becomes

$$
\begin{aligned}
\vec{S}_3 &= M_2 \cdot \vec{S}_2 \\
&= \frac{1}{2}I_0 \begin{pmatrix}
\cosh(\delta'') & -\cos(2\alpha)\sinh(\delta'') \\
-\cos(2\alpha)\sinh(\delta'') & \cos^2(2\alpha)\sinh(\delta'') + \sin^2(2\alpha)\cos(\delta') \\
-\sin(2\alpha)\sinh(\delta'') & \cos(2\alpha)\sin(2\alpha)\left(\cosh(\delta'') - \cos(\delta')\right) \\
0 & -\sin(2\alpha)\sin(\delta')
\end{pmatrix}
\end{aligned}
$$

$$
\begin{pmatrix}
-\sin(2\alpha)\sinh(\delta'') & 0 \\
\cos(2\alpha)\sin(2\alpha)\left[\cosh(\delta'') - \cos(\delta')\right] & \sin(2\alpha)\sin(\delta') \\
\sin^2(2\alpha)\cosh(\delta'') + \cos^2(2\alpha)\cos(\delta') & -\cos(2\alpha)\sin(\delta') \\
\cos(2\alpha)\sin(\delta') & \cos(\delta')
\end{pmatrix}_{4\times4}
\begin{pmatrix}
1 \\
\cos 4(\omega t + \beta_0) \\
\sin 4(\omega t + \beta_0) \\
0
\end{pmatrix}
$$

$$
= \frac{1}{2}I_0 \begin{pmatrix}
\cosh(\delta'') - \cos 4(\omega t + \beta_0)\cos(2\alpha)\sinh(\delta'') \\
-\cos(2\alpha)\sinh(\delta'') + \cos 4(\omega t + \beta_0)\left[\cos^2(2\alpha)\sinh(\delta'') + \sin^2(2\alpha)\cos(\delta')\right] \\
-\sin(2\alpha)\sinh(\delta'') + \cos 4(\omega t + \beta_0)\cos(2\alpha)\sin(2\alpha)\left[\cosh(\delta'') - \cos(\delta')\right] \\
-\cos 4(\omega t + \beta_0)\sin(2\alpha)\sin(\delta')
\end{pmatrix}
$$

$$
\begin{pmatrix}
-\sin 4(\omega t + \beta_0)\sin(2\alpha)\sinh(\delta'') \\
+\sin 4(\omega t + \beta_0)\cos(2\alpha)\sin(2\alpha)\left[\cosh(\delta'') - \cos(\delta')\right] \\
+\sin 4(\omega t + \beta_0)\left[\sin^2(2\alpha)\cosh(\delta'') + \cos^2(2\alpha)\cos(\delta')\right] \\
+\sin 4(\omega t + \beta_0)\cos(2\alpha)\sin(\delta')
\end{pmatrix}_{4\times1}. \tag{4.21}
$$

A polarization conserving light bending prism [84] is used to deflect the beam before the sample suspension due to the space limitation. Since the prism changes the propagation direction of the light without changing the polarization state of the light, it is not necessary to include the function of the the prism in the mathematical analysis. The intensity of the after-sample beam will be collected by a photodetector as

$$
\begin{aligned}
I &= \frac{1}{2}I_0 \left[\cosh(\delta'') - \cos 4(\omega t + \beta_0)\cos(2\alpha)\sinh(\delta'') - \sin 4(\omega t + \beta_0)\sin(2\alpha)\sinh(\delta'')\right] \\
&= \frac{1}{2}I_0 \cosh(\delta'') \left[1 - \cos 4(\omega t + \beta_0)\cos(2\alpha)\tanh(\delta'') - \sin 4(\omega t + \beta_0)\sin(2\alpha)\tanh(\delta'')\right] \\
&= \frac{1}{2}I_0 \cosh(\delta'') \left\{1 - \cos\left[4\omega t - (2\alpha - 4\beta_0)\right]\tanh(\delta'')\right\} \\
&= \frac{1}{2}I_0 \cosh(\delta'') \left\{1 - \sin\left\{4\omega t + \left[\frac{\pi}{2} - (2\alpha - 4\beta_0)\right]\right\}\tanh(\delta'')\right\} \tag{4.22}
\end{aligned}
$$

The signal from the photodetector will go through a DC (low-cut) filter so that

only the $\sin(4\omega t)$ component of the signal is left. Then it is demodulated and further processed by a lock-in amplifier. Both the magnitude and phase of $\sin(4\omega t)$ component of the signal will be extracted. Two unknown angles need to be determined, the initial phase angle of the half-wave plate, β_0, and the orientation angle of the dichroism of the suspension, α. β_0 is determined in the same fashion at the beginning of each experiment by replacing the sample with a known angle (usually $90°$, so $\alpha = 90°$) polarizer. α, or equivalently, the ensemble average of the particle orientations at equilibrium state will be obtained from the phase information of signal $\sin(4\omega t)$ after the β_0 is known.

4.5   Results and discussion

Representative time traces of the measured apparent viscosity, η, normalized by the viscosity of the solvent, η_c, at a volume fraction of $\Phi = 1.5 \times 10^{-5}$ are shown in Fig. 4.9 for a constant shear rate of $2.81\ s^{-1}$ and various electric-field strengths. Before the field is turned on, the suspension viscosity is the same as the base fluid viscosity to within the experimental precision because of the low particle concentration. With an electric field, the shear viscosity increases, with the magnitude of the viscosity change increasing, and the time scale of the viscosity change decreasing, with field strength. Despite the diluteness of the suspension, the apparent viscosity nearly triples at the highest electric field for this shear rate. The response time for the viscosity change is very slow, on the order of 10^2 seconds, however. These apparent-viscosity results are consistent with those previously obtained with a different measurement cell [42].

Ensemble-averaged particle orientations, measured simultaneously with the viscosity measurements, are shown in Fig. 4.10 for the same electric-field strengths and shear rate. In the absence of an electric field, the large-aspect ratio nanotubes can be expected [45, 46, 87] to rotate periodically in Jeffery orbits, spending most of their time aligned in the flow direction. As seen in Fig. 4.10, the ensemble-averaged particle-orientation angle without the electric field is in the flow direction ($90°$ as defined in our coordinate system). This is consistent with the predicted Jeffery orbits, and would seem to rule out purely chaotic orbits which might rise due to the existence of triaxial-ellipsoid-like particles [88]. Upon application of the electric field at $t = 160s$, the measured
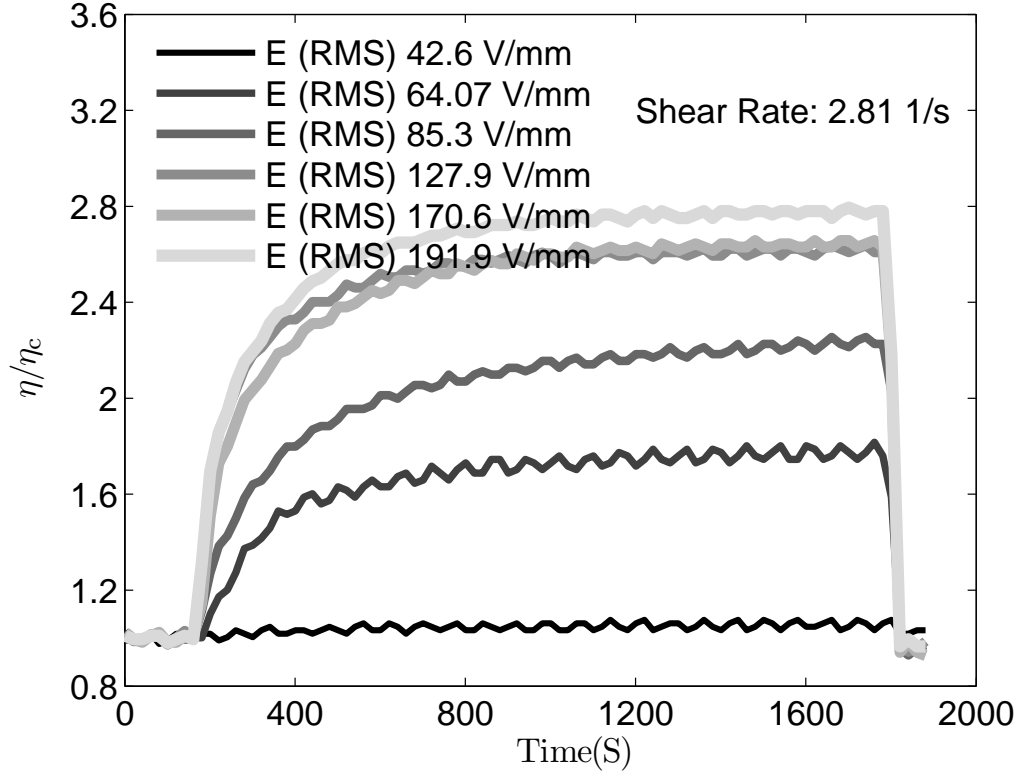
Figure 4.9: Time traces of the normalized apparent viscosity of the suspension. Various electric-field strength were applied while the shear rate was kept at a constant value $\dot{\gamma} = 2.81\ 1/s$.

equilibrium orientation angles quickly deviate towards the radial direction $(0°)$. The alignment of nanotubes in the radial direction is increased with an increase in field strength, reaching $33°$ at a shear rate of $2.81\ s^{-1}$ for $E_{\mathrm{rms}} = 191$ V/mm. Once the electric field is turned off at $t = 1900$ s, the nanotube orientations return to the flow direction $(90°)$, again consistent with Jeffery's predictions [45] and experiments by Taylor [46] and Mason and coworkers [87].

The alignment of the nanotubes in the simultaneous shear flow and electric field occurs on time scales on the order of $10^0 - 10^1$ seconds (Fig. 4.10), one to two orders of magnitude faster than the time scales of the rheological response (Fig. 4.9). Thus, at these low concentrations, the alignment of the particles with the electric field appears to have little direct impact on the apparent viscosity of the suspension, despite the very
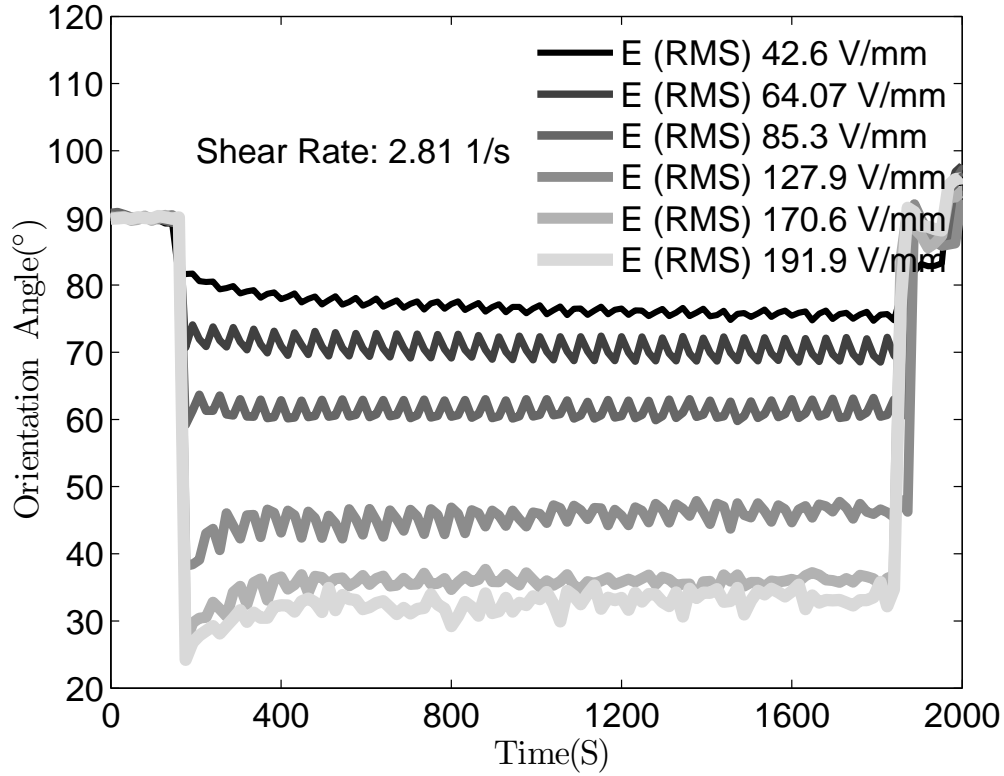
Figure 4.10: Equilibrium particle-orientation angles, measured simultaneously with the electrorheological data shown in Fig. 4.9.

large aspect ratio of the nanotubes. Rather, consistent with the behavior of conventional ER fluids [25, 30–32], the chaining of nanotubes under dipole-dipole interactions appears to be the primary mechanism for the change in apparent viscosity under an external electric field. In this light, the slow ER time response observed in these experiments is due to the diluteness of the SWNT suspensions, which increases the mean spacing between particles (and thus the chaining time) in the suspension. Similarly slow response times on the order of minutes have also been reported for an ER fluid composed of carbon-cone particles at low concentration [89].

Fig. 4.11 plots the measured ensemble-averaged particle orientation angle against shear rate at different electric field strength. And Fig. 4.12 plots the measured orientation angle against electric field strength at different shear rate. As the effects of the two fields applied on particles compete with each other at various electric and shear fields,
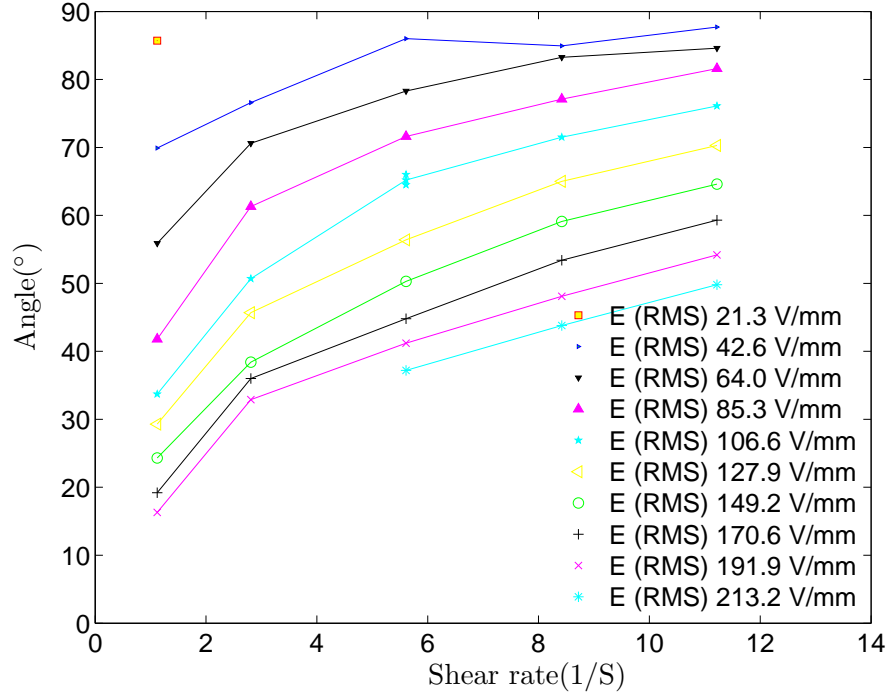
Figure 4.11: Particle orientation angle as a function of shear rate at various electric field strength.

the equilibrium orientation angle vary accordingly. Higher electric field strength drives the particles more towards 0° while higher shear rate pushes them on the direction perpendicular to the electric field direction, which is 90° as defined in our system.

Mason's theory predicts that particles under both shear and electric field align themselves at a specific equilibrium orientation angle when the externally applied electric field strength is greater than a critical value, E_{crit}, at which $f = 1$. To experimentally validate this E_{crit} for the SWNTs/α-terpineol suspensions, the electric field applied to the suspension was increased until deviation from preferential orientation in the flow direction was detected. Fig. 4.13 shows the measured ensemble-averaged orientation angles for varying electric-field strengths for the $\Phi = 1.5 \times 10^{-5}$ sample at a fixed shear rate of $\dot{\gamma} = 5.61$ s^{-1}. Two linear curve fits were applied to data for the seven lowest field-strengths in order to obtain an experimental $E_{\mathrm{crit}} = 19 V_{\mathrm{rms}}$/mm. Since the real samples are polydispersed, with particles/bundles having a range of aspect ratios, care must be taken in calculations of the theoretical value of E_{crit} in Eq. (4.3). For
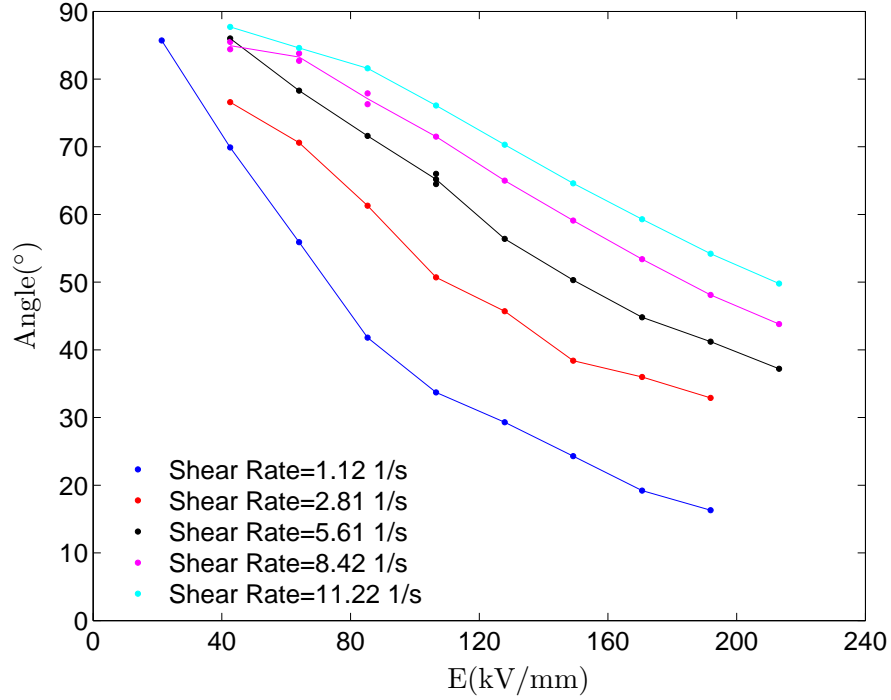
Figure 4.12: Particle orientation angle as a function of electric field stength at various shear rate.

particles/bundles with aspect ratios ranging from 10^2 to 10^3, the calculated theoretical values of E_{crit} range between $20.6V_{\text{rms}}/\text{mm}$ and $63.9V_{\text{rms}}/\text{mm}$, which is in reasonable agreement with the experimentally determined value $E_{\text{crit}} = 19V_{\text{rms}}/\text{mm}$.

The equilibrium orientation angles for various shear rates and electric-field strengths are plotted in Fig. 4.14 against the parameter $\text{E}^2/\dot{\gamma}$ predicted by Mason's theory to govern the orientation of ellipsoidal polarizable particles in simultaneous shear flow and electric fields (Eq. 4.2). As seen in the figure, the measured orientation angles collapse well against $\text{E}^2/\dot{\gamma}$ for an order-of-magnitude variation in both electric-field strengths ($21.3V_{\text{rms}}/\text{mm} \leq E \leq 383.7V_{\text{rms}}/\text{mm}$) and shear rates ($1.12s^{-1} \leq \dot{\gamma} \leq 11.22s^{-1}$). The collapse of the data indicates that the $\text{E}^2/\dot{\gamma}$-dependence for the equilibrium orientation angle predicted by Mason's theory is essentially correct. One would also expect based on Eq. (4.2) that particles will align along the electric field direction ($0°$) when the parameter $\text{E}^2/\dot{\gamma} \to \infty$, $i.e.$, the electric field is much stronger than the shear flow. In order to experimentally approach this upper limit, an electric field of $213.2V_{\text{rms}}/\text{mm}$ was
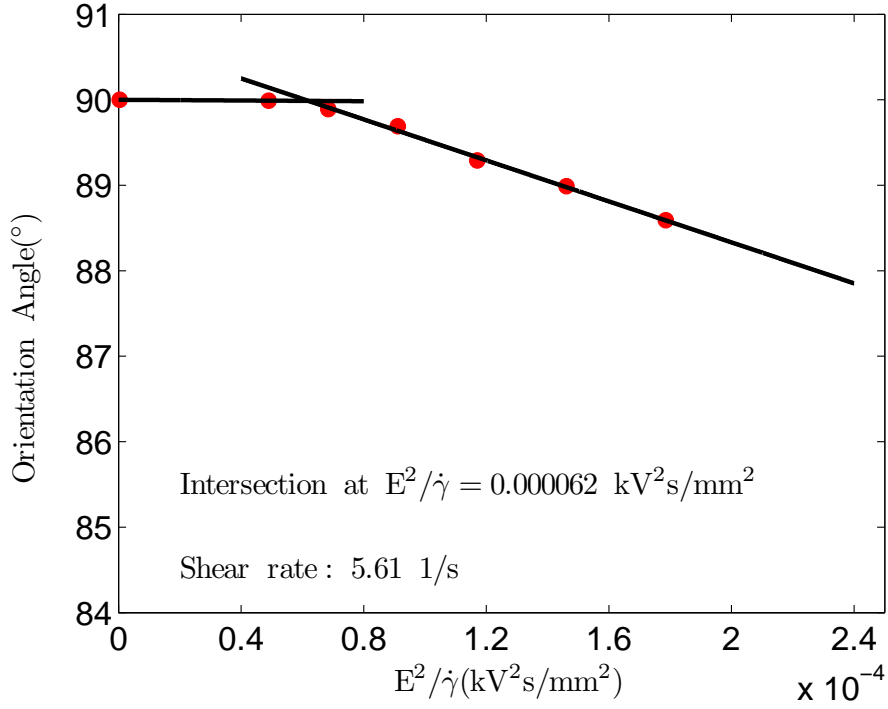
Figure 4.13: Two linear curve fits applied to the first seven measured equilibrium particle-orientation data points to determine E_{crit}.

applied to two quiescent samples. The measured ensemble-averaged orientation angles (not shown in Fig. 4.14) were 6.9° and 3.3° for the uncentrifuged ($\Phi = 1.5 \times 10^{-5}$) and centrifuged suspensions, respectively, in reasonable agreement with theory.

However, significant discrepancies are found between the experimental results and the theoretical predictions at the intermediate values of f (or $E^2/\dot{\gamma}$). Shown in Fig. 4.14 are also the predicted orientation angles from Eq. (4.2) for particles of aspect ratio $r_e = 10$, 100, and 1000. The model predictions of the particle orientation angle are seen to be essentially independent of the aspect ratio in this high-aspect-ratio range. Thus, the polydispersity of the suspension (*i.e.*, the broad distribution of nanotube lengths in the actual sample) is irrelevant to the expected orientation angles. However, as seen in Fig. 4.14, the measured angles fall below the theory (inclined toward the electric-field direction) by as much as 40°. This implies a higher aligning torque (either electrostatic or hydrodynamic) in the electric-field direction than predicted by simple theory. Thus,
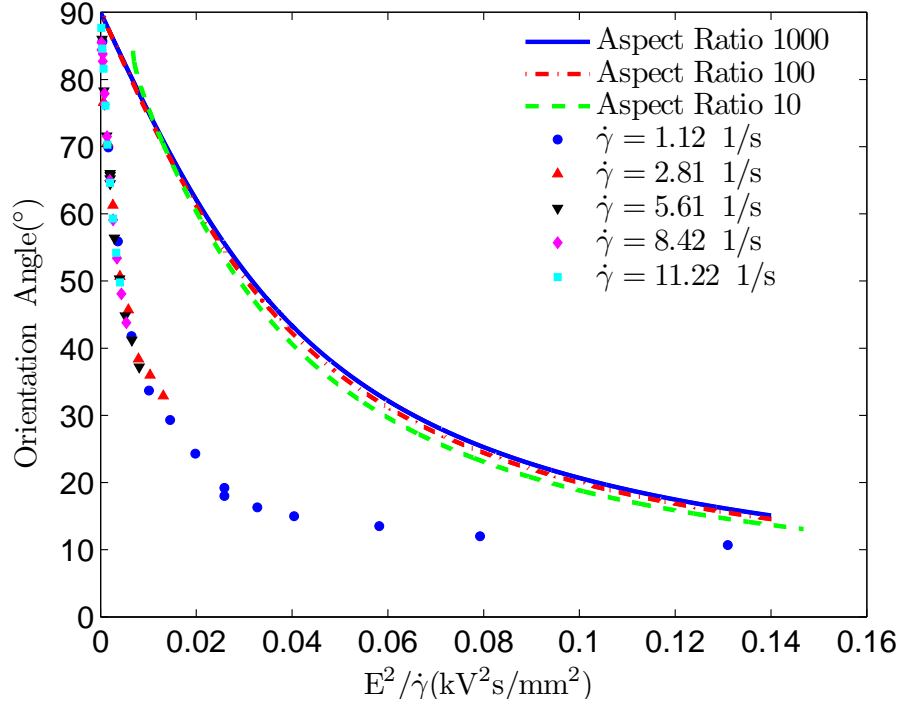
Figure 4.14: Measured equilibrium orientation angles as a function of $E^2/\dot{\gamma}$. Predicted angles (Eq. 4.2) are shown for three particle aspect ratios.

while the collapse of the data for various shear rates and electric fields indicates that the particle orientation is indeed governed by the ratio between electric-field and shear-flow torques, as parameterized by $E^2/\dot{\gamma}$, or equivalently f, Eq. (4.2) does not completely predict SWNT orientation in these suspensions.

One possible source of the discrepancy between the experiment and Mason's prediction is particle-particle interaction, which is neglected in the classical theory. To examine the possible role of such particle-particle interactions on the equilibrium orientation angles, we further tested suspensions of different SWNT volume fraction. If particle-particle interactions were indeed responsible for the observed discrepancies, one would expect the measured angles to agree better with the theoretical curve at lower SWNT concentrations, when the mean spacing between particles is larger. As seen in Fig. 4.15, this was indeed the case, with better agreement between the measured angles and the model for less concentrated samples. Even at the lowest concentrations

however, which are almost certainly dilute in the sense that particles are unlikely to interact through random rotations in the absence of an external electric field (Eq. 4.12), significant discrepancies persist between the measurements and theoretical predictions. Nonidealities due to bundling of the particles are unlikely to account for the difference, as a sample which had been centrifuged at 50,000g for 2.5 hours to remove large particles still showed a significant discrepancy from theory. To better understand the possible role that particle-particle interactions may have on the equilibrium orientation angles, we next consider to lowest order the effect of electrostatic interaction between two neighboring spheroidal particles.
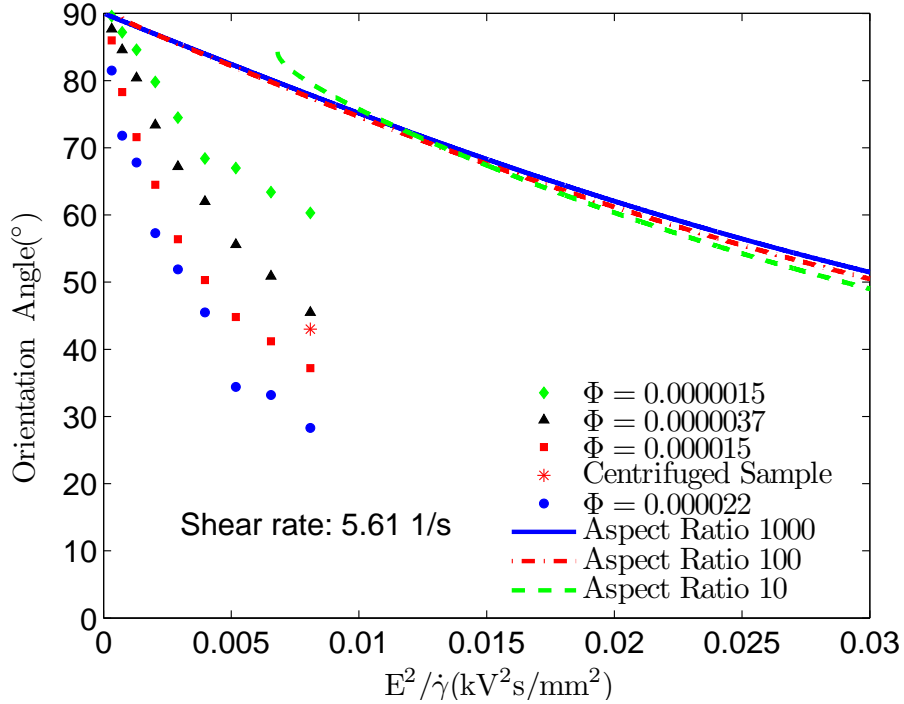
Figure 4.15: Concentration effects on the equilibrium orientation angle of SWNTs/bundles under shear and electric fields. Lines show the predictions of classical theory (Eq. 4.2) for various particle aspect ratios.

The simplest model for the effect of electrostatic interactions is to consider the disturbance field generated by a dipole and calculate its effect on a nearby dipole. For simplicity, we present here only the special case when the major axes of the two prolate particles are parallel and the line (vector $\vec{r}$ in Fig. 4.4) connecting the centroid of the

two particles lies in the electric field direction. The special case is illustrative without the additional complexity that would arise from considering all possible arrangements of pairs of particles. The inset of Fig. 4.4 depicts the configuration of the particle pair, the coordinate system, and the external electric and flow fields. The effective moment of a particle in a uniform field $\vec{E}$ is

$$\vec{p}_{eff} = 4\pi a b^2 \epsilon_f \left(\underline{K}_\parallel E_\parallel \hat{\vec{e}}_\parallel + \underline{K}_\perp E_\perp \hat{\vec{e}}_\perp \right), \tag{4.23}$$

where $\hat{\vec{e}}_\parallel$ and $\hat{\vec{e}}_\perp$ are unit vectors parallel and perpendicular to the major axes of the particles respectively. In the limit of $r_e \gg 1$ for high-aspect-ratio particles, the two Clausius-Mossotti factors in Eq. (4.23) simplify to

$$\underline{K}_\parallel = \frac{\underline{\epsilon}_2 - \underline{\epsilon}_1}{3\{\underline{\epsilon}_1 + \frac{1}{r_e^2} (\underline{\epsilon}_2 - \underline{\epsilon}_1) [ln\,(2r_e) - 1]\}}$$

$$\underline{K}_\perp = \frac{2\,(\underline{\epsilon}_2 - \underline{\epsilon}_1)}{3\,(\underline{\epsilon}_2 + \underline{\epsilon}_1)}. \tag{4.24}$$

The electric field generated at a location $\vec{r}$ by a particle of effective moment $\vec{p}_{eff}$ centered at origin is [60]

$$\vec{E}_{\text{dipole}}\,(\vec{r}) = \left(\frac{1}{4\pi\epsilon_f} \right) \frac{\left[3 \left(\vec{p}_{eff} \cdot \hat{\vec{r}} \right) \hat{\vec{r}} - \vec{p}_{eff} \right]}{r^3}, \tag{4.25}$$

where the unit vector $\hat{\vec{r}} = \vec{r}/r$ in the direction of the line connecting the centers of the two particles is

$$\hat{\vec{r}} = \cos\,(\delta - \phi)\,\hat{\vec{e}}_\parallel - \sin\,(\delta - \phi)\,\hat{\vec{e}}_\perp. \tag{4.26}$$

The torque $\vec{T} = \vec{p} \times \vec{E}$ due to electrostatic interactions with a neighboring particle is calculated to lowest order using the disturbance electric field of Eq. (4.25), and the dipole moment $\vec{p}_{eff}$ induced by the uniform electric field. Compared to the torque applied by the uniform external electric field (Eq. 4.9), the torque due to the electrostatic

interaction with a neighboring particle is, to lowest order,

$$
\begin{aligned}
\frac{T^e_{\text{induced}}}{T^e} &= \frac{3ab^2}{r^3} \frac{\left\{ \underline{K}_\parallel \underline{K}_\perp \sin(2\phi) \cos[2(\delta-\phi)] - \left(\underline{K}_\perp \underline{K}_\perp \sin^2\phi - \underline{K}_\parallel \underline{K}_\parallel \cos^2\phi \right) \sin[2(\delta-\phi)] \right\}}{\left(\underline{K}_\perp - \underline{K}_\parallel \right) \sin 2\phi} \\[2mm]
&\sim \frac{9\Phi}{4\pi} \frac{\left\{ \underline{K}_\parallel \underline{K}_\perp \cos(2\phi) + \left(\underline{K}_\perp \underline{K}_\perp \sin^2\phi - \underline{K}_\parallel \underline{K}_\parallel \cos^2\phi \right) \right\}}{\underline{K}_\perp - \underline{K}_\parallel}, \qquad (\delta = 0^\circ) \\[2mm]
&= \begin{cases} \frac{9\Phi}{4\pi} \underline{K}_\parallel & (\phi = 0^\circ) \\[2mm] \frac{9\Phi}{4\pi} \underline{K}_\perp & (\phi = 90^\circ) \end{cases}
\end{aligned}
\tag{4.27}
$$

In Fig. 4.16, this additional aligning torque due to electrostatic interaction is plotted against particle separation distance r for the special case when the line connecting the centers of the particles becomes parallel to the electric field (*i.e.*, $\delta = 0^\circ$). It is also assumed that the conductivities dominate the response, as they would in the low frequency ($\Omega \ll 2\pi/\tau_{\text{Maxwell-Wagner}}$) case [31] considered here and that $\sigma_f/\sigma_p \ll 1$. The result does not depend strongly on the exact conductivities for $\sigma_f/\sigma_p \ll 1$, and we assume conservatively in our calculation that $\sigma_f/\sigma_p = 10^{-6}$. The polarizability of SWNT along its main tube axis is calculated using Eq. (3.3) to be 0.034 μm^3 in vacuum which within a factor of three of independent experimental results [54]. As seen in Fig. 4.16, the electrostatic torque due to interaction with a neighboring particle is of the same sign as that of a dipole in a uniform field, *i.e.*, it tends to increase particle alignment with the electric-field direction. This is consistent with the measured orientation angles in Fig. 4.14, which consistently fell below the predictions of the theoretical model that neglects particle-particle interactions. The additional torque acting on the particle due to electrostatic interaction with a neighboring particle varies as r^{-3}, and become an appreciable fraction of electrostatic alignment torque for separation distances on the order of microns. The samples used in the present study have mean particle spacings between 0.3 microns (for $\Phi = 2.2 \times 10^{-5}$) and 0.8 microns (for $\Phi = 1.5 \times 10^{-6}$) calculated (assuming individual particles) using

$$
R_{ij} = n^{-\frac{1}{3}} = \left(\frac{\pi d^2 l}{4\Phi} \right)^{\frac{1}{3}},
\tag{4.28}
$$

where R_{ij} is the mean particle spacing and n is the particle number density. Thus, electrostatic interactions between neighboring particles can have a significant effect

on equilibrium orientation of the nanotubes, despite the apparent "diluteness" of the suspension by some conventional measures.
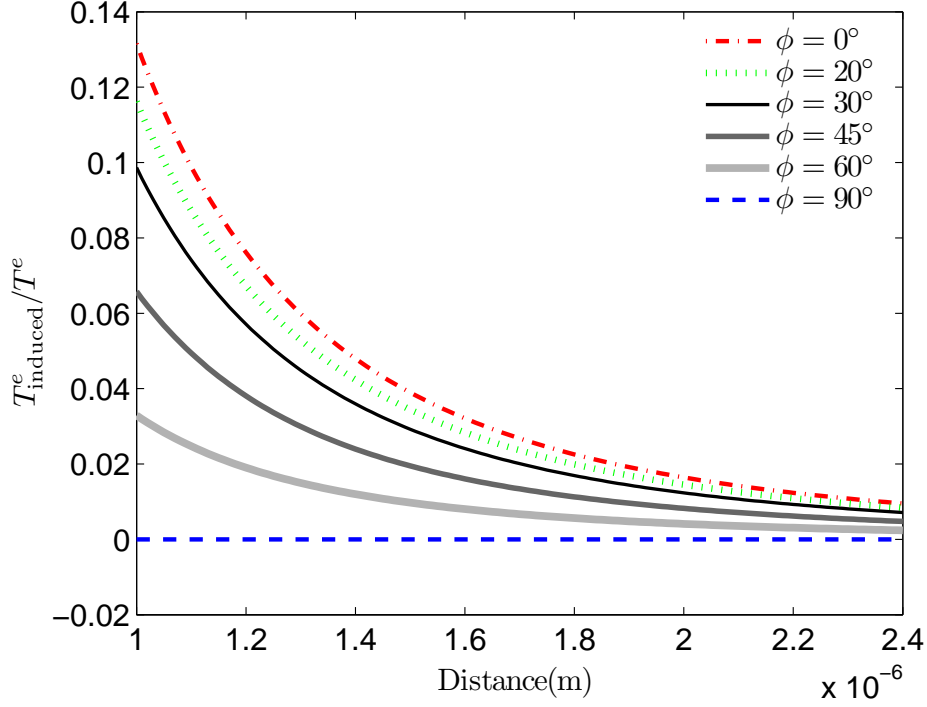
Figure 4.16: Calculated electrostatic-interaction torque as a function of the spacing between two neighboring particles for various particle-orientation angles. The SWNT length is assumed to be 1 μm. Interaction torque is normalized by the torque of the dipole in a uniform field.

It should be noted that, while it is clear that electrostatic interactions that draw the particles together are important on long time scales, it is not *a priori* obvious that electrostatic interactions would also affect particle orientations at short time scales, at the onset of the electric field, before particles have had a chance to move together. Moreover, electrostatic interactions need not necessarily affect the orientation of the particles even when the dipole-dipole force is significant. For example, in ordinary ER suspensions with spherical particles, the dipolar interaction force is significant, but there is no electrostatic interaction torque that would change the orientation of the particles. For the case of the SWNTs, however, it can be seen from Eq. (4.27) that, in the limiting case when both $\delta = 0°$ and $\phi = 0°$, the electrostatic-interaction torque on a particle

scales as $\Phi \underline{K}_\parallel$. Although the volume fraction Φ of our samples is low, $\underline{K}_\parallel$ is large due to the high particle aspect ratio and the large electrical conductivity mismatch between the SWNTs and the solvent (Eq. 4.24). Thus, the effect of electrostatic interactions on the particle equilibrium orientation angle at short time scales is a consequence of the large aspect ratio of the nanotubes in these dilute suspensions.

Besides the effect of electrostatic interaction between two neighboring particles, there are other possibilities which could contribute to the discrepancy between the experimental results and the predictions of classical theory. Hydrodynamic interactions between particles (in particular, particles prevented from rotating in the shear flow by the electric field) may affect the ensemble-averaged particle orientation. Particle interactions with the walls could also affect the equilibrium orientation of the particles, as the transmitted laser beam, whose diameter is of the same order as the gap width, could probe the orientations of particles close to the walls. In addition, it should be noted that the equilibrium particle orientations that are measured are the cumulative ensemble-averaged orientation angles along the path of the transmitted laser beam. While the laser pathlength of 5 cm is large compared to the gap width of 3.2 mm, the measurement necessarily includes particle orientations near the top and bottom of the concentric cylinder, where the flow may deviate substantially from simple shear flow, and the electric field is not uniform and radial. Although these possibilities may contribute to the difference between the experiments and the theory, the data (Fig. 4.15) and analysis indicate that there is a clear concentration effect, and that electrostatic interactions between particles can be significant even at low concentrations.

The esemble-averaged particle orientation angle changes with sample suspension concentration at various f are plotted in Fig. 4.17 and the difference between the experimental results and the ideal value (calculated from Mason's theory) is shown in Fig. 4.18.
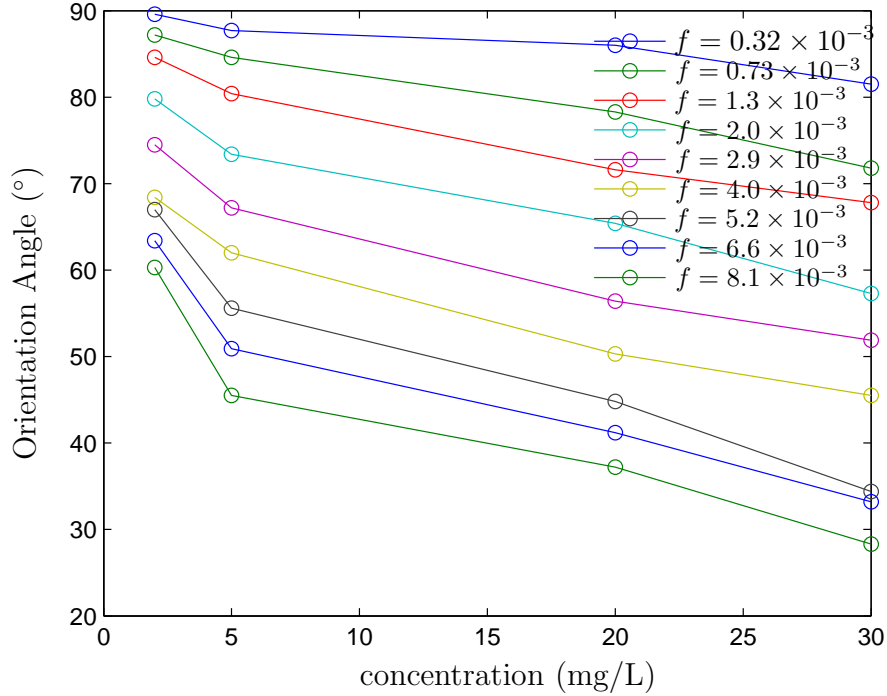
Figure 4.17: Ensemble-averaged particle orientation angle changes with sample suspension at various f, the dimensionless parameter.

4.6 Summary

In summary, we have performed simultaneous measurements of the shear viscosity and equilibrium particle-orientation angle of dilute SWNT/α-terpineol suspensions under-combined shear and electric fields. The ER behavior of these suspensions shows more than a doubling of apparent viscosity at low shear rates, with a very long time scale to reach steady state, as consistent with previous work on low-concentration suspensions [42, 89]. The measured equilibrium particle-orientation angles reach steady state at least an order-of-magnitude faster than the apparent-viscosity response. Particle-orientation angles for various shear rates and field strengths collapse well when plotted against Mason's predicted parameter $E^2/\dot{\gamma}$ or the equivalent dimensionless number f. This is the evidence that the orientational behavior of the SWNTs/bundles in these suspensions under both shear and electric fields can be characterized by the ratio of electrostatic and hydrodynamic torques. The difference in time scales between the
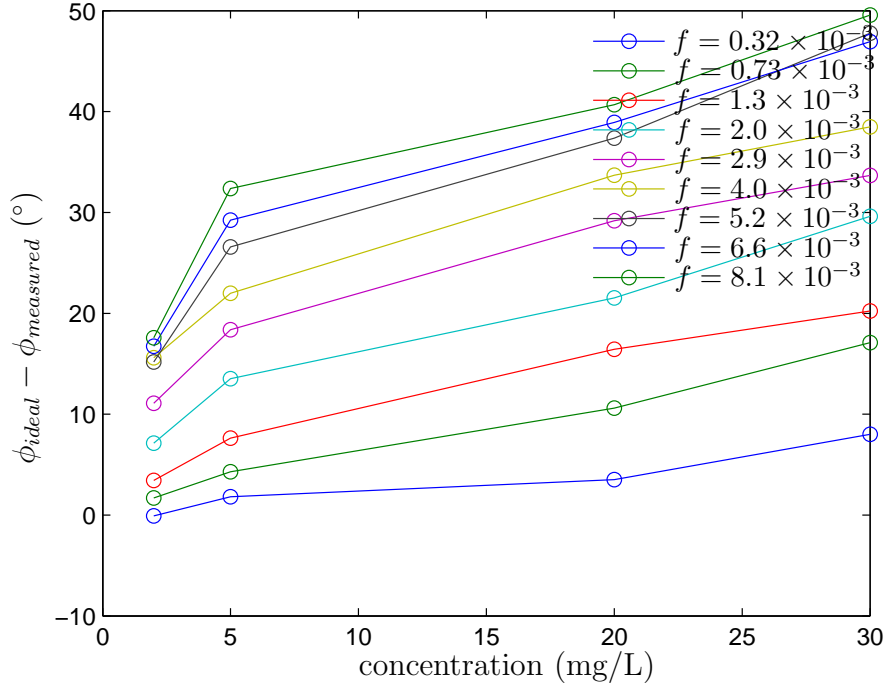
Figure 4.18: The difference between the measured and the ideal (calculated from Mason's theory) particle orientation angle changes with sample suspension at various f, the dimensionless parameter.

particle-orientation response and the macroscopic electrorheological response indicates that the particle-orientation angle does not have a direct impact on the ER properties of these dilute suspensions. (However, the particle orientation does affect the induced dipole moment and thus may indirectly influence the suspension rheology by affecting the particle-particle chaining process.) It is experimentally found that even for dilute suspensions, electrostatic particle-particle interactions significantly affect equilibrium orientation angle, with deviations from classical theory increasing with particle concentration. Estimates of the electrostatic interaction moment for paired particles in a simple configuration show that this interaction can be significant, and that it tends to orient the particles additionally in the electric-field direction. Thus, even for SWNT suspensions that are classically dilute in the sense of Eq. (4.12), electrostatic particle-particle interactions can cause deviations from Mason's theory for the equilibrium orientation angles of an ellipsoidal particle in shear flow subject to an external

electric field.

Chapter 5

Conclusions and perspectives for future work

5.1 Conclusion

Two closely related projects have been conducted on the macroscopic eletrorheology and equilibrium orientation angles of SWNTs in liquid suspension. In the first project, the apparent shear viscosity of dilute suspensions of single-wall carbon nanotubes was experimentally investigated and found to change significantly under external electric fields. In particular, the apparent viscosity of a dilute SWNT/α-terpineol suspension more than doubled at moderate shear rates under an external electric field of strength 160 V/mm. By systematically varying the shear rate and electric field, we found that the electrorheological response can be interpreted in terms of an electrostatic-polarization model, where the governing parameter was a modified Mason number giving the ratio of viscous to dipole-dipole forces. Analysis of the electrostatic forces suggested that the magnitude of the electrorheological response in the dilute SWNT suspension, which was much higher than conventional spherical-particle suspensions of comparable volume fractions, was due to the high aspect ratio of the nanotubes. This work was the first to our knowledge on the electrorheology of SWNT suspensions, and the first to observe significant electrorheological activity in a suspension of such low volume fraction.

In the second project, simultaneous measurements of the apparent shear viscosity and the ensemble-averaged equilibrium particle orientation angle of dilute SWNT/α-terpineol suspensions under both shear and electric fields was performed. The particle orientation time scales were found to be one to two orders of magnitude faster than the rather slow electrorheological response. This implies that the nanotube orientation angle does not have direct impact on the ER properties of these dilute suspensions, although it may still indirectly do so by affecting the induced dipole moment and the

electrostatic particle interaction. Further evidence for this comes from the results of repeated applications of the electric field (Fig. 4.3), which showed that the electrorheological response rate increased for subsequent applications of the electric field due to partially-remaining chain structure in the suspension. The measured ensemble-averaged particle orientation anglse for various shear rates and electric field strengts were seen to collapses well when plotted against Mason's predicted non-dimensional parameter f, or equivalently the variable $E^2/\dot{\gamma}$. This is the evidence that the orientational behavior of the SWNTs/bundles in these suspensions under both shear and electric fields can be characterized by the ratio of electrostatic and hydrodynamic torques. However, significant discrepancies are found between the experimental results and the theoretical predictions at the intermediate values of f (or $E^2/\dot{\gamma}$), with deviations from classical theory increasing with particle concentration. We attribute these discrepancies to the significant particle-particle interactions in the suspension even though the suspensions themselves are dilute by the conventional measures, *e.g.* Eq. (4.12). Lowest-order estimates of the electrostatic interaction moment for paired particles in a simple configuration show that this interaction can be significant, and that it tends to orient the particles additionally in the electric-field direction.

5.2   Suggested future work

Concentration effects on the ER response of SWNT suspensions have not been studied, apart from preliminary work by a former lab member, Peter Huang. Such studies may further strengthen our argument here that the polarization model can characterize the ER behavior of our suspensions by testing various inter-particle spacings and thus the electrostatic interactions. The dipole-dipole interaction between particles in a uniform electric field depends on the distance between neighboring particles, and thus the time scale of the ER response is expected to depend on the particle concentration. Moreover, we have not yet been able to quanitatively predict the precise dependence of the equilibrium orientation angle on the particle concentration. In particular, one would seek a description of particle orientation angle as a function of both $E^2/\dot{\gamma}$ and Φ that would

collapse the data for different particle volume fractions shown in Fig. 4.15. Preliminary attempts to find power law or exponential dependence on particle concentration are shown in the the log-log and semilog-log plots of Fig. 4.14 and 4.15. There does not appear to be a simple scaling that collapses all of the data for varying concentration, shear rate, and field strength. Surface fitting of the particle orientation angle data as a function of two variables were also attempted as shown in Fig. 5.5, but none of these attempts seem to successfully solve the problem.

Another possible future project as a continuation of the work on particle dynamics under both shear and electric flow is to design an optical system with much faster response time than the current experimental setup. The initial response of the nanotubes to the turn-on of the electric field is very rapid and well beyond the capability of our current system. If the rate of polarization modulation in the optical system were increased by orders of magnitude, it would be possible to capture more details on the dynamic response of the SWNT suspensions to an external electric field. More detailed microscopic characterization of the particle chaining process would also be desirable to enable better understanding of the fluid microstructure and its effect on the rheology of the suspension.
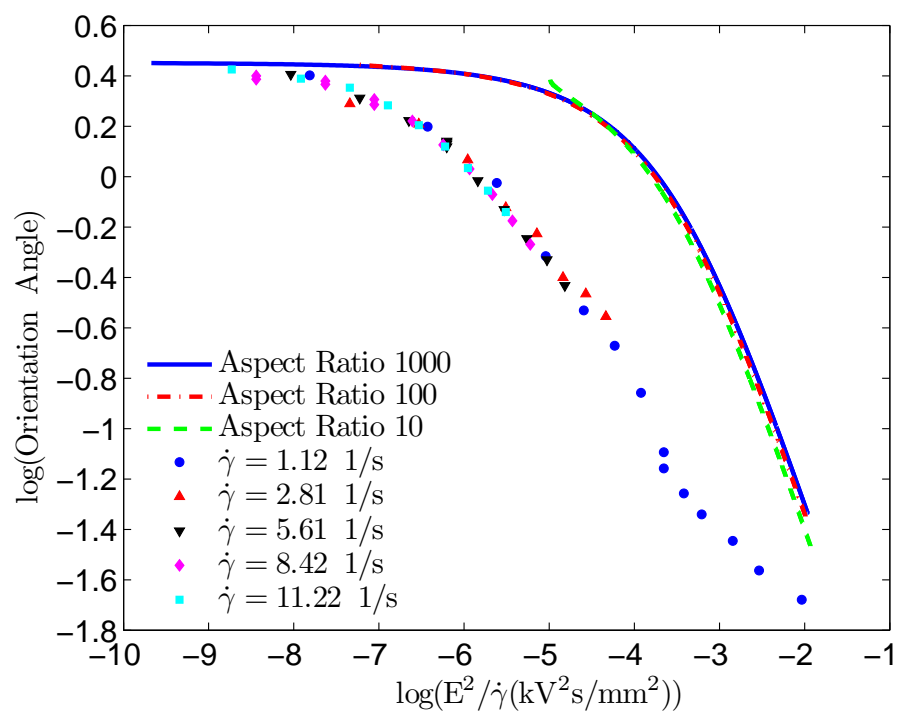
Figure 5.1: Log-log plot of particle orientation angle vs $E^2/\dot{\gamma}(kV^2/mm^2s^{-1})$.
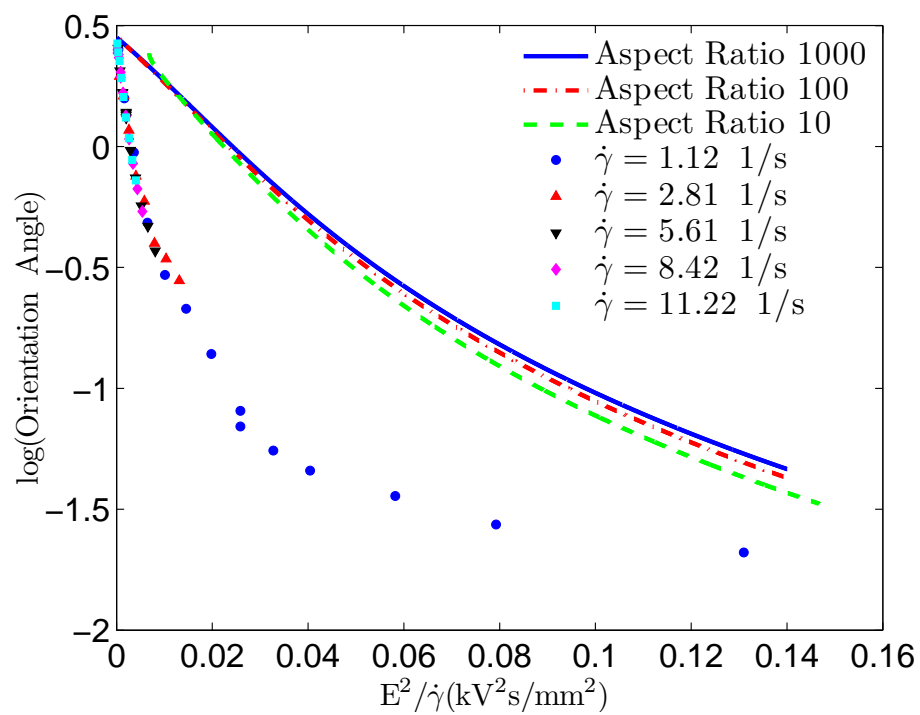
Figure 5.2: Semilog plot of particle orientation angle vs $\mathrm{E}^2/\dot{\gamma}(\mathrm{kV}^2/\mathrm{mm}^2\mathrm{s}^{-1})$.
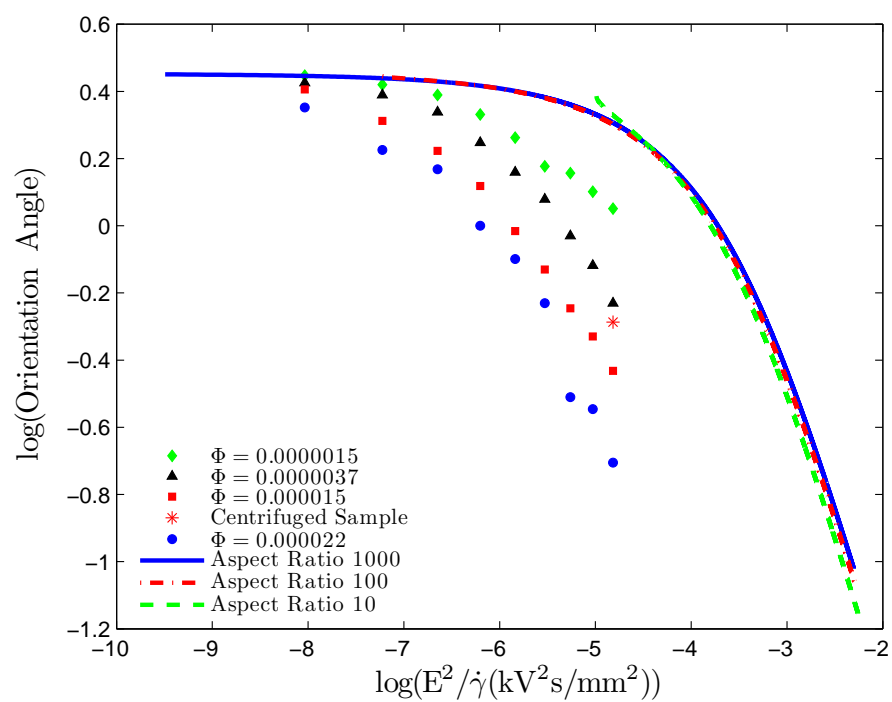
Figure 5.3: Log-log plot of particle orientation angle vs concentration.
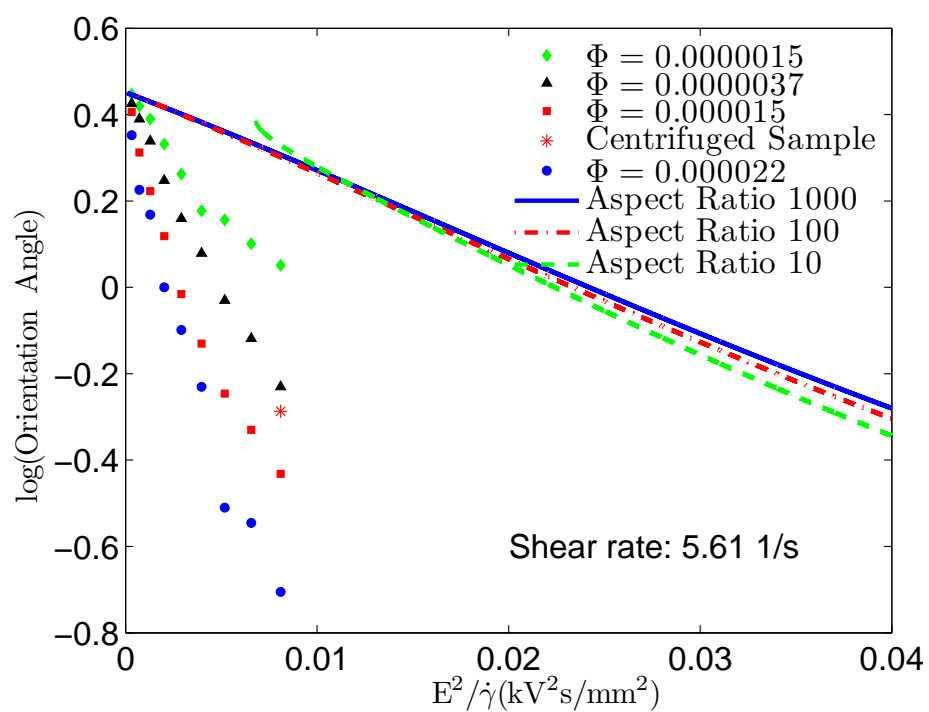
Figure 5.4: Semilog plot of particle orientation angle vs concentration.
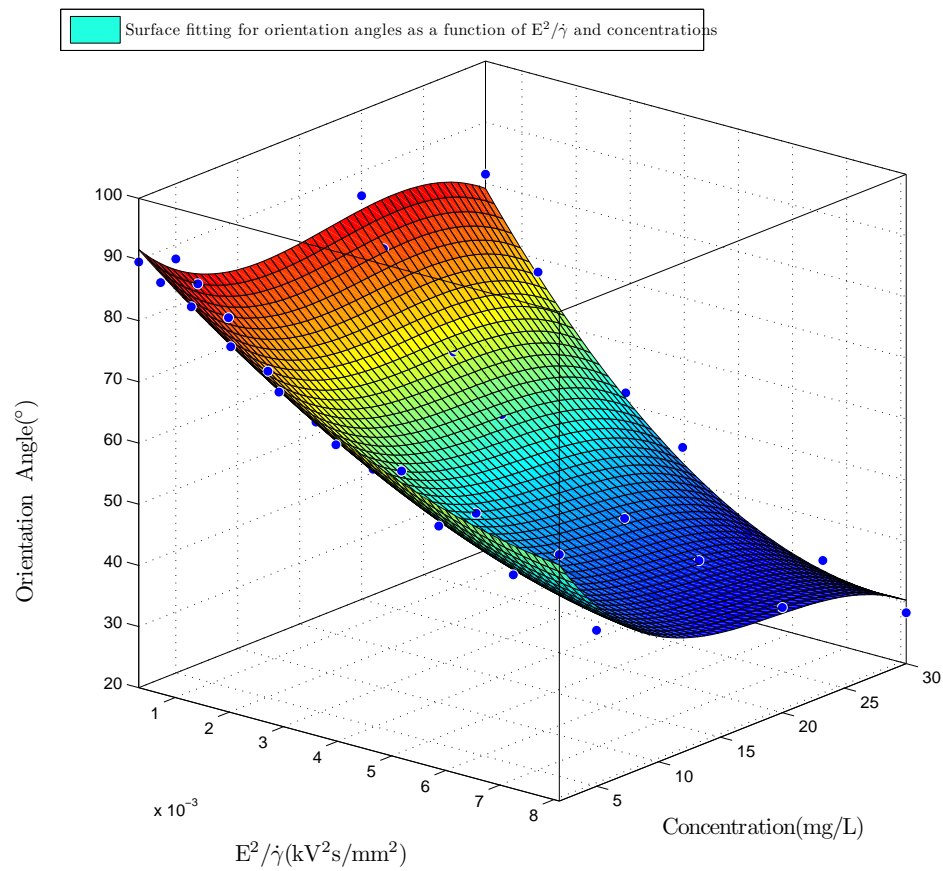
Figure 5.5: Surface fitting of particle orientation angle as a function of $E^2/\dot{\gamma}$ and concentration.

Appendix A

Derivation of the complex Clausius-Mossotti function for conducting particle suspended in a dielectric liquid medium at DC field

The three component of the complex Clausius-Mossotti function $\underline{K}$ have been shown in Eq. (2.23) as

$$\underline{K}_{x_1} = \frac{\underline{\epsilon}_p - \underline{\epsilon}_f}{3\left[\underline{\epsilon}_f + \left(\underline{\epsilon}_p - \underline{\epsilon}_f\right) L_{x_1}\right]}, \tag{A.1}$$

$$\underline{K}_{x_2} = \frac{\underline{\epsilon}_p - \underline{\epsilon}_f}{3\left[\underline{\epsilon}_f + \left(\underline{\epsilon}_p - \underline{\epsilon}_f\right) L_{x_2}\right]},$$

$$\underline{K}_{x_3} = \frac{\underline{\epsilon}_p - \underline{\epsilon}_f}{3\left[\underline{\epsilon}_f + \left(\underline{\epsilon}_p - \underline{\epsilon}_f\right) L_{x_3}\right]},$$

where

$$\underline{\epsilon}_f = \epsilon_f - \frac{\sigma_f}{\omega}j \tag{A.2}$$

$$\underline{\epsilon}_p = \epsilon_p - \frac{\sigma_p}{\omega}j \tag{A.3}$$

The definitions of $\underline{\epsilon}_f$ and $\underline{\epsilon}_p$ can be found in both Jones' book [58] and Parthasarathy and Klingenberg's paper [31]. ω is the frequency of the external AC field.

To demostrate, Let us take $\underline{K}_{x_1}$ as an example for the following derivation

$$
\underline{K}_{x_1} = \frac{\epsilon_p - \epsilon_f}{3\left[\underline{\epsilon}_f + (\underline{\epsilon}_p - \underline{\epsilon}_f)L_{x_1}\right]},
$$

$$
= \frac{(\epsilon_p - \epsilon_f) - \frac{1}{\omega}(\sigma_p - \sigma_f)j}{3\{(\epsilon_f - \frac{\sigma_f}{\omega}j) + [(\epsilon_p - \epsilon_f) - \frac{1}{\omega}(\sigma_p - \sigma_f)j]L_{x_1}\}}
$$

$$
= \frac{(\epsilon_p - \epsilon_f) - \frac{1}{\omega}(\sigma_p - \sigma_f)j}{3\{\epsilon_f + (\epsilon_p - \epsilon_f)L_{x_1} - \frac{1}{\omega}[\sigma_f + (\sigma_p - \sigma_f)L_{x_1}]j\}}
$$

$$
= \frac{[(\epsilon_p - \epsilon_f) - \frac{1}{\omega}(\sigma_p - \sigma_f)j]\{(\epsilon_f + (\epsilon_p - \epsilon_f)L_{x_1} + \frac{1}{\omega}[\sigma_f + (\sigma_p - \sigma_f)L_{x_1}]j\}}{3\{[\epsilon_f + (\epsilon_p - \epsilon_f)L_{x_1}]^2 + \frac{1}{\omega^2}[\sigma_f + (\sigma_p - \sigma_f)L_{x_1}]^2\}}
$$

then,

$$
\mathbf{Re}[\underline{K}_{x_1}] = \frac{(\epsilon_p - \epsilon_f)[\epsilon_f + (\epsilon_p - \epsilon_f)L_{x_1}] + \frac{1}{\omega^2}(\sigma_p - \sigma_f)[\sigma_f + (\sigma_p - \sigma_f)L_{x_1}]}{3\{[\epsilon_f + (\epsilon_p - \epsilon_f)L_{x_1}]^2 + \frac{1}{\omega^2}[\sigma_f + (\sigma_p - \sigma_f)L_{x_1}]^2\}}
$$

$$
= \frac{(\epsilon_p - \epsilon_f)[(1 - L_{x_1})\epsilon_f + \epsilon_p L_{x_1}] + \frac{1}{\omega^2}(\sigma_p - \sigma_f)[(1 - L_{x_1})\sigma_f + \sigma_p L_{x_1}]}{3\{[(1 - L_{x_1})\epsilon_f + \epsilon_p L_{x_1}]^2 + \frac{1}{\omega^2}[(1 - L_{x_1})\sigma_f + \sigma_p L_{x_1}]^2\}}
$$

$$
= \frac{(\epsilon_p - \epsilon_f)[(1 - L_{x_1})\epsilon_f + \epsilon_p L_{x_1}]\omega^2 + (\sigma_p - \sigma_f)[(1 - L_{x_1})\sigma_f + \sigma_p L_{x_1}]}{3\{(1 + \omega^2\tau_{mw}^2)[(1 - L_{x_1})\sigma_f + \sigma_p L_{x_1}]^2\}}
$$

$$(A.4)$$

where

$$
\tau_{mw} = \frac{(1 - L_{x_1})\epsilon_f + \epsilon_p L_{x_1}}{(1 - L_{x_1})\sigma_f + \sigma_p L_{x_1}}
$$

continue from Eq.(A.4) as

$$
= \frac{(\epsilon_p - \epsilon_f)\omega^2\tau_{mw}^2}{3(1 + \omega^2\tau_{mw}^2)[(1 - L_{x_1})\epsilon_f + \epsilon_p L_{x_1}]} + \frac{\sigma_p - \sigma_f}{3(1 + \omega^2\tau_{mw}^2)[(1 - L_{x_1})\sigma_f + \sigma_p L_{x_1}]}
$$

$$
= \frac{\epsilon_p - \epsilon_f}{3[(1 - L_{x_1})\epsilon_f + \epsilon_p L_{x_1}]} - \frac{\epsilon_p - \epsilon_f}{3(1 + \omega^2\tau_{mw}^2)[(1 - L_{x_1})\epsilon_f + \epsilon_p L_{x_1}]} + \frac{\sigma_p - \sigma_f}{3(1 + \omega^2\tau_{mw}^2)[(1 - L_{x_1})\sigma_f + \sigma_p L_{x_1}]}
$$

$$
= \frac{\epsilon_p - \epsilon_f}{3[(1 - L_{x_1})\epsilon_f + \epsilon_p L_{x_1}]} + \frac{(\sigma_p - \sigma_f)[(1 - L_{x_1})\epsilon_f + \epsilon_p L_{x_1}] - (\epsilon_p - \epsilon_f)[(1 - L_{x_1})\sigma_f + \sigma_p L_{x_1}]}{3(1 + \omega^2\tau_{mw}^2)[(1 - L_{x_1})\epsilon_f + \epsilon_p L_{x_1}][(1 - L_{x_1})\sigma_f + \sigma_p L_{x_1}]}
$$

$$
= \frac{\epsilon_p - \epsilon_f}{3[(1 - L_{x_1})\epsilon_f + \epsilon_p L_{x_1}]} + \frac{\sigma_p\epsilon_f - \sigma_f\epsilon_p}{3\tau_{mw}(1 + \omega^2\tau_{mw}^2)[(1 - L_{x_1})\sigma_f + \sigma_p L_{x_1}]^2}
$$

$$(A.5)$$

For spherical particle, $L_{x_1} = \frac{1}{3}$, and Eq.(A.5) simplifies to

$$\mathbf{Re}[\underline{K}_{x_1}] = \frac{\epsilon_p - \epsilon_f}{2\epsilon_f + \epsilon_p} + \frac{3(\sigma_p \epsilon_f \sigma_f \epsilon_p)}{\tau_{mw}(1 + \omega^2 \tau_{mw}^2)(2\sigma_f + \sigma_p)^2}$$

which agrees well with the formula on Page 40 in Jones' book [58].

For general L_{x_1}, we have

$$\mathbf{Re}[\underline{K}_{x_1}] = \begin{cases} \frac{\epsilon_p - \epsilon_f}{3[(1-L_{x_1})\epsilon_f + \epsilon_p L_{x_1}]}, & \text{for } \omega\tau_{mw} >> 1 \\ \frac{\sigma_p - \sigma_f}{3[(1-L_{x_1})\sigma_f + \sigma_p L_{x_1}]}, & \text{for } \omega\tau_{mw} << 1 \end{cases}$$

So when $\omega\tau_{mw} << 1$, we have

$$\begin{aligned} \mathbf{Re}[\underline{K}_{x_1}] &= \frac{\sigma_p - \sigma_f}{3[(1 - L_{x_1})\sigma_f + \sigma_p L_{x_1}]} \\ &= \frac{1 - \sigma_f/\sigma_p}{3[(1 - L_{x_1})\sigma_f/\sigma_p + L_{x_1}]} \end{aligned}$$

When $\sigma_f/\sigma_p << 1$, then $\mathbf{Re}[\underline{K}_{x_1}] = \frac{1}{3L_{x_1}}$ is a constant.

Appendix B

Detailed design and operation procedure of simultaneous rheology and particle orientation measurements

The experimental setup and sample preparation of simultaneous rheology and particle orientation measurements of SWNTs/α-terpineol suspensions were described in Ch. **4**. Detailed description of each operation steps including the alignment of the laser beam, the determination of initial phase β_0 and the time sequence of applications of shear flow and electric field on the samples will be given here. The functions of each component in the optical train and the related calculations will also be included.

B.1   Design and components of the optical system

The optical system we used to detect the orientation of SWNT/bundle in suspensions consisted five parts. The first component of the whole optical system, a linearly polarized helium-neon laser, was secured in an alumina frame. The laser was tilted so that the laser head was up and a 5° angle was formed between the laser's longitudinal axis and the horizontal direction (surface of our optical table). This 5° tilting angle was used later to compensate the angle difference between the actual bended angle by the polarization-conserving light bending prism (bend light 95° using the material having the closest refractive index to the theoretically calculated number) and perfect 90° bending. The second component right after the laser was a Glan-Taylor calcite polarizer which was aligned in the horizontal direction using square ruler. This G-T polarizer had two basic functions in our system: (1) to make the polarization of the laser beam only in horizontal direction; (2) to make the intensity of the light adjustable. Since the original laser beam was linearly polarized, by rotating the laser we could change the original polarization direction of the beam as to adjust the light intensity after the G-T

polarizer. The next part was the pulley-motor system which rotated the polarization direction of the light. The motor could run up to 5200 RPM and it had an encoder assembled together with it. The encoder had two channels with each channel having 500 counts per resolution (CPR). In order to use the signals from the encoder as a reference signal for the lock-in amplifier, an electrical device called EDivide was used to bring the signal frequency down to 4 counts per resolution. This frequency was also the frequency at which we were interested when we analyze the output signals from the photodiode as can be seen in Eqn.4.22. The component after the pulley-motor system was the polarization-conserving light bending prism. Ideally we need an optical element which can deflect the incident laser beam 90° without changing the polarization state of the light (both magnitude and phase). A specially designed prism using total internal reflection was a good solution for us. The detailed calculation of the design of the prism is as following:

The phase shift Δ resulting from an internal reflection was given by

$$\tan \frac{\Delta}{2} = \cos \phi_i \left(\sin^2 \phi_i - \left(\frac{n_{air}}{n_{glass}} \right)^2 \right)^{1/2} / \sin^2 \phi_i \tag{B.1}$$

where ϕ_i was the incident angle on the surface, n_{air} and n_{glass} were the index of refraction of air and glass respectively. We could see that Δ was a function of ϕ_i and the ratio of the refractive index of two mediums.

The idea was we optimally select the incident angle ϕ_i and the n_{glass} at $632nm$ wavelength so that after a few times of internal reflections we could achieve $80 \sim 100°$ bending of the original laser beam and a $180°$ or $360°$ change of Δ.

The design of this prism is illustrated in Fig. B.1., A $60°$ phase shift could be achieved by a particular incident angle of $47.7°$ if we used a glass (H-ZF6) which had 1.74968 index of refraction at $632nm$. Three times internal reflection would give us $95.4°$ deflection and $180°$ phase shift.

The last component of the optical system was the photodiode which sensed the intensity of the light and sent the electrical signal to the lock-in amplifier.
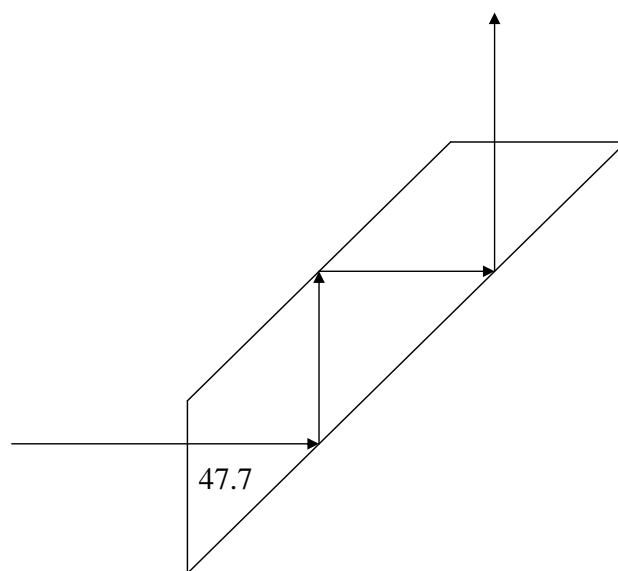
47.7

Figure B.1: An example of prism design.

B.2 Operation of the simultaneous rheology and particle orientation measurements

Before the particle orientation measurements are conducted, the alignment of all the optical components in the optical train and the concentric cylinder cell of the viscometer must be performed. The procedure of the alignment are described as below: (1) Adjust the laser so that 5° angle is formed between its longitudinal axis and the horizontal direction. (2) Align the Glan-Taylor polarizer so that the transmitting axis of the polarizer is parallel to the horizontal direction. (3) Align the rotating aluminum tube with the half-wave plate attached so that the light spot is right in the center of the half-wave plate. (4) Align the polarization-conserving prism to make sure that the transmitted light from the second face of the prism is pointing up vertically. In order to achieve this, a down-facing horizontally positioned mirror is needed. Perfect vertical light will only be achieved when the incident and the reflected beams overlap each other. (5) Align the outer cylinder of the concentric cylinder cell so that the 90° tick on the top edge of the cylinder is parallel to the transmitting axis of G-T polarizer used in (2). To do this, another G-T polarizer will be needed. (6) Align the photodiode so that the laser spot is right in the center of the sensor.

After the alignment, one more step is required before we can fill sample suspensions into the gap between the concentric cylinders: the acquirement of the initial phase of the half wave-plate. As we can see in Eqn.4.22, β_0 must be known in order to get the essemble-averaged orientation angle of the particles in suspensions. The way to obtain β_0 is to replace the sample with a polarizer at known orientation angle. In our case we positioned our polarizer at 90° referring to the transmitting axis of the first polarizer in step (2), because this way all we need to do is take off the half-wave plate and adjust the second polarizer so that the output signal reaches minimum. Then put the half-wave plate back on the aluminum tube, start the measurements (only run for a couple of minutes) and analyze the signal the same fashion as described in Ch. **4**, mathematical analysis part, the initial phase of the half-wave plate can be easily obtained. One caveat here is that DO NOT turn off the power supply for the Edivide. As long as the 5-volts

power is supplied to the Edivide, the initial phase of the half-wave plate will not change unless the optical setup is changed.

Now the sample suspensions can be filled into the gap of the concentric cylinders. The viscometer is controlled by the software called Rheocalc provided by the manufacturer. The lock-in amplifier installed in a PC and the motor which rotates the half-wave plate have to be turned on first, in another words, the optical measurement should start before anything else. 30 seconds later, the viscometer starts rotating which generates a shear flow. The external electric field is applied 160 seconds after the beginning of the shear flow and is on for about 10 minutes. Once the electric field is turned off, there will be another 100 seconds of data in order to test if the particles return to the original motion state.

The electrical signal output from the photodiode is received and further analyzed by the Lock-In amplifier using National Instrument DSA-4472 card. For further information of the modification of the software lock-in amplifier, please see the user manual of NI lock-in start up kit. The programs used in our experiments are saved in the following two files: (1) MultiChannelLockInDAQmxBinary03.vi and (2) MyBinaryRead.vi.

References

[1] S. Iijima and T. Ichihashi. Single-shell carbon nanotubes of 1-nm diameter. *Nature*, 363:603–615, 1993.

[2] H. R. Baughman, A. A. Zakhidov, and W. A. Heer. Carbon nanotubes–the route toward applications. *Science*, 297:787–792, 2002.

[3] D. Qian, E. C. Dickey, R. Andrews, and T. Rantell. Load transfer and deformation mechanisms in carbon nanotube-polystyrene composites. *Appl. Phys. Lett.*, 76:2868, 2000.

[4] C. Zandonella. Is it all just a pipe dream. *Nature*, 410:734–735, 2001.

[5] Y. Chen, D. T. Shaw, X. D. Bai, E. G. Wang, C. Lund, W. M. Lu, and D. D. L. Chung. Hydrogen storage in aligned carbon nanotubes. *Appl. Phys. Lett.*, 78:2128, 2001.

[6] W. A. Heer, A. Chtelain, and D. Ugarte. A carbon nanotube field-emission electron source. *science*, 270:1179–1180, 1995.

[7] Y. Saito and S. Uemura. Field emission from carbon nanotubes and its application to electron sources. *Carbon*, 38:169–182, 2000.

[8] Z. Liu, W. Cai, L. He, N. Nakayama, K. Chen, X. Sun, X. Chen, and H. Dai. In vivo biodistribution and highly efficient tumour targeting of carbon nanotubes in mice. *Nature Nanotechnology*, 2:47–52, 2007.

[9] S. G. Louie. Electronic properties, junctions, and defects of carbon nanotubes. *Top.Appl.Phys*, 80:113–145, 2001.

[10] J. N. Coleman, W. J. Blau, A. B. Dalton, E. Muoz, S. Collins, B. G. Kim, J. Razal, M. Selvidge, G. Vieiro, and R. H. Baughman. Improving the mechanical properties of single-walled carbon nanotube sheets by intercalation of polymeric adhesives. *Appl. Phys. Lett.*, 82:1682–1684, 2003.

[11] J. N. Coleman, M. Cadek, K. P. Ryan, A. Fonseca, J. B. Nagy, W. J. Blau, and M. S. Ferreira. Reinforcement of polymers with carbon nanotubes. the role of an ordered polymer interfacial region. experiment and modeling. *Polymer*, 47:8556–8561, 2006.

[12] J. Wei, Y. Jia, Q. Shu, Z. Gu, K. Wang, D. Zhuang, G. Zhang, Z. Wang, J. Luo, A. Cao, and D. Wu. Double-walled carbon nanotube solar cells. *Nano lett.*, 8:2317–2321, 2007.

[13] E. Kymakis and G. A. J. Amaratunga. Single-wall carbon nanotube/conjugated polymer photovoltaic devices. *Appl. Phys. Lett.*, 80:112–114, 2002.

[14] S. T. Kim, J. Y. Lim, B. J. Park, and H. J. Choi. Dispersion polymerized carbon nanotube poly methyl methacrylate composite particles and their electrorheological characteristics. *Macromol. Chem. Phys.*, 208:514–519, 2007.

[15] R. S. Voronov, D. V. Papavassiliou, and L. L. Lee. Boundary slip and wetting properties of interfaces: Correlation of the contact angle with the slip length. *J. Chem. Phys.*, 124:204701, 2006.

[16] J. Chen, S. Chen, X. Zhao, L. V. Kuznetsova, S. S. Wong, and I. Ojima. Functionalized single-walled carbon nanotubes as rationally designed vehicles for tumor-targeted drug delivery. *J. Am. Chem. Soc.*, 130:16778–16785, 2008.

[17] M. F. Islam, E. Rojas, D. M. Bergey, A. T. Johnson, and A. G. Yodh. High weight fraction surfactant solubilization of single-wall carbon nanotubes in water. *Nano Lett.*, 3:269–273, 2003.

[18] J. L. Bahr, E. T. Mickelson, M. J. Bronikowski, R. E. Smalley, and R. E. Tour. Dissolution of small diameter single-wall carbon nanotubes in organic solvents. *Chem. Comm.*, pages 193–194, 2001.

[19] M. Ferrari. Nanogeometry beyond drug delivery. *nature nanotechnology*, 3:131–132, 2008.

[20] B. Vigolo, A. Penicaud, C. Coulon, C. Sauder, R. Pailler, C. Journet, P. Bernier, and P. Poulin. Macroscopic fibers and ribbons of oriented carbon nanotubes. *Science*, 290:1331–1334, 2000.

[21] Z. Wu, Z. Chen, X Du, M. J. Logan, J. Sippel, M. Nikolou, K. Kamaras, R. J. Reynolds, B. D. Tanner, F. A. Hebard, and G. A. Rinzler. Transparent, conductive carbon nanotube films. *Science*, 305:1273–1276, 2004.

[22] K. Bubke, H. Gnewuch, M. Hempstead, J. Hammer, and M. L. H. Green. Optical anisotropy of dispersed carbon nanotubes induced by an electric field. *Appl. Phys. Lett.*, 71:1906, 1997.

[23] M. S. Arnold, A. A. Green, J. F. Hulvat, S. I. Stupp, and M. C. Hersam. Sorting carbon nanotubes by electronic structure using density differentiation. *nature nanotechnology*, 1:60–65, 2006.

[24] M. Zheng, A. Jagota, M. S. Strano, A. P. Santos, P. Barone, S. G. Chou, B. A. Diner, M. S. Dresselhaus, R. S. Mclean, G. B. Onoa, G. G. Samsonidze, E. D. Semke, M. Usrey, and D. J. Walls. Structure-based carbon nanotube sorting by sequence-dependent dna assembly. *Science*, 302:1545–1548, 2003.

[25] W. M. Winslow. Induced fibration of suspensions. *J. Appl. Phys.*, 20:1137–1140, 1949.

[26] A. P. Gast and C. F. Zukoski. Electrorheological fluids as colloidal suspensions. *Adv. Colloid interface Sci.*, 30:153–202, 1989.

[27] H. Block, A. Qin J. P. Kelly, and T. Watson. Materials and mechanisms in electrorheology. *Langmuir*, 6:6–14, 1990.

[28] D. J. Klingenberg and C. F. Zukoski. Studies on the steady-shear behavior of electrorheological suspensions. *Langmuir*, 6:15–24, 1990.

[29] L. C. Davis. Polarization forces and conductivity effects in electrorheological fluids. *J. Appl. Phys.*, 72:1334–1340, 1992.

[30] H. Block and J. P. Kelly. Electrorheology. *J. Phys. D: Appl. Phys.*, 21:1661, 1988.

[31] M. Parthasarathy and D. J. Klingenberg. Electrorheology: Mechanisms and models. *Mater. Sci. Eng. R*, 17:57, 1996.

[32] T. Hao. Electrorheological suspensions. *Adv. Colloid interface Sci.*, 97:1, 2002.

[33] W. Wen, X Huang, S. Yang, K. Lu, and P. Sheng. The giant electrorheological effect in suspensions of nanoparticlesnature. *Nat. Mater.*, 2:727–730, 2003.

[34] X. Huang, W. Wen, S. Yang, and P. Sheng. Mehcanisms of the giant electrorheological effect. *Solid state communications*, 139:581–588, 2006.

[35] K. Lozano, C. Hernandez, T. W. Petty, M. B. Sigman, and B. Korgel. Electrorheological analysis of nano laden suspensions. *J. Colloid Interface Sci.*, 297:618–624, 2006.

[36] J. Yin, X. Zhao, L. Xiang, X. Xiang, and Z. Zhang. Enhanced electrorheology of suspensions containing sea-urchin-like hierarchical cr-doped titania particles. *Soft Matter*, 5:4687–4697, 2009.

[37] A. Hong, M. Choi, C. Kim, and J. Jang. Geometrical study of electrorheological activity with shape-controlled titania-coated silica nanomaterials. *J. Colloid Interface Sci.*, 347:177–182, 2010.

[38] H. J. Choi, S. J. Park, Kim S. T, and M. S. Jhon. Electrorheological application of polyaniline/multi-walled carbon nanotube composites. *Diamond Relat. Mater.*, 14:766, 2005.

[39] J. Yin and X. Zhao. Titanate nano-whisker electrorheological fluid with high suspended stability and ER activity. *Nanotechnology*, 17:192, 2006.

[40] J. Yin and X. Zhao. Electrorheological properties of titanate nanotube suspensions. *Colloid Surf. A*, 329:153, 2008.

[41] C. R. Kanu and T. M. Shaw. Enhanced electrorheological fluids using anisotropic particles. *J. Rheol.*, 42:657–670, 1998.

[42] C. Lin and J. W. Shan. Electrically tunable viscosity of dilute suspensions of carbon nanotubes. *Phys. Fluids*, 19:121702, 2007.

[43] J. Happel and H. Brenner. *Low Reynolds number Hydrodynamics*. Martinus Nijhoff Publishers, Dordrecht, 1986.

[44] L. G. Leal. Particle motions in a viscous fluid. *Annual Reviews of Fluid Mechanics*, 12:435, 1980.

[45] G. B. Jeffery. The motion of ellipsoidal particles immersed in a viscous fluid. *Proc. Roy. Soc. London*, 102:161–179, 1922.

[46] G. I. Taylor. The motion of ellipsoidal particles in a viscous fluid. *Proc. R. Soc. London, Ser. A*, 103:58, 1923.

[47] R. Duggal and M. Pasquali. Dynamics of individual single walled carbon nanotubes in water by real time visualization. *Phys. Rev. Lett.*, 23:246104, 2006.

[48] E. K. Hobbie, H. Wang, H. Kim, and S. Lin-Gibson. Orientation of carbon nanotubes in a sheared polymer melt. *Phys. Fluids*, 15:1196, 2003.

[49] E. K. Hobbie and D. J. Fry. Rheology of concentrated carbon nanotube suspensions. *J. Chem. Phys.*, 126:124907, 2007.

[50] M. K. Tiwari, A. V. Bazilevsky, A. L. Yarin, and C. M. Megaridis. Elongational and shear rheology of carbon nanotube suspensions. *Rheol. Acta*, 48:597, 2009.

[51] E. K. Hobbie, H. Wang, H. Kim, c. C. Han, E. A. Grulke, and J. Obrzut. Optical measurements of structure and orientation in sheared carbon-nanotube suspensions. *Rev. Sci. Instrum.*, 74:1244–1250, 2003.

[52] E. K. Hobbie. Optical anisotropy of nanotube suspensions. *J. Chem. Phys.*, 121:1029–1037, 2004.

[53] X. Q. Chen, T. Saito, H. Yamada, and K. Matsushige. Aligning single-wall carbon nanotubes with an alternating-current electric field. *Appl. Phys. Lett.*, 78:3714, 2001.

[54] M. Brown, J. W. Shan, C. Lin, and F. Zimmermann. Electrical polarizability of single-wall nanotubes in liquid suspension. *Appl. Phys. Lett.*, 90:203108, 2007.

[55] F. M. Zimmermann and J. W. Shan. Rotational friction of single-wall carbon nanotubes in liquid suspension. *Appl. Phys Lett.*, 94:053107, 2009.

[56] V. Pryamitsyn and V. Ganesan. Structure of aggregating rod suspensions under combined shear and electric fields. *Macromolecules*, 42:7184, 2009.

[57] A. J. Stratton. *Electromagnetic theory*. McGraw-Hill book company, Inc, New York and London, 1941.

[58] T. B. Jones. *Electromechanics of Particles*. Cambridge Univ. Press, Cambridge, 1995.

[59] R. Krupke, F. Hennrich, V. H. Lohneysen, and M. M. Kappes. Separation of metallic from semiconducting single walled carbon nanotubes. *Science*, 301:344–347, 2003.

[60] J. D. Jackson. *Classical Electrodynamics*. John Wiley & Sons. Inc, New York, 1998.

[61] R. G. Larson. *The Structure and Rheology of Complex Fluids*. Oxford University Press, Oxford, 1999.

[62] A. Okagawa, R. G. Cox, and S. G. Mason. The kinetics of flowing dispersion vi. transient orientation and rheological phenomena of rods and discs in shear flow. *J. Colloid Interface Sci.*, 45:303–329, 1973.

[63] A. Okagawa, R. G. Cox, and S. G. Mason. Particle behavior in shear and electric fields vi. the microrheology of rigid spheroids. *J. Colloid Interface Sci.*, 47:536–567, 1974.

[64] H. Goldstein. *Classical Mechanics*. Addison Wesley, London, 1980.

[65] A. F. Stevenson. Solution of electromagnetic scattering problems as power series in the ratio (dimension of scatterer)/wavelength. *J. Appl. Phys*, 24:1134–1142, 1953.

[66] A. F. Stevenson. Electromagnetic scattering by an ellipsoid in the third approximation. *J. Appl. Phys*, 24:1143–1150, 1953.

[67] S. J. Johnson. *Simultaneous dichroism and birefringence measurements of sheared colloidal suspensions in polymeric liquids*. PhD thesis, Stanford University, 1987.

[68] G. G. Fuller and K. J. Mikkelsen. Optical rheometry using a rotary polarization modulator. *J. Rheol.*, 33:761, 1989.

[69] B. Kim, Y. H. Lee, J. H. Ryu, and K. D. Suh. Enhanced colloidal properties of single-wall carbon nanotubes in α-terpineol and Texanol. *Colloids and Surf. A*, 273:161–164, 2006.

[70] M. Assael, C.-F. Chen, I. Metaxa, and W. Wakeham. Thermal conductivity of suspensions of carbon nanotubes in water. *Int. J. Thermophys.*, 25:971–985, 2004.

[71] M. J. O'Connell, S. M. Bachilo, C. B. Huffman, V. C. Moore, M. S. Strano, E. H. Haroz, K. L. Rialon, P. J. Boul, W. H. Noon, C. Kittrell, J. Ma, R. H. Hauge, R. B. Weisman, and R. E. Smalley. Band gap fluoresence from individual single walled carbon nanotubes. *Science*, 298:593–596, 2002.

[72] M. J. Espin, A. V. Delgado, and F. G. Caballero. Structural explanation of the rheology of a colloidal suspension under high dc electric fields. *Phys. Rev. E*, 73:041503, 2006.

[73] L. A. Girifalco, M. Hodak, and R. S. Lee. Carbon nanotubes, buckyballs, ropes, and a universal graphitic potential. *Phys. Rev. B*, 62:13104, 2000.

[74] J. N. Foulc, P. Atten, and N. Felici. Macroscopic model of interaction between particles in an electrorheological fluid. *J. Electrostat.*, 33:103, 1994.

[75] Y. Otsubo. Electrorheology of whisker suspensions. *Colloids Surf. A: Phys. Eng. Aspects*, 153:459, 1999.

[76] K. Tsuda, Y. Takeda, H. Ogura, and Y. Otsubo. Electrorheological behavior of whisker suspensions under oscillatory shear. *Colloids Surf. A: Phys. Eng. Aspects*, 299:262, 2007.

[77] E. M. Lifshitz, L. D. Landau, and L. P. Pitaevskii. *Electrodynamics of Continuous Media*. Butterworth-Heinemann, Oxford, 1984.

[78] M. Doi and S. F. Edwards. *The Theory of Polymer Dynamics*. Oxford University Press, Oxford, 1986.

[79] J. A. Fagan, B. J. Landi, I. Mandelbaum, J. R. Simpson, V. Bajpai, B. J. Bauer, K. Migler, A. R. Hight Walker, R. Raffaelle, and E. K. Hobbie. Comparative measures of single wall carbon nanotube dispersion. *J. Phys. Chem. B*, 110:23801, 2006.

[80] B. I. Yakobson and L. S. Couchman. Persistence length and nanomechanics of random bundles of nanotubes. *J. Nanopart. Res.*, 8:105, 2006.

[81] Y. Mori, N. Ookubo, R. Hayakawa, and Y. Wada. Low-frequency and high-frequency relaxations in dynamic electric birefringence of poly(γ-benzyl-l-glutamate) in m-cresol. *J. Polym. Sci.*, 20:2111, 1982.

[82] M. F. Islam, D. E. Milkie, C. L. Kane, A. G. Yodh, and J. M. Kikkawa. Direct measurement of the polarized optical absorption cross section of single-wall carbon nanotubes. *Phys. Rev. Lett.*, 92:037404, 2004.

[83] G. G. Fuller. Optical rheometry. *Annual Reviews of Fluid Mechanics*, 22:387, 1990.

[84] W. R. Anderson. Polarization conserving light bending prisms and optimized Fresnel rhombs. *Appl. Opt.*, 13:1110, 1974.

[85] G. J. Kirkwood and L. P. Auer. The visco-elastic properties of solutions of rod-like macromolecules. *J. Chem. Phys.*, 19:281, 1951.

[86] P. H. Jensen, A. J. Schellman, and T. Troxell. Modulation techniques in polarization spectroscopy. *Appl. Spectrosc.*, 32:192–200, 1978.

[87] A. Karnis, H. L. Goldsmith, and S. G. Mason. The flow of suspensions through tubes: V. inertial effects. *Can. J. Chem. Eng.*, 44:181, 1966.

[88] A. L. Yarin, O. Gottlieb, and I. V. Roisman. Chaotic rotation of triaxial ellipsoids in simple shear flow. *J. Fluid Mech.*, 340:83, 1997.

[89] E. Svasand, K. L. Kristiansen, O. G. Martinsen, G. Helgesen, S. Grimnes, and A. T. Skjeltorp. Behavior of carbon cone particle dispersions in electric and magnetic fields. *Colloid Surf. A*, 339:211, 2009.

Vita

Chen Lin

2010   Ph.D. in Mechanical and Aerospace Engineering, Rutgers University

2000-2003 M.S. in Engineering Mechanics, Fudan University

1996-2000 B.S. in Theoretical and Applied Mechanics, Fudan Universtiy

2004-2009 Teaching assistant, Department of Mechanical and Aerospace Engineering, Rutgers University